Characterizing natural compounds for anticancer activity and validating RNA binding proteins as therapeutic cancer targets

Dissertation

zur Erlangung des Grades

des Doktors der Naturwissenschaften

der Naturwissenschaftlich-Technischen Fakultät

der Universität des Saarlandes

von

Shilpee Chanda

Saarbrücken

2023

Tag des Kolloquiums:	8. Februar 2024
Dekan:	Prof. Dr. Ludger Santen
Berichterstatter:	Prof. Dr. Alexandra K. Kiemer Prof. Dr. Andriy Luzhetskyy
Akad. Mitglied:	Dr. Konstantin Lepikhov
Vorsitz:	Prof. Dr. Marc Schneider

Contents

Abstract

Cancer stands as one of the foremost causes of death globally, underscoring the need for identifying new druggable targets. This study focuses on two strategies:

Part I: The first part characterizes the natural compound violacein as a potential anticancer agent. Violacein was assessed for its cytotoxic and anti-proliferative effects in cell lines from different cancer entities. Furthermore, its potential to induce immunogenic cell death was studied.

Part II: RNA binding proteins (RBPs) play pivotal roles in cancer initiation, progression, and metastasis, thus emerging as potential therapeutic targets in cancer treatment. In this study, two RBPs, ELAVL1/HuR and IGF2BP2/IMP2, were characterized through CRISPR/Cas9-mediated gene editing.

Successful monoallelic knockout of HuR was achieved in breast and liver cancer cell lines. The impact of monoallelic HuR knockout in MDAMB-231 breast cancer cells, as well as the effects of potential HuR inhibitors on cell proliferation across several cancer cell lines were evaluated.

IMP2 knockouts were generated in colon, lung, and hepatocellular cancer cell lines. The target specificity of IMP2 in knockout cells was assessed through rescue experiments by overexpression, and the effect on the expression of potential IMP2 targets was investigated. The effect of IMP2 knockout was evaluated *in vitro* regarding tumor cell proliferation, colony and spheroid formation, and migration, and small-molecule inhibitors of IMP2 were employed.

Zusamenfassung

Krebs gilt weltweit als eine der häufigsten Todesursachen, weshalb es erforderlich ist, neue therapeutische Targets zu identifizieren. Diese Studie konzentriert sich auf zwei Strategien:

Teil I: Der erste Teil charakterisiert den Naturstoff Violacein als mögliches Antikrebsmittel. Violacein wurde in Zelllinien verschiedener Entitäten hinsichtlich seiner zytotoxischen und antiproliferativen Wirkungen untersucht. Darüber hinaus wurde sein Potenzial zur Auslösung des immunogenen Zelltods untersucht.

Teil II: RNA-bindene Proteine (RBPs) spielen eine entscheidende Rolle von Krebs. In dieser Studie wurden zwei RBPs, ELAVL1/HuR und IGF2BP2/IMP2, durch CRISPR/Cas9-vermittelte Genbearbeitung charakterisiert.

In Brust- und Leberkrebszelllinien wurde ein erfolgreicher monoalleler Knockout von HuR erreicht. Der Einfluss des monoallelen HuR-Knockouts in MDAMB-231-Brustkrebszellen sowie die Auswirkungen potenzieller HuR-Inhibitoren auf die Zellproliferation über mehrere Krebszelllinien hinweg wurden untersucht.

IMP2-Knockouts wurden in Zelllinien von Dickdarm-, Lungen- und hepatozellulärem Krebs erzeugt. Die Target-Spezifität von IMP2 einer Knockout-Zelllinie wurde durch IMP2 Überexpression und Untersuchung der Expression potenzieller IMP2-Ziele bestätigt. Die Wirkung des IMP2-Knockouts wurde *in vitro* der Tumorzellproliferation, der Kolonie- und Sphäroidbildung bewertet und es wurden Migration und niedermolekulare Inhibitoren von IMP2 eingesetzt.

1. Introduction

1.1 Global insights into cancer

Cancer is a large group of diseases characterized by the uncontrollable growth of the body's cells, crossing their pre-defined boundaries, and resulting in their spread to nearby areas or farther parts of the body (Alberts et al., 2002). Global mortality data for the year 2020 reported nearly 19.3 million new cases of cancer and approximately 10.0 million cancer-related deaths worldwide (Sung et al., 2021). Frequently diagnosed cancers include breast, lung, colorectal, and liver cancers. In several countries, cancer is the leading cause of death, marked by an annual increase in incidence (Sung et al., 2021). This further highlights the urgent need to search for new druggable targets, given the current lack of effective therapy and the failure of presently used chemotherapeutics in terms of severe side effects and the development of resistance.

1.2 Cancer hallmarks

The "Hallmarks of Cancer," was first described as a set of defined biological capabilities acquired by cancer cells during tumor development by Hanahan and Weinberg in 2000. These hallmarks include evading growth suppressors, enabling replicative immortality, activating invasion and metastasis, sustaining proliferative signaling, inducing vasculature, and resisting cell death (Hanahan, 2022). Since then, additional hallmarks, such as avoiding immune destruction and deregulating cellular metabolism, as well as enabling characteristics like genome instability and mutation, were recognized. In 2022, Hanahan and Weinberg proposed new emerging hallmarks including non-mutational epigenetic reprogramming, senescent cells, polymorphic microbiomes, and unlocking phenotypic plasticity (Hanahan, 2022).

The regulation of normal mammalian cell proliferation involves various cell cycle regulators, such as cyclins and cyclin-dependent kinases (Cdks) (Otto & Sicinski, 2017). However, this regulation is disrupted in cancer, leading to uncontrolled and sustained proliferation. Targeting proliferation is a major focus in cancer treatments, with therapies aimed at inhibiting or disrupting cancer cell growth by targeting cell division mechanisms and signaling pathways. To provide valuable insights into cancer cell proliferation and survival, upon gene knockout or compound treatment, this thesis employed 2D and 3D cell culture models. A live cell imaging system has been used to measure cell confluency to study proliferation in 2D. The 3D cell culture models, known as multicellular tumors (MCTs) or spheroids, better mimic the *in vivo* tumor microenvironment in terms of the structural organization, oxygen and nutrient gradients, and pH conditions of *in vivo* solid tumors (Han, et al., 2021). Additionally, the clonogenic assay/colony formation assay assesses the ability of single adherent cells to survive and form clonal populations (Franken et al., 2006). This assay is commonly used in cancer drug screening to distinguish cells with proliferative capacity from those that do not.

Migration is a crucial aspect of cancer metastasis. Metastasis involves tumor cells leaving the primary site and spreading to other parts of the body, forming secondary sites (Novikov et al., 2020). The initial step in this process is invasion, where tumor cells breach the surrounding basement membrane and migrate through the extracellular matrix (ECM) into adjacent tissues (Novikov et al., 2020). Several factors within the tumor microenvironment, such as hypoxia, chemoattractants, ECM stiffness, and nutrient deprivation, drive cancer cells to search for a more favorable environment (Novikov et al., 2020). Notably, the phenomenon of epithelial-to-mesenchymal transition (EMT) holds significant importance during migration and invasion. Through EMT, tumor cells acquire plasticity, transitioning from a stationary epithelial state to a mobile mesenchymal state. This transition empowers cancer cells with malignant traits, including enhanced invasiveness and resistance to senescence, apoptosis, and treatment (Novikov et al., 2020). In this thesis, cell migration assays, such as the classical scratch assay, combined with live cell imaging have been employed to study the effect on tumor cell migration.

1.3 Natural compounds as anticancer agents

Natural compounds are those produced naturally from living organisms, such as plants, insects, animals, fungi, and microbes, and can be used to treat disease conditions in humans (Zhu et al., 2022). These compounds are still widely used up to date, as stated in a recent review by Newmann and Cragg (Newman & Cragg, 2020). The US FDA approved 547 natural drugs used between 1827 and 2013 for the treatment of conditions, primarily cancer, hypertension, and bacterial infections in the year 2016 (Patridge et al., 2016).

In the antitumor drug category, spanning from January 1981 to September 2019, out of a total of 185 small-molecule anticancer drugs, only 29 (15.7%) could be classified as entirely synthetic. The remainder can be categorized as originating from naturally inspired sources (Newman & Cragg, 2020). Popular examples of natural-origin anticancer drugs are taxanes, vinblastine, vincristine, and podophyllotoxin analogs (Naeem et al., 2022). These naturally derived anti-tumor compounds have been shown to act by several mechanisms, such as suppressing cell proliferation, regulating the cell cycle, interfering with some tumorigenic pathways, modulating antioxidant enzymes, and stimulating DNA repair mechanisms (Naeem et al., 2022). Furthermore, these drugs affect tumor cell differentiation, angiogenesis, apoptosis, and metastasis (**Figure 1**).

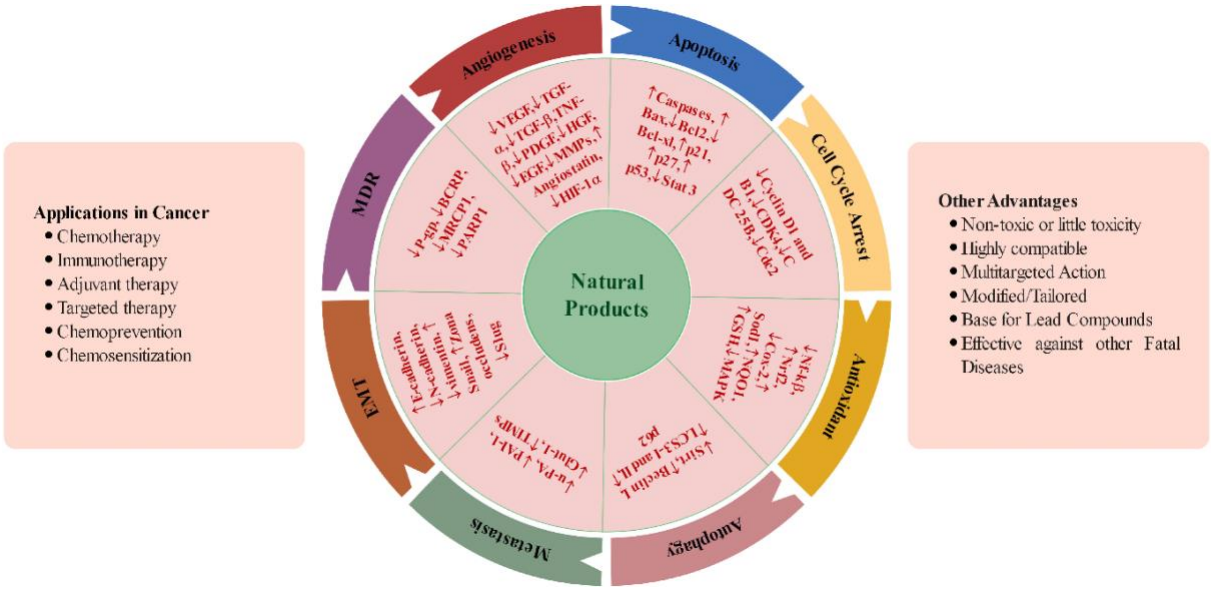

Figure 1. Natural products as anticancer agents (Naeem et al., 2022).

The limitations of conventional cancer therapies consist of high costs, toxicities arising from non-specific targeting, and increased chemoresistance that have been marked as serious challenges in the treatment of cancer (Naeem et al., 2022). On the other hand, natural products are expected to be major drug options in cancer as they offer higher efficacy, lesser toxicity, and multi-targeted action, and could serve as a base for developing lead compounds that can be modified effectively (Naeem et al., 2022). However, future studies must focus on investigating combinations of natural compounds or combinations of existing chemotherapeutics to overcome the limitation of bioavailability and develop an efficient drug delivery system. In this thesis, the naturally derived compounds auratryptanon and violacein have been studied for their potential as anticancer agents.

1.4 RNA binding proteins as anticancer targets

RNA binding proteins (RBPs) are proteins that are involved in the post-transcriptional regulatory layer, deciding the fate and function of each cell transcript and maintaining cellular homeostasis (Pereira et al., 2017). Upon binding of the RBP to coding and non-coding RNAs, a complex of ribonucleoprotein (RNP) is formed (Pereira et al., 2017). RBPs are involved in several cellular processes, such as alternative splicing, alternative polyadenylation, RNA modifications, mRNA stability, RNA localization, and mRNA translocation (Cen et al., 2023). RBPs are seen to be dysregulated in different types of cancer, affecting the expression and function of oncoproteins and tumor-suppressor proteins (Pereira et al., 2017). RBPs can serve as potential targets in cancer therapy and are involved in cancer initiation, development, and metastasis.

1.4.1 ELAVL1/HuR as an anticancer target

The RNA binding protein, human antigen R, commonly referred to as HuR, is an important post-transcriptional regulator belonging to the mammalian embryonic abnormal lethal vision-like (ELAVL) protein family and known as ELAVL1 (Wu & Xu, 2022). It is located on the minus strand and consists of 6 exons on human chromosome 19p13 (GRCh38.p14). Structurally, HuR is a 32 kDa protein (326 amino acids) and has three RNA recognition motif (RRM) domains, primarily RRM1 and 2, which support its binding to target mRNAs containing adenine and uridine-rich elements (AREs) (Schultz et al., 2020) (**Figure 2)**. A hinge between RRM2 and 3 is known as the HuR nucleoplasmic shuttling sequence (HNS), and plays a crucial role in translocating HuR from the nucleus to the cytoplasm (Schultz et al., 2020). HuR is primarily present within the nucleus but translocates to the cytoplasm in response to stress stimuli, such as hypoglycemia, hypoxia, radiation, and chemotherapy, stabilizing and translating its target mRNAs (Schultz et al., 2020).

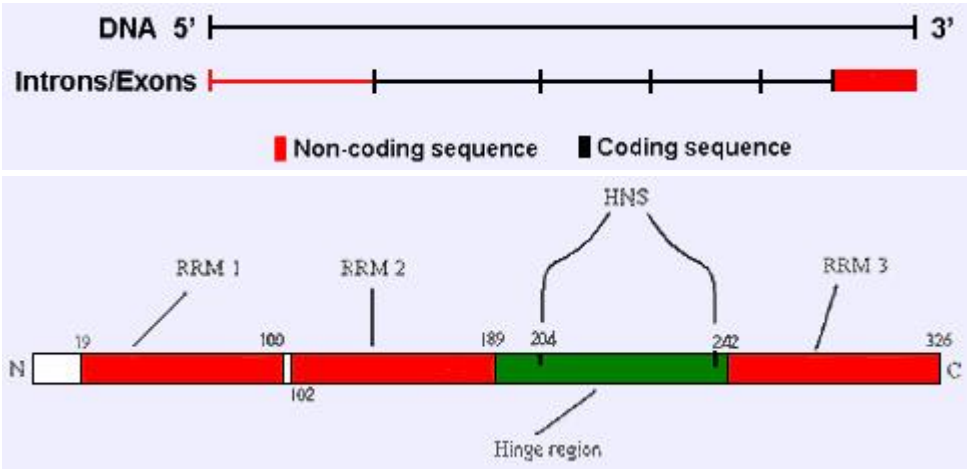

Figure 2. Gene and structure of ELAVL1/HuR (ELAVL1 (Embryonic Lethal, Abnormal Vision, Drosophila)-like 1 (Hu Antigen R), 2008). HNS: HuR nucleoplasmic shuttling sequence. Short vertical lines in the top panel showing sequence represent an exon, and the region in between the vertical lines denotes the intronic region.

HuR is a ubiquitous protein (found in many different cell types and tissues throughout the body), involved in regulating thousands of transcripts, influencing the expression and function of important genes involved in cell proliferation, maintaining cell homeostasis, inflammation, angiogenesis, and apoptosis (Wu & Xu, 2022). HuR is overexpressed in cancer in response to stress stimulators, such as hypoxia (Levy et al., 1998) and inflammation (Suswam et al., 2005). It binds to mRNAs encoding proto-oncogenes, growth factors, cytokines, and invasion-related factors, leading to a cancer-aggressive phenotype. Since HuR is essential for the proliferation, metastasis, growth, and survival of cancer cells, drugs targeting HuR may help regulate HuR-mediated tumorigenic effects (Schultz et al., 2020).

The initial discovery of HuR's role in carcinogenesis was noted in mice, exhibiting a tumor-promoting role in colon cancer cells (López De Silanes et al., 2003). High HuR levels were observed in cancer tissue compared to normal tissue, especially in the cytoplasm. Protein levels of HuR did not correspond with mRNA levels, which remained relatively stable (López De Silanes et al., 2003). Measuring protein levels is essential for understanding HuR's activity or its correlation with disease progression. Studies have examined HuR expression and explored the diagnostic and prognostic potential in different cancer types (Wu & Xu, 2022), including breast (Denkert et al., 2004), colon (Denkert et al., 2006), liver (Zhu et al., 2015), prostrate (Niesporek et al., 2008;Mitsunari et al., 2016), ovarian (Yi et al., 2009), pancreatic (Costantino et al., 2009; Richards et al., 2010), lung (Wang et al., 2009, 2011), and glioblastoma (Bolognani et al., 2012; Filippova et al., 2011).

Strategies have been put in place to target HuR in cancer therapy and to better understand its role in cancer. Firstly, downregulation/genetic inhibition of HuR expression by silencing or knockout using CRISPR, siRNA, or shRNA interference technologies has been used to validate HuR as an anticancer target (Schultz et al., 2020). Secondly, inhibition of the nucleo-cytoplasmic shuttling of HuR has been shown to block its function (Schultz et al., 2020). Inhibitors, such as MS-444, derived originally from *Micromonospora* and initially discovered as a myosin light chain kinase inhibitor (Schultz et al., 2020), were later found to inhibit the dimerization and trafficking of HuR in cancer (Blanco et al., 2016; Meisner et al., 2007).

The third strategy focuses on the inhibition of HuR-RNA interaction, thereby blocking its function. Small molecule inhibitors have been identified employing high-throughput screening that prevents the binding of HuR and a target mRNA. These methods use purified HuR protein and a target mRNA that bears a fluorescent label. Changes in the fluorescent polarization enable researchers to screen for compounds that hinder the interaction between HuR and the fluorescently labeled mRNA (Schultz et al., 2020). Inhibitors derived from coumarins, such as benzothiophene hydraxamate, dihydrotanshionone-I (DHTS), and tanshinone mimics disrupt this interaction and impair tumor growth in carcinoma models (D'Agostino et al., 2015; Wu&Xu,2022).

Due to the ubiquitous presence, certain factors do not make HuR an ideal target for cancer therapy. Since HuR may also have crucial functions in healthy cells, designing therapies that selectively target cancer cells while sparing healthy cells becomes a complex task. The therapy cannot effectively discriminate between cancer and healthy cells, potentially leading to severe side effects (X. Wu & Xu, 2022). Moreover, given that HuR is essential for fundamental cellular functions, there might be redundancy in the system. Inhibiting only HuR might not suffice to halt cancer growth, as there could be other proteins capable of compensating for its loss. Additionally, cancer cells could develop resistance to the therapy over time and discover ways to bypass the inhibition of a single protein by activating alternative pathways. The delivery of therapies targeting ubiquitous proteins throughout the body can be challenging, as the therapy needs to accurately reach the appropriate cells and tissues while minimizing off-target effects (X. Wu & Xu, 2022).

In this thesis, the CRISPR/Cas9-based approach was adopted for the knockout of HuR in breast and hepatocellular cancer cell lines to validate HuR as an anticancer target in these cancer entities. Previous research conducted by our collaborators combined Saturation Transfer Difference-Non-Magnetic Resonance (STD-NMR) and molecular modeling approaches to demonstrate the affinity of several natural compounds that target the interaction between HuR and mRNA (Vasile et al., 2018). Building on this work, our study focused on investigating the impact of two potential small molecule inhibitors, epicatechin (EC) and novobiocin (NovNa), on the proliferation of various cancer cell lines. Additionally, this thesis aimed to confirm the specificity of these compounds for HuR by employing CRISPR/Cas9-generated HuR knockout cells.

1.4.2 IGF2BP2/IMP2 as an anticancer target

The insulin-like growth factor 2 mRNA-binding protein 2 (IGF2BP2/IMP2/VICKZ2) is an RNA-binding protein, which is 66 kDa in size and composed of 599 amino acids. On the gene level, *IGF2BP2* consists of 16 exons, located on human chromosome 3q27.2 (GRCh38.p13) (Christiansen et al., 2009) (**Figure 3**). In this thesis, the protein form is denoted as IMP2, while the human and murine gene expressions are referred to as *IGF2BP2* and *Igf2bp2*, respectively. Structurally, IMP2 consists of two N-terminally situated RRM domains and a C-terminus end consisting of four K-homology (KH) domains (Christiansen et al., 2009) (**Figure 3**). There are altogether seven known splice variants of the protein, one being *p62/IGF2BP2-2*, a 62 kDa protein with 556 amino acids, but lacking exon 10 of *IGF2BP2* and in terms of structure, lack 43 amino acids between KH2 and KH3 (Christiansen et al., 2009).

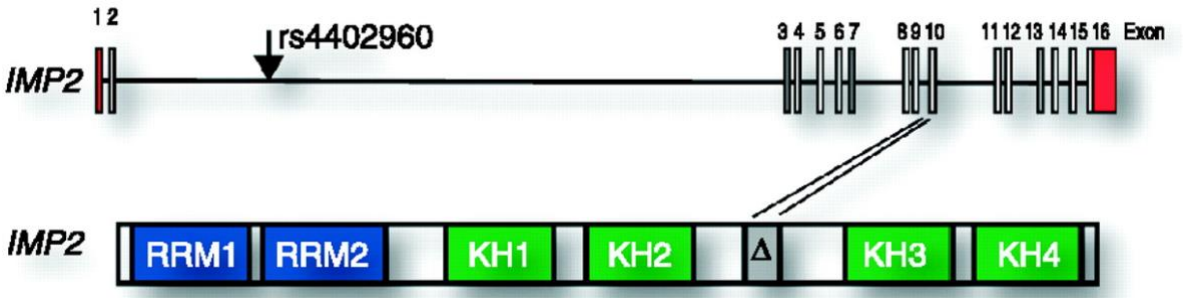

Figure 3. Gene and protein structure of IGF2BP2/IMP2 (Christiansen et al., 2009).

The other members of the IMP family, namely IMP1 and IMP3 are known to be an oncofetal protein that is dominantly expressed during embryonic development; however, its expression is ceased upon birth, but expressed in several adult organs (Czepukojc et al., 2019). However, the oncofetal nature of IMP2 is still unclear (Czepukojc et al., 2019). IMP2 plays a role in the development of type-2 diabetes by disrupting the secretion of insulin (Christiansen et al., 2009). The connection between IMP2 and human metabolic diseases is established through its post-transcriptional regulation of numerous genes across various cell types and pathways (Dai, 2020). Furthermore, *IGF2BP2* dysregulation has been associated with the progression of cancers and cancer stem cells (Cao et al., 2018). Recent studies have found that *IGF2BP2* is an

N6-methyladenosine (m6A) reader, which is the most abundant internal RNA modification present in eukaryotic cells (Maity & Das, 2016). *IGF2BP2* interacts with various types of RNAs, including microRNAs, messenger RNAs, and long non-coding RNAs, enabling the regulation of multiple biological processes (Dai et al., 2017; Li et al., 2017; Wu et al., 2019).

Numerous studies have demonstrated that IMP2 is overexpressed in several human cancers, leading to poor disease prognosis and shorter patient survival. Notable example types include colon (Bigagli et al. 2016; Cui et al. 2021; Dahlem et al. 2022; T. Liu et al., 2023), liver (Dahlem et al. 2022; Pu et al. 2020), and lung (Han et al. 2022), breast (Barghash et al., 2015), pancreatic (Dahlem et al., 2019), gall bladder (Kessler et al., 2017), head and neck squamous cell carcinoma (Deng et al., 2020), and esophageal carcinoma (Barghash et al., 2016).

Previous investigations using siRNA-mediated knockdown of IMP2 have indicated its crucial role in promoting tumor cell hallmarks, including cell proliferation and migration in cancer (Xu et al. 2019; Cui et al., 2021; Cao et al., 2023; Dong et al., 2021). However, siRNA-mediated knockdown offers only temporary gene silencing at the mRNA level (Boettcher and Mcmanus. 2015). In contrast, CRISPR/Cas9-based gene editing provides a permanent and precise approach to induce frameshift mutations and protein knockout, enabling a deeper understanding of the protein of interest (Gomy et al., 2020). Additionally, the specificity and reduced off-target effects of CRISPR/Cas9, including its variation, the prime editing, make it desirable for generating stable cell lines with different mutations in the gene of interest (Smith et al. 2017; Anzalone et al. 2019; Giuliano et al., 2019).

In this thesis, a CRISPR/Cas9-based gene editing approach was employed to obtain IMP2 knockouts and explore their effect on hallmarks of cancer, such as proliferation, and migration. Moreover, recently our group performed IMP2-directed biophysical compound screening using fluorescence polarization to identify IMP2 inhibitors (Dahlem, Abuhaliema, et al., 2022). The identified hits act as protein-RNA interaction inhibitors and have been confirmed to bind to the protein surface of the interaction interface by using additional biophysical methods (i.e., thermal shift assay and STD-NMR). Employing these inhibitors in wild-type and IMP2 knockout cells, we showed strong target-dependent effects hinting at a suitable specificity (Dahlem, Abuhaliema, et al., 2022). By employing gene editing and small molecule inhibitors, this thesis aimed to verify IMP2 as a tumor promoter in liver, colon, and lung cancer entities. Other small molecule inhibitors of IMP2 have also been recently employed as an anticancer therapy (Feng et al., 2022; Weng et al., 2022).

1.5 *The clustered regularly interspaced short palindromic repeats/CRISPR-associated Cas9 (CRISPR/Cas9) technology*

The development of immunity to limit the spread of harmful mobile genetic elements has been observed in prokaryotes (Garrett, 2021). One such known tool is the clustered regularly interspaced short palindromic repeats/CRISPR-associated Cas9 (CRISPR-Cas9) system that stores information on the potential harmful genetic elements in an array, which are described as spacers (Garrett, 2021). These spacers serve as a memory of the DNA encountered as a result

of previous invaders. In recent years, CRISPR-based gene editing has been widely applied in the fields of medicine, biotechnology, and agriculture (Gomy et al., 2020). The CRISPR/Cas9 system consists of two components. The first component consists of the Cas9 endonuclease, which acts as molecular scissors to cut the gene at the target site with the help of its two parts, RuvC and HNH (Gomy et al., 2020). The second component of the system is the single guide RNA (sgRNA). It carries the scaffold sequence, binds to Cas9, and recognizes the spacer sequence that is complementary to the gene of interest. This recognition occurs adjacent to the proto-spacer adjacent motif (PAM) sequence. As a result, the sgRNA guides the CRISPR/Cas9 complex to the intended site of editing in the genome (Gomy et al., 2020).

The editing process relies on one of two DNA repair mechanisms: non-homologous end-joining (NHEJ) or homology-directed repair (HDR) (**Figure 4**). The default DNA repair pathway in the human system is NHEJ, which involves the random insertion or deletion of base pairs, resulting in indels at the site of the cut (Gomy et al., 2020). This pathway disrupts the genetic sequence through frameshift mutations to achieve gene knockouts. On the other hand, HDR is an error-free but less efficient pathway that utilizes the homologous region of the target DNA strand as a template to correct the disrupted DNA, resulting in precise targeted mutations (Gomy et al., 2020).

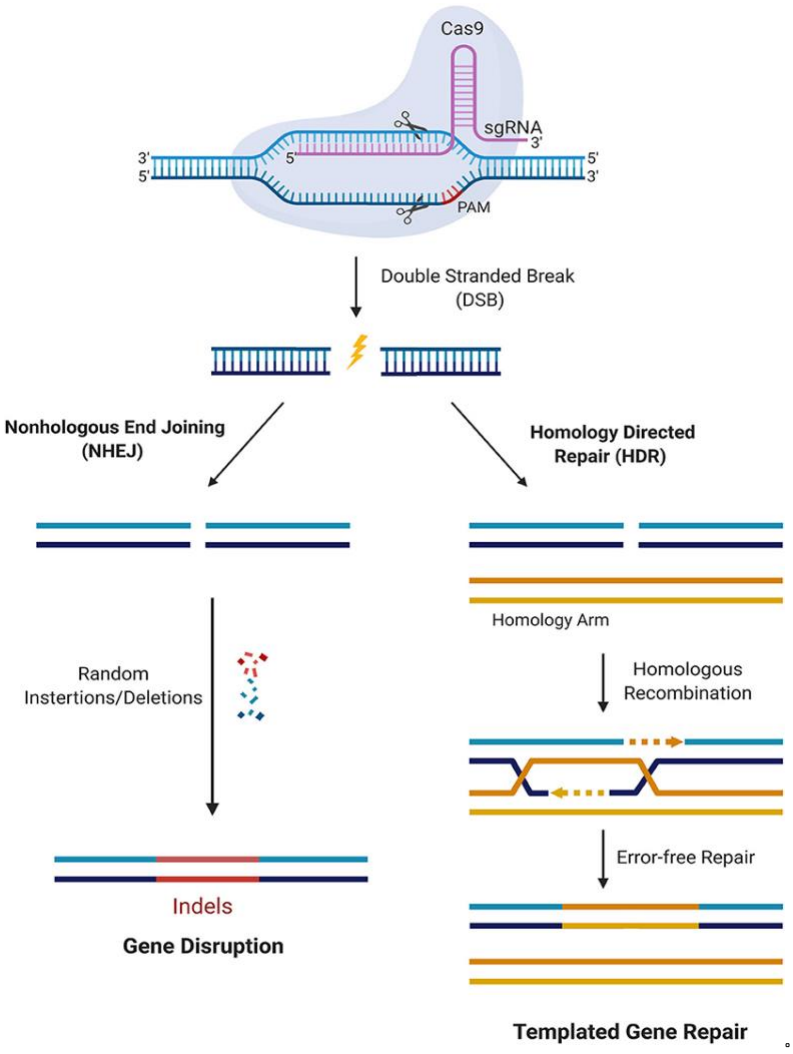

Figure 4. The mechanism of CRISPR/Cas9-mediated gene editing (Gomy et al., 2020).

The most recent strategy for precise gene editing, prime editing is used to insert or delete a desired part of the target without inducing double-strand breaks (Anzalone et al., 2019). It utilizes a prime editor composed of a Cas9 nickase fused to a reverse transcriptase (RT) obtained from Wild-type Moloney murine leukemia virus (MMLV). A prime editing gRNA (pegRNA) is utilized to achieve precise genome editing and consists of the spacer sequence, directing the prime editor to the target site in the genome, and has a 3′ extension encoding the sequence of the desired edit (Anzalone et al., 2019). Once inside the cell, the complex of the prime editor and pegRNA binds to the target site in the genome, complementary to the spacer sequence of the pegRNA, and creates a nick in the single-stranded DNA (ssDNA) by the prime editor. The 3′ end of the DNA is released by the nick, which then hybridizes to the pegRNA extension and performs reverse transcription of the pegRNA template region. This process is followed by 3′ flap equilibration and 5′ flap excision. The ligation of the nick forms a heteroduplex, with one strand containing the edit. Finally, the prime edit becomes permanent through the DNA repair mechanism or during replication, resulting in copies with the desired edit in the complementary strand (**Figure 5**). This approach can be used for small-base insertions, deletions, and single-base substitutions with lower off-target activity in human cells (Anzalone et al., 2019).

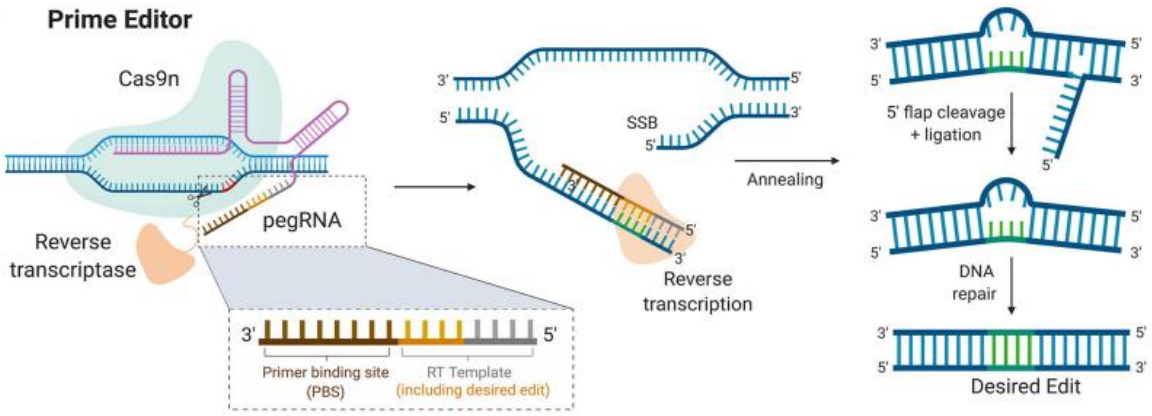

Figure 5. Prime editing-mediated gene editing (Gomy et al., 2020)

Using safe harbor loci as target sites to establish negative control for prime editing:

Safe harbor loci (SHL) are specific regions in the genome where new genetic information or genetic alterations can be introduced without negatively affecting function or posing risks to the host cell (Papapetrou & Schambach, 2016). The safe harbor loci include adeno-associated virus site 1 (*AAVS1*) and C-C chemokine receptor type 5 (*CCR5)* in humans, and reverse-oriented splice acceptor, clone 26 (*Rosa26*) in mice (Shrestha et al., 2022).

AAVS1 is situated on human chromosome 19 q13.42 and contains the *PPP1R12C* gene, encoding a myosin phosphatase subunit (Surks et al., 2003). Successful editing of this locus has been achieved in hematopoietic stem cell (HSC) patients by integrating a transgene cassette

with or without an exogenous promoter, treating conditions like Fanconi anemia (Diez et al., 2017) and X-linked chronic granulomatous disease (X-CGD) (De Ravin et al., 2016). In mice, the Rosa26 locus, located on chromosome 3 p25.31, has proven to be a reliable site for transgenesis through DNA cassette integration (Zambrowicz et al., 1997). Successful *in vivo* targeting of this locus has been demonstrated using the CRISPR/Cas9 technique to introduce coagulation Factor IX (FIX) (Stephens et al., 2019) or human alpha-1-antitrypsin genes (Stephens et al., 2018) into mouse livers. Although a human homolog of the *Rosa26* locus is present on chromosome 3 at position 3p25.3 (Irion et al., 2007), the safety and effectiveness of targeted integration in humans have not been thoroughly studied.

This thesis focuses on targeting the SHL to establish negative controls for the prime editing approach, utilizing *AAVS1* in the human (HCT116) system and *Rosa26* in the murine (LLC1) system.

Gene knockout generation using CRISPR/Cas9:

Some general points need to be considered before designing a gRNA for achieving CRISPR/Cas9-generated gene knockout. When employing *S. pyogenes* Cas9 (SpCas9), both [5'-20nt-NGG] and [5'-CCN-20nt] are potential target sites and equally efficient for targeting the coding or non-coding strand of the DNA. It is important to avoid sites that code for amino acids near the N-terminus of the protein to reduce the chances of the cell using an alternative ATG downstream of the annotated start codon. Similarly, target sites that code for amino acids near the C-terminus of the protein must also be avoided to maximize the chances of producing a non-functional allele (Doench, 2017).

For a 1-kilobase gene, potential target sites would appear approximately once every 8 nucleotides, resulting in dozens of potential gRNAs to choose from. There are several online computational tools available to grade gRNAs based on sgRNA-dependent off-target effects (Guo et al., 2023). While these computational tools are not perfect, they can serve as a basis for narrowing down the number of guides to be tested in the lab. Checking for the off-target potential of the guide is important. It is preferable to choose a guide with low to no off-target activity even with a low on-target activity rather than one with high off-target and high on-target activity (Anthon et al., 2022).

In this thesis, three different approaches based on CRISPR/Cas9 have been employed. For the knockout of HuR, Cas9/sgRNA ribonucleoprotein complexes (RNPs) were used to target and edit DNA. Secondly, to achieve IMP2 knockout, a single plasmid was employed that encoded for the Cas9, gRNA, and a selection marker, Green Fluorescent Protein (GFP) that makes the cell appear fluorescent green upon the plasmid's successful uptake into the cell. The Prime editing system 2 generates IMP2 knockouts as well as targets the SHL mentioned earlier. This involved a two-plasmid system, with one encoding GFP and Cas9, and the other encoding the pegRNA.

As a result of CRISPR/Cas9-mediated indel formation, the edit may occur in one or both alleles, resulting in monoallelic and biallelic knockouts, respectively. To achieve a complete knockout of the protein of interest, both copies of the gene need to be edited. In this thesis, successful monoallelic HuR knockout and biallelic IMP2 knockout have been achieved.

2. Objectives

This work consists of two parts as follows:

I) The first part of this project was to characterize the natural compound violacein as a potential anticancer agent.

II) The second part of this project focused on the *in vitro* validation of the RNA binding proteins ELAVL1/HuR and IGF2BP2/IMP2 as potential anticancer targets.

3. Materials and Methods

3.1 Cell culture

3.1.1 Cultivation of cell lines

The tumor cell lines were cultured in RMPI-1640 (A549, Huh7, LLC1, T47D) or DMEM (HCT116, MCF7, MDAMB-231, HepG2, SW480, PANC-1) medium, supplemented with 10% FCS, 100 U/100 µg/ml penicillin/streptomycin, and 2 mM glutamine unless otherwise specified. The cells were maintained at 37°C in a 5% CO_2 humidified atmosphere. Sub-culturing followed the ATCC recommendations: Cells were rinsed once with 1X PBS buffer (2.7 mM KCl, 1.8 mM KH_2PO_4, 137 mM NaCl, and 10 mM Na_2HPO_4 in distilled water; pH adjusted to 7.4, then autoclaved), detached with trypsin-EDTA, and the reaction was halted with culture medium. The cell suspensions were centrifuged for 5 min at 250 x g, and the resulting pellets were resuspended in full growth media. This suspension was used for seeding cells in experiments, and suitable aliquots were used for passaging.

3.1.2 Cell freezing and thawing

To preserve the cells, they were detached, and the resulting cell suspension was centrifuged and resuspended in a solution of 10% DMSO prepared in FCS. The cells were then divided into cryovials, frozen at -80°C, and transferred to a liquid nitrogen tank for long-term storage. Thawing involved warming the cryovials in a 37°C water bath and quickly adding them to a pre-warmed medium to create a cell suspension. The cells were then centrifuged, and the medium was replaced with fresh media to get rid of the toxicity that could arise from the DMSO used for freezing. Culturing of the cells was carried out as described in *3.1.1*.

3.1.3 Cultivation of doxorubicin-resistant cells

Huh7 cells were cultured as described in *3.1.1* and made doxorubicin-resistant over several months by increasing the concentration of doxorubicin. The chemoresistance in Huh7 cells was maintained by treatment with 2 µM doxorubicin (Alfa Aesar #J64000) every twice a week for 24 h. The confirmation of doxorubicin resistance was done by MTT assay. Cells were seeded in 100 µl per well in a 96-well plate without doxorubicin, the day before compound treatment.

3.1.4 Cell proliferation in 2D

The IncuCyte® S3 system was employed to monitor 2D cell proliferation. 3000 cells per 100 µl per well were seeded into a 96-well plate. Cell confluency was measured every 8 h starting from the time point of seeding until 72 h and analyzed using the basic analyzer software. Cell confluence was normalized to the 0 h time point. Metabolic activity was measured 72 h after seeding using the MTT assay. For each compound, the effect on the 2D cell proliferation was

calculated for each concentration and normalized to its respective DMSO control or untreated control (if DMSO control showed no effect on proliferation).

3.1.5 MTT assay

Cell viability/metabolic activity upon compound treatment was performed using an MTT assay. Depending on cell type, 60000-70000 cells per 100 µl per well were seeded into a 96-well plate. The next day, treatment stock solutions were prepared in DMSO, and solvent controls were added to the cells. The viability of adherent cells was measured 72 h after compound treatment unless stated otherwise. Media was replaced with 0.5 mg/ml MTT solution (3-(4,5-dimethylthiazole-2-yl)-2,5 diphenyltetrazolium bromide) (Sigma-Aldrich #M5655) in the respective culture medium. After incubation, the cells were lysed in DMSO, and the absorbance was measured at 560 nm using a microplate reader. For each compound treatment, the inhibition of cell viability was calculated for each concentration and normalized to its respective DMSO control or untreated control (if DMSO control showed viability above 90%).

3.1.6 3D proliferation/spheroid formation assay

For the assessment of the spheroid-forming ability of cells, the IncuCyte® S3 system was utilized. 3000 cells per 100 µl per well were seeded in low-attachment U-bottom 96-well plates (Band #781900), and the spheroid formation was monitored for 6 days. For HCT116 cells, the spheroid area was normalized to the 2-d old spheroid (the time point of complete spheroid formation). In cell lines, where spheroid formation could not take place, representative images of the cells were shown at 6 d.

3.1.7 Migration measurements

80,000 cells were seeded per 100 µl per well into Image Lock 96-well plates. On the following day, the wound maker tool was used to perform scratches into the cell monolayers. The media containing the detached cells were removed and replaced with media without FCS. The treatment stock solutions were prepared in DMSO, and solvent controls were added to the cells after replacement with FCS-free media. Migration was observed every 8 h up to 48 h after scratching. Cell confluency in the wound area was analyzed using IncuCyte® S3 migration software. For each compound treatment, cell migration was calculated for each concentration and normalized to its respective DMSO control or untreated control (if DMSO control showed no effect on cell migration).

3.1.8 Colony formation assay

Using serial dilution, 300 cells per 2 ml per well were seeded in a 6-well plate. For compound treatment, solvent control (0.1% DMSO dissolved in respective media) was also tested, and compounds were added to the well at the time of seeding. Cells were allowed to grow for 1-2 weeks to assess colony formation ability. The media was removed, and cells were washed once

carefully using 1X PBS. The live colonies were imaged using the IncuCyte® S3 system. The confluence area was measured for colonies consisting of at least 50 cells per colony, which corresponded to an object area of at least 1 X 10^4 - 2 X 10^4 μm^2 depending on the cell type and the cut-off mask was applied accordingly. The object counts per well module provided the total count of the colonies per well. The object average area module provided the average colony area per well. The inhibition of colony formation activity was calculated by normalizing to its untreated control (if solvent control did not show any difference in the number and size of the colony in comparison to the untreated).

3.1.9 ROS measurement

To measure the reactive oxygen species (ROS) particularly hydrogen peroxide in the tumor cell supernatant, the homovanillic acid (HVA) oxidation assay was conducted. Fresh HVA assay solution was prepared composed of 0.1 mM HVA and 4 U/ml horse radish peroxidase (HRP) in 1X PBS. Care was taken to protect the solution from light. Cells were washed once with 1X PBS, followed by the addition of 150 µl HVA assay solution. Plates were incubated at 37°C for 1 h, well protected from light. Next, 100 µl supernatant was transferred into a white 96-well plate. The reaction was stopped by the addition of 5 µl stop solution (0.1 M glycine, 0.1 M NaOH, 25 mM EDTA). Fluorescence was measured at excitation (312 nm) and emission (420 nm) wavelength using a microplate reader (GloMax™).

3.2 Determination of protein concentrations

The Pierce BCA protein assay kit (Thermo Fisher Scientific #23225) was used to determine the protein concentration following the manufacturer's instructions.

3.3 Bacterial culture

3.3.1 Transformation

The *E. coli* strain GT116 (Invivogen, San Diego, CA, USA) was used as the host organism for plasmid amplification. Chemically competent *E. coli* GT116 (50 µl) were mixed with 50 ng of plasmid solution and incubated on ice for 20 min. The bacteria were then heat-shocked at 42°C for 40 s and returned to the ice for an additional 2 min. The bacteria were resuspended in 900 µl of pre-warmed LBamp medium (autoclaved LBamp medium supplemented with 100 µg/ml ampicillin) and incubated at 37°C and 250 rpm for 1.5 h. Subsequently, 100-500 µl of the suspension was plated on LBamp plates (1.5% agar in LBamp medium) and incubated overnight.

3.3.2 Plasmid isolation

Single colonies were selected from the agar plates to prepare liquid overnight cultures. Plasmids were isolated from the overnight cultures using the High Pure Plasmid Isolation Kit according to the manufacturer's protocol (Roche #11754777001). The concentration of

plasmid DNA was measured at 260 nm, and its purity was assessed by the A260/280 ratio using a Thermo Scientific NanoDrop Lite Spectrophotometer (Wilmington, DE, USA).

3.4 Development of HuR knockout tumor cell lines *via* CRISPR/Cas9-mediated RNP delivery of Cas9: sgRNA

The CRISPR/Cas9 technique was used to disrupt the *ELAVL1* in breast carcinoma (MDAMB231) and hepatocellular carcinoma (HepG2) cell lines by ribonucleoprotein delivery (RNP) using a transient transfection and clonal expansion approach. Two designed synthetic TrueGuide™ single guide (sg) RNAs were obtained from Thermo Fisher Scientific, targeting two different exons as shown in **Table 1**. Designing tools such as CHOPCHOP (https://chopchop.cbu.uib.no/) and CRISPOR (http://crispor.tefor.net/) were employed to cross-check on-target activity and off-targets of the sgRNAs employed.

Table 1. sgRNAs designed for HuR knockout.

Name	**sgRNA sequence (5‘-3‘)**	**Target region**
gRNA3	TGTGAACTACGTGACCGCGA	Exon 3
gRNA4	TTGGGCGGATCATCAACTCG	Exon 4

The ribonucleoprotein delivery of Cas9 utilizes the cell's error-prone repair mechanism c-NHEJ to randomly create small indels after a double-strand break at a target site. The target sites were chosen due to the following reasons: (i) close distance to the start site of the *ELAVL1* gene, (ii) all exons encode a part of RRM2 as an important protein domain.

In a 12-well format, cells at 30-70% confluency were transfected with synthetic sgRNA and recombinant Cas9 protein (TrueCut™ Cas9 Protein v2, #A36496, Thermo Fisher Scientific) using the Lipofectamine™ CRISPRMAX™ Cas9 transfection reagent (#CMAX00001, Thermo Fisher Scientific) according to the manufacturer’s instructions. 48 h post-transfection, the cells were detached and counted. A portion of the cells was used for clonal expansion following the limiting dilution cloning procedure, where the cells were seeded at a density of 0.8 cells per well per 100 µl in a 96-well plate and nine plates were prepared each time. The surviving clones obtained after clonal expansion were collected for gDNA extraction, PCR amplification of the edited region, and Sanger sequencing analysis. Once the editing was confirmed by sequencing analysis, the reduced expression of HuR was validated by western blot analysis. The monoallelic HuR MDAMB-231 knockout clone mKO#1 was re-CRISPRed as described above, however, this could not result in a biallelic knockout of HuR.

3.5 Development of IMP2 knockout tumor cell lines

3.5.1 Approach 1: Prime editing

Design of prime editor 2 system

The prime editor 2 system was used to achieve *IGF2BP2* knockout in SW480, HepG2, Huh7, and A549 cells and *AAVS1* in HCT116 cells. In the murine system, this approach was used to achieve *Ifg2bp2* and *Rosa26* knockout in LLC1 cells. Here, pCMV-PE2-P2A-GFP (plasmid #132776, Addgene, **Supplementary Figure 9**) and pU6-pegRNA-GG-acceptor (plasmid #132777, Addgene, **Supplementary Figure 10**) were a gift from David R. Liu (Anzalone et al., 2019). The pegRNA acceptor (pU6- pegRNA-GG-acceptor) was employed as a vector to deliver the pegRNA component and the designed pegRNAs were inserted into the vector by golden gate cloning as described previously (Anzalone et al., 2019).

The spacer targeting different loci of exon 6 of human and murine IGF2BP2 served as a basis for the pegRNA assembly. The design criteria for the pegRNA vector used in this study were based on several considerations from previous research (Anzalone et al., 2019). Firstly, the pU6-pegRNA-GG-acceptor vector utilized a U6 promoter, which requires an adenine or guanine as the first base at the 5' end of the spacer for efficient transcription by human RNA polymerase III (Gao et al., 2017; Ma et al., 2014). Secondly, it was noted that TT- and GCC motifs within the last four bases of the targeting sequence can significantly reduce the efficiency of CRISPR/Cas9-mediated gene editing, as demonstrated (Graf et al., 2019). Therefore, these motifs were avoided in the design. On the other hand, purines located near the protospacer adjacent motif (PAM) were found to slightly enhance knockout efficiency.
Additionally, considerations were given to the recommendations of Wong et al., 2015, who reported that stretches of at least four contiguous RNA bases and the presence of a UUU-motif within the last six bases of the targeting sequence (seed region) were associated with poor CRISPR activity. Consequently, these sequences were avoided in the design.
To prevent further editing of the mutated sequence, the desired mutations were planned to disrupt the PAM of the spacer sequences. The length of the primer-binding site (PBS) and the size of the reverse transcriptase (RT) template were determined following the guidelines provided by PrimeDesign (https://drugthatgene.pinellolab.partners.org/). For the design of the spacer sequences tools like CHOPCHOP (https://chopchop.cbu.uib.no/) and CRISPOR (http://crispor.tefor.net/) were used to crosscheck on-target activity and off-targets.

Note that the designing and preparation of the pegRNA4_-GG_16ntRT (pegRNA4_16) and the biallelic IMP2 knockout HCT116 cells were generated by Dr. Tarek Kröhler (Dahlem, Abuhaliema, et al., 2022). The pegRNA4_16 was used to attain IMP2 knockout in SW480, HepG2, Huh7, and A549 cells. The pegRNAs designed, prepared, and attempted for knockout are listed in **Table 2**.

Table 2. Design of pegRNAs with the desired deletion.
Sequences of the single components, including a spacer, linked to the common sgRNA scaffold:5'AGAGCTAGAAATAGCAAGTTAAAATAAGGCTAGTCCGTTATCAACTTGAAAAAGTGGCACCGAGTCG-3'), and the 3'extension. PBS: primer-binding site, RTT: reverse transcriptase template.

Gene Name	**pegRNA abbreviation**	**sgSpacer (5'-3')**	**pegRNA 3'extension (5'-3')**	**PBS length**	**RTT length**	**Deletion intended**
IGF2BP2	pegRNA4_16	AGAGCCATGGAGAAGCTAAG	CAAACTGATGCGCTTAGCTTCTCCATGG	13	16	-GG
AAVS1	pegRNA1	GGGGCCACTAGGGACAGGAT	ATGGGGCTTTTCTGTAATCCTGTCCCTAGTG	12	19	-GGTG
	pegRNA2	GGGACCACCTTATATTCCCA	ACATTAACCGGCTGGGAATATAAGGTGGTCC	15	16	-GG
Rosa26	pegRNAa	GGTAGGCCTAGCACATGATC	GGGTTTCCCTGCACTTGATCATGTGCTAGGC	12	19	-ATCC
	pegRNAb	GGAAAAGTCTCCACCGGACG	GAGCCATGGGCGTCCGGTGGAGACT	12	15	-GG
Ifg2bp2	pegRNAI	GAGAGCTCACCTCTTCATCG	AAGATTTCCTACATCCGATGAAGAGGTGAGCTC	15	18	-GG
	pegRNAII	GATGATGGCACCAACAAACT	GATCCTGGTCCCCACAGTTTGTTGGTGCCA	12	18	-GG

The knockout procedure:

In 24-well plates, 100,000 cells per 500 µl well were seeded and incubated overnight. The following morning (after 16-24 h), the transfection was carried out when the cells reached approximately 60% confluency. Lipofectamine 3000 (Thermo Fisher Scientific) was employed for transfection, and an equimolar ratio of the two vectors of the prime editing system was used to obtain 2 µg of total DNA, according to the manufacturer's instructions. Transfection efficiency was assessed at 48 h post-transfection by measuring the green-fluorescent area

(expressed by the GFP-positive cells) of the cells using the IncuCyte® S3 system (Sartorius, Göttingen, Germany). For hepatocellular carcinoma cell lines, HepG2 and Huh7, the jet PEI hepatocyte DNA transfection reagent (Polyplus) was used as per the manufacturer's instructions and based on trials, media was changed 4 h post-transfection to prevent toxicity associated with the transfection components. The transfection efficiency was checked at 24 h post-transfection, followed by single-cell cloning. For the experiment performed to verify transfection using the jet PEI hepatocyte DNA transfection reagent in HepG2 and Huh7 cells, *IMP2* overexpressing (pcDNA3-GFP-IMP2-2, **Supplementary Figure 7**) and *IMP2* control plasmid (pcDNA3-GFP-IMP2-2_antisense-control, **Supplementary Figure 8**) established previously in our lab was used (Kessler et al., 2013). The GFP forward primer, 5'-TACCCCGACCACATGAAGCAG-3' and GFP reverse primer, 5'-TCGTCCATGCCGAGAGTGATCC-3' used to quantify the GFP of the pCMV-PE2-P2A-GFP, to validate the successful transfection in the liver cancer cell lines using the above-mentioned transfection reagent.

Two different methods were established to perform single-cell cloning by using GFP as a selection marker, as follows:

A) Single-cell printer-mediated single-cell cloning: Optimizations were implemented to isolate individual GFP-positive cells, which were successfully transfected using the prime editing approach, from a mixture of GFP-positive and non-GFP-positive cells. This was achieved using the single-cell printer (SCP), known as f.sight™ (Cytena). Before the single-cell printing process, the cells were detached from the plates and underwent a single wash by centrifugation (400 x g, 2 min) using 1X PBS. Subsequently, they were resuspended in 1X PBS at a final concentration ranging between 10^5 and 10^6 cells/ml. For each experiment, a new sterile cartridge with a 40 µm nozzle was filled with 30 µl of the cell suspension and mounted on the SCP. The piezo stroke length was set to 10 µm, and the downstroke velocity was maintained at 140 +/- 10 µm/s to ensure stable droplet formation. Individual cells were then printed into the wells of a standard 96-well plate, which had been pre-filled with pre-warmed, pre-conditioned media prepared using 24 h conditioned cell culture medium from parental wild-type cells, sterile filtered, and adjusted to 20% FCS.

   The use of the SCP presented challenges after the centrifugation step, as the cells could not be resuspended in the culture media due to the presence of proteins which led to the blockage of the cartridge nozzle with air bubbles, rendering it unusable. As a result, the cells could only be resuspended in 1X PBS which made the process time-constrained requiring the process of single-cell printing to be completed within 5 min. Prolonged exposure to non-optimal conditions could compromise the viability of the transfected cells, making it crucial to work efficiently. To mitigate these issues, only up to 15 wells of a 96-well plate were seeded with cells at a time. It is worth noting that while the f.sight™ system supported the growth of non-transfected cells (SW480), it did not favor the formation of transfected GFP-positive single-cell colonies. To overcome these

challenges associated with f.sight™, an alternative method of manual cell picking was employed.

B) Manual cell-picking-mediated single-cell cloning: To obtain a single-cell suspension, the detached cells were resuspended in a medium. Under a microscope, the GFP-positive cells were manually picked using a glass capillary by Dr. Konstantin Lepikhov from the Institute of Genetics/Epigenetics, Saarland University, Saarbrücken, Germany. The picked cells were then transferred into 60 mm Petri dishes, where a grid with squares (0.5 cm apart from each other) was drawn on the bottom of the dishes to ensure enough spaces between the picked cells so that the resulting colonies would not overlap. To support the growth of clones, a sterile-filtered 48 h conditioned cell culture medium from wild-type cells, supplemented with 20% FCS was utilized. Once the clones reached a sufficient growth point, they were then transferred into a 96-well plate and subsequently cultured in a 24-well plate. They were maintained in culture until the knockout of IMP2 was verified by Sanger sequencing using CRISP-ID to analyze the sequencing results (Dehairs et al., 2016), followed by Western blot analysis.

3.5.2 Approach 2: Plasmid-based CRISPR/Cas9-mediated development of IMP2 knockout tumor cells lines.

Design of CRISPR/Cas9 system

The CRISPR/Cas9 system was used to achieve IMP2 knockout in A549, Huh7 cells, and LLC1 cells. In this system, pSpCas9(BB)-2A-GFP (PX458, Addgene plasmid #48138, **Supplementary Figure 11**) plasmid construct was used. Cas9-GFP fusion protein expression cassette was combined with U6-promotor driven sgRNA expression in the single plasmid. Restriction enzyme cloning was employed to insert designed gRNAs into the PX458 plasmid construct. The plasmid PX458 was digested with restriction enzyme BbsIHF® (NEB #R3539) as per the manufacturer's protocol. Two different gRNAs targeting *IGF2BP2* designated as gRNA1 and gRNA2 were used, while gRNAI and gRNAII were used to obtain *Ifg2bp2* knockout (**Table 3**). The design criteria, tools, and the transfection method employed were as described in *3.5.1*, however, the total DNA used for the transfection was 1 µg.

Table 3. The gRNA sequences for IMP2 knockout.

Name	**Sequence 5'-3'**	**Target region**
IGF2BP2 gRNA1	GGGCTCGCTGAGGGGGCGAA	Exon 6
IGF2BP2 gRNA2	GTGGGGACCAGGATCCGCAG	Exon 6
Ifg2bp2 gRNAI	GAGAGCTCACCTCTTCATCG	Exon 6
Ifg2bp2 gRNAII	GATGATGGCACCAACAAACT	Exon 6

The designed gRNAs were ordered as oligos from Eurofins genomics and care was taken that they were of HPLC purified (**Table 4**). The oligos were phosphorylated using T4 Polynucleotide Kinase (NEB#M0201S) kit as per the manufacturer's instructions and thereafter annealed to form a duplex.

Table 4. Top and bottom oligo sequences for IMP2 knockout.

Name	**Sequence 5'-3'**
IGF2BP2 gRNA1 top oligo	CACCGGGCTCGCTGAGGGGGCGAA
IGF2BP2 gRNA1 bottom oligo	AAACTTCGCCCCCTCAGCGAGCCC
IGF2BP2 gRNA2 top oligo	CACCGTGGGGACCAGGATCCGCAG
IGF2BP2 gRNA2 bottom oligo	AAACCTGCGGATCCTGGTCCCCAC
Ifg2bp2 gRNAI top oligo	CACCGAGAGCTCACCTCTTCATCG
Ifg2bp2 gRNAI bottom oligo	AAACCGATGAAGAGGTGAGCTCTC
Ifg2bp2 gRNAII top oligo	CACCGATGATGGCACCAACAAACT
Ifg2bp2 gRNAII bottom oligo	AAACAGTTTGTTGGTGCCATCATC

Each of the 20 µl mixes of the top and bottom oligo was incubated at 37°C for 60 min in the cycler T100 in separate PCR tubes. The 20 µl of the top and bottom oligo were pooled together to get the final product of 40 µl with the final oligo duplex concentration of 0.5 µM.

The oligos were set to anneal as follows:

denaturation	95°C 3 min
annealing °C	50°C 5 min
gradual cooling	37°C 5 min
final cooling	12°C, ∞

The annealed oligos were ligated using T4 DNA Ligase (NEB# M0202S) kit into the digested plasmid PX458 as per the manufacturer's instructions. The ligated product was then transformed into GT116 competent cells, and the ligated plasmid was isolated as mentioned in 3.3. The insertion of the desired oligo into the plasmid PX450 was verified by Sanger sequencing confirming the success of the cloning.

The development of knockout cells was performed as described in *3.5.1* using manual cell picking.

3.6 Sanger sequencing analysis

According to the manufacturer's instructions, gDNA was extracted using QuickExtract™ DNA Extraction Solution (#101094, Biozym, Hessisch Oldendorf, Germany). PCR amplification was carried out using primers designed for amplifying the edited region (**Table 5**) with slight modifications: 4 µl of the DNA extract was added to a master mix consisting of 5 µl HOT FIREPol® EvaGreen® qPCR Mix Plus (#08-25-00020, Solis BioDyne, Tartu,

Estonia), 14.5 µl molecular biology-grade water (#A7398,0500, AppliChem, Darmstadt, Germany), and 0.75 µl of 10 µM forward and reverse primers, respectively.

The PCR products were combined with an appropriate volume of 10X loading buffer (40 mM EDTA disodium, 0.05% bromophenol blue, 0.05% xylene cyanol, 70% glycerol, adjusted with H2O) and loaded onto 2% agarose gels containing 0.5 µg/ml ethidium bromide (#E1510, Merck). The gels were run in 1X TBE buffer (90 mM Tris, 90 mM H3BO3, 2 mM EDTA disodium, in H2O) at 100 V. To estimate the sizes of the digested fragments, a 50 bp DNA ladder (#SM0372, Thermo Fisher Scientific) was used. The DNA bands were visualized using a UV transilluminator in a light-protected cabinet, and the ArgusX1 photo software (Biostep, Stollberg, Germany) was employed for analysis.

Afterward, the resulting PCR amplicons were purified using the NucleoSpin™ Gel and PCR Clean-up Kit (#740609, Macherey-Nagel, Düren, Germany). They were then mixed with the sequencing primer (either of the primer pairs used for PCR amplification of the edited region depending on the proximity to the intended cut site as indicated in (**Table 5**) and sent for Sanger sequencing analysis to Macrogen Europe B.V. (Amsterdam, the Netherlands). The web-based CRISP-ID analysis tool (Dehairs et al., 2016) was utilized to identify indel formation by aligning the wild-type sequence with that of the sequenced clones.

Table 5. The primers used for PCR amplification of the edited region.

Primer (P) Name	**Forward primer (5‘-3’)**	**Reverse primer (5‘-3’)**	**Annealing T (°C)**	**PCR fragment size (bp)**
ELAVL1 exon 3 P1	GTTACAACTGGCCCCAAGGA	GGAACCTGTGTTCATTGCAGA	62	607
ELAVL1 exon 3 P2	GCAAAGGTCGGAAAGACACG	ATCCCATTTCCCAAAGGCCAG	65	986
ELAVL1 exon 4 P1	CCTCAGCCTCCTCAAACCAAA	CCAGCACATCAGAGAGGTAGC	60	635
AAVS1 P1	GCTCCATCGTAAGCAAACC	AGTCTTCTTCCTCCAACCC	62	348
Rosa26 P1	GCCCATGAGATACAGAACAAAG	GCCACTCAATGCTCACTAAC	59	537
Rosa26 P2	CCGTTCTGTGAGACAGCC	CTTGCACGAACACGAGCC	60	549
Ifg2bp2 P1	GAGAGGGAAAGAAAAGCGAG	GCAGCAAAGGACCAGAAC	62	579
IGF2BP2 P1	TGTCCTGCTGCATTTCAGAGCC	AAGGAAGCAAAGGAAGCCCCAC	62	323

3.7 RNA isolation, reverse transcription, and quantitative PCR

To extract human RNA from cultured cells, the High Pure RNA Isolation Kit (#11828665001, Roche, Mannheim, Germany) was utilized following the manufacturer's instructions. The concentration of the isolated RNA was determined using NanoDrop™ (Thermo Fisher Scientific), and RNA samples with an A260/A280 ratio higher than 1.8 were selected for further experiments. Equal amounts of RNA were then transcribed using the High-Capacity cDNA Reverse Transcription Kit (Thermo Fisher Scientific #4368813) in the presence of an RNAase inhibitor (Invitrogen #10777-019), following the manufacturer's instructions. Gene expression analysis was conducted using 5X HotFirePol EvaGreen qPCR Mix (#08-25-00020, Solis BioDyne, Tartu, Estonia) on a CFX96 touch® Real-Time PCR detection system with the CFX Manager 2.1 software (Bio-Rad Laboratories, Munich, Germany). The efficiency of reverse transcription quantitative PCR (RT-qPCR) was checked for each run to ensure it fell within the accepted range of 90-105%. Generally, Ct values were normalized to the housekeeping gene *RNA18SN5*. Primers for all the listed genes in **Table 6** were obtained from Eurofins Genomics (Ebersberg, Germany).

Table 6. The conditions used in the setup of qPCR reaction of the listed genes.

Gene	**Forward primer (5'-3')**	**Reverse primer (5'-3')**	**µl primer [10 µM] /reaction**	**Annealing T (°C)**
RNA18SN5	GAATGGGGTTCAACGGGTTA	GAATGGGGTTCAACGGGTTA	0.5	61
p62	GTTCCCGCATCATCACTCTTAT	GAATCTCGCCAGCTGTTTGA	0.5	61
IGF1R	TTCGGAGTATTGTTTCCTTCGCC	CCTGGCCCGCAGATTTCTC	0.5	60
IGF2	AAGTACAACATCTGGCCCGC	GGATTCCCATTGGTGTCTGGA	0.5	56
IMP1	GCCTCCATCAAGATTGCACCAC	AGCTTCACTTCCTCCTTGGGAC	0.5	62
IMP2	CAATCTGATCCCAGGGTTG	GCCCTGCTGGTGGAGATAG	0.4	60
IMP3	TCCCACCCA ATT TGT TGGAGC C	GCAGCCCCCGCATTTTCTTTAC	0.4	62
HMGA2	CCTAGGAAATGGCCACAACA	CTTCGGCAGACTCTTGTGAGG	0.5	59
HMGA1	CTAATTGGGACTCCGAGCCG	GTAGCAAATGCGGATGCCTT	0.5	59
PPAR-γ	GACAGGAAAGACAACAGACAAATC	GGGGTGATGTGTTTGAACTTG	0.5	59

TSC1	AGAGCCACATGACAA GCACC	GGATAAACGAGTGGC GGCTT	0.5	60
MYC	AGCCACAGCATACAT CCTGTCC	CTCGTCGTTTCCGCAA CAAGTC	0.5	59
DANCR	GCTCCAGGAGTTCGTC TCTTAC	TGCGCTAAGAACTGA GGCAG	0.5	60

A total volume of 20 µl per PCR reaction was used, and all samples were performed in biological triplicates and technical triplicates within the PCR runs using the following program:

denaturation	95°C 15 min	
denaturation	95°C 0.15 min	
annealing °C*	0.20 min	35 cycles
elongation	72°C 0.20 min	
final elongation	72°C 10 min	
Plate read		
Melting curve	65°C	0.5°C / 5s
	95°C	

* Annealing temperatures for each gene were adjusted based on **Table 6**.

3.8 Next-generation sequencing

The cell transfection was performed as described in 3.5.1, and 24 h post-transfection, the cells were washed with 1X PBS, detached with trypsin (#T3924, Merck), and resuspended in culture media to obtain a cell suspension. Approximate 30-40 GFP-positive cells as mentioned in section 3.5.1 were picked manually with a microneedle under a microscope and added to a PCR tube containing 2 µl of lysis buffer (Phire Tissue Direct PCR Kit, ThermoFisher Scientific #F170). Heat inactivation of Proteinase K in the lysis buffer was performed at 96°C for 3 min. The ready-to-use genomic DNA probes were then maintained at -20°C until further use.

The PCR1 was performed using gene-specific primers *IGF2BP2*-P1 (**Table 5**) to amplify a specific target region where the gRNA1 and gRNA2 were designed for the editing of the *IGF2BP2*. For PCR1, the Phire Tissue Direct PCR Master Mix (F170S, Thermo Scientific) was used as per the manufacturer's protocol. The amplified product was purified by agarose gel electrophoresis (as described in 3.6) to get the desired size amplicon of 323 bp and to remove PCR residues, such as nucleotides, salt, and primers which could interfere with the downstream processing. The purified product is eluted in molecular biology water and used as a template in the PCR2 and thereafter stored at -20°C until use.

PCR1 protocol

denaturation	95°C 0.30 min	
denaturation	95°C 0.15 min	
annealing °C	68°C 0.15 min	37 cycles
elongation	72°C 0.30 min	
final elongation	72°C 3 min	
cooling	12°C, ∞	

PCR2 protocol

denaturation	95°C 0.30 min	
denaturation	95°C 0.15 min	
annealing °C	50°C 0.15 min	15 cycles
elongation	72°C 0.30 min	
denaturation	95°C 0.15 min	
annealing °C	68°C 0.15 min	15 cycles
elongation	72°C 0.30 min	
final elongation	72°C 3 min	
cooling	12°C, ∞	

In PCR2, the primers bound to NGS-sequencing adapters (**Table 7**) were used. For the PCR2, the KAPA2G Fast Hot Start Genotyping Mix (KK5620, Sigma Aldrich) was used as per the manufacturer's instructions, using the PCR1 product as a template. The primers used in this step were ordered from Eurofins genomics. The PCR2 product was then subjected to agarose gel purification, eluted in water, and stored at -20°C until further use. Subsequent sequencing was performed on an Illumina NextSeq platform using single-end sequencing. The sequencing results were analyzed using the CRISPResso2 software package (Clement et al., 2019).

Table 7. NGS adapter primers.

Primer	**Sequence (5'-3')**
gRNA1 Fwd	TCTTTCCCTACACGACGCTCTTCCGATCTCCTTCAAGATTTCCTACATC
gRNA1 Rev	GTGACTGGAGTTCAGACGTGTGCTCTTCCGATCTGCCCTCCTTTCCGATGATG
gRNA2 Fwd	TCTTTCCCTACACGACGCTCTTCCGATCTGCCCTCCTTTCCGATGATG
gRNA2 Rev	GTGACTGGAGTTCAGACGTGTGCTCTTCCGATCTCCTTCAAGATTTCCTACATC

3.9 Western blot

The samples were prepared in either SB lysis buffer or RIPA buffer, both supplemented with a protease inhibitor cocktail (cOmplete® Mini, # 04693124001, Roche). The SB lysis buffer consisted of 50 mM Tris-HCl, 1% SDS, 10% glycerol, 5% β-mercaptoethanol, 0.004% bromophenol blue, and water. The RIPA buffer contained 50 mM Tris-HCl, 1% triton X-100, 0.1% SDS, 0.5% sodium deoxycholate, 150 mM NaCl, and water. After preparation, the samples were sonicated for 5 s and stored at -80°C until further analysis. The protein concentration in the RIPA lysates was determined using the Pierce™ BCA Protein Assay Kit (#23225, Thermo Fisher Scientific) as per the manufacturer's instructions. SDS-polyacrylamide gel electrophoresis (SDS-PAGE) was carried out using polyacrylamide gels (4% stacking gel and 12% resolving gel) and the Mini PROTEAN system from Bio-Rad Laboratories. The samples were thawed on ice and denatured at 95°C for 5 min before loading onto the gel. For samples prepared in RIPA buffer, a loading buffer (Roti®-Load 1 buffer #K929, Carl-Roth) was added before denaturation. To estimate the size of proteins, a prestained protein ladder (PageRuler™, #26616, Thermo Fisher Scientific) was run alongside the samples. The samples were transferred onto an Immobilon®-FL polyvinylidene fluoride (PVDF) membrane using a Mini TransBlot® cell from Bio-Rad. The gel sandwich preparation materials were equilibrated in blotting (transfer) buffer containing 25 mM Tris, 192 mM glycine, 20% methanol, and 0.05% SDS in a final volume of 1 L distilled water. The PVDF (#IPFL00010, Merck, Darmstadt, Germany) membrane was activated with methanol for 30 s before blotting. The transfer was performed in a cold transfer buffer at 80 mA overnight. The membrane was then blocked with Rockland blocking buffer (RBB) (#MB-070, Rockland Immunochemicals, Limerick, PA, USA) for 2 h to prevent the non-specific binding of antibodies. After blocking, the membrane was washed once with 1X PBST buffer (0.1% Tween-20 in 1X PBS) and thrice with 1X PBS buffer. Next, the membrane was incubated with the primary antibody overnight at 4 °C. Following another round of washing, the membrane was incubated with the appropriate IRDye-conjugated secondary antibody at RT for 2 h. All washing steps and incubation were performed on a shaker. After the final wash, the signal was detected using an Odyssey® Near-Infrared Imaging System and software from LI-COR Biosciences. The list of antibodies employed in this work is listed in **Table 8**.

Table 8. List of antibodies used in western blotting.

Antibody	**Dilution**	**Cat-number**	**Supplier**
HuR/ELAVL1 Antibody (3A2)	1:1000 in 5% Milk powder-PBST	sc-5261	Santa Cruz Biotechnology
Anti-human IMP2/p62, rabbit IgG	1:1000 in RBB	Lu et al., 2001	In house
Mouse anti-α-tubulin [DM1A] mAb	1:1000 in RBB	T 9026	Sigma-Aldrich
IRDye® 680RD goat anti rabbit IgG	1:10,000 in RBB	926-68071	LI-COR Biosciences, Lincoln, NE, USA
IRDye® 800CW goat anti mouse IgG	1:10,000 in RBB	926-32210	LI-COR Biosciences, Lincoln, NE, USA

3.10 NFκB reporter cells

HEK-Blue™ hTLR4, HEK-Blue™ Null2, THP1-Xblue™, and RAW-Blue™ cells were used for determining NFκB activity as they express a SEAP gene inducible by NFκB transcription factors. 2 ml tumor cell suspension was seeded per well in a 6-well plate with appropriate cell number to reach 90% confluency the next day. On the following day, the tumor cells were treated with either 50 μM violacein, oxaliplatin, or solvent control. After 4 h, the treatment medium was removed, and fresh media were added to the wells. After an additional 20 h, the supernatants were collected and centrifuged to remove dead cells. These conditioned media from dead tumor cells (dTCM) were then added to the reporter cells that were seeded a day prior, following the manufacturer's protocol. After 24 h, the SEAP activity in the reporter cell supernatants was determined using the QUANTI-Blue™ solution according to the supplier's instructions. A positive control using lipopolysaccharide (LPS-EK Ultrapure) was included in all reporter cell assays. The SEAP levels were measured at 600 nm using a microplate reader (GloMax™) and normalized to cell confluency determined by IncuCyte® S3 analysis.

3.11 Statistics

Data analysis and statistics of experimental data were performed using the OriginPro® 2020 software (OriginLabs, Northampton, MA, USA). All data are displayed as mean values ± SEM of at least 3 independent experiments, if not stated otherwise. Normality was tested with the Shapiro–Wilk algorithm. Grubb's test was performed to identify possible outliers. Depending on normality, a one-way analysis of variance (ANOVA) followed by Tukey's or Bonferroni's analysis or Kruskal–Wallis–ANOVA followed by the Mann–Whitney test was performed. A two-sample *t*-test was used to calculate statistical differences between the two groups. Differences were considered statistically significant with $p \leq 0.05$.

Results and discussion

4. Part I: Characterization of violacein as an anticancer drug

4.1 Violacein

4.1.1 Introduction

Originally isolated from *Chromobacterium violaceum* (*C. violaceum*), violacein (vio) is a distinct blue-violet compound classified as a pyrrolidone and a bisindole. It forms through the condensation of two modified tryptophan molecules (**Figure 6**) (Durán et al., 2016). Prior research has emphasized violacein's anticancer properties, including the induction of programmed cell death through apoptosis (Alshatwi et al., 2016; Ferreira et al., 2004), attenuation of stem-like traits in tumor cells (Kim et al., 2021), and inhibition of tumor cell migration (Mehta et al., 2015).

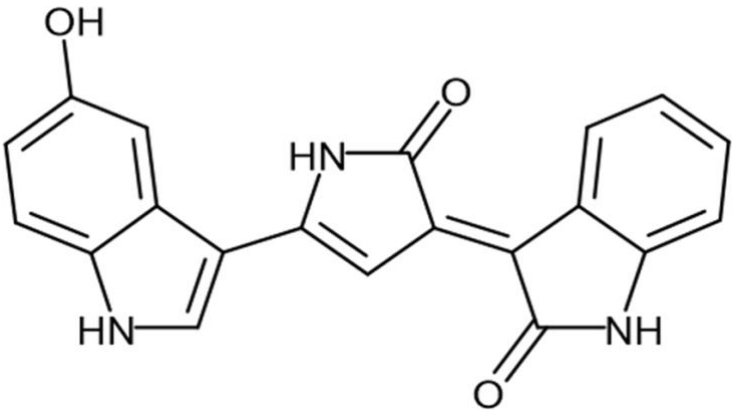

Figure 6. Chemical structure of violacein (Venegas et al., 2019).

In normal cellular contexts, programmed cell death, often executed through apoptosis, efficiently eliminates cells without triggering local or systemic inflammation, thus preventing undesired immune responses (Kroemer et al., 2013). In contrast, immunogenic cell death (ICD), a distinct form of cell demise, stimulates an immune response by releasing specific molecules known as damage-associated molecular patterns (DAMPs), particularly from cancer cells. This phenomenon acts as a protective mechanism, activating the immune system to target and eliminate tumor cells (Zhou et al., 2019).

Key DAMPs include nuclear high mobility group box 1 (HMGB1), calreticulin (CRT), heat shock proteins 70/90 (HSP 70/90), and adenosine triphosphate (ATP). Dendritic cells (DCs) express receptors and attract ligands on their surface that help in recognizing DAMPs present in cancer cells. This leads to the transition of DCs from an immature to a mature phenotype. An ‘eat me’ signal is sent by CRT binding to ERp57 (CRT-ERp57 complex), which promotes the phagocytosis of the cell by the DCs. A ‘find me’ signal is initiated when extracellularly secreted ATP and activates P2X7 receptors on DCs. The binding of HMGB1 to Toll-like receptor 4 (TLR4) and the expression of HSP 70/90 promote the engulfment of antigenic

components by DCs by enhancing the processing of phagocytic cargo in DCs. This results in the stimulation of specific T-cell responses and the killing of more tumor cells (Zhou et al., 2019).

The ICD inducers such as chemotherapeutics, nanoparticles, nano pulse, and near-infrared light can induce ICD by different pathways (**Figure 7**). The classical ICD is triggered by endoplasmic reticulum (ER) stress dependent, upon the induction of the expression of DAMPs. Another pathway involves the stimulation of NFκB activity by mitochondrial outer membrane permeabilization (MOMP). This subsequently leads to caspase-independent cell death (CICD) induction, also considered to be ICD (Zhou et al., 2019).

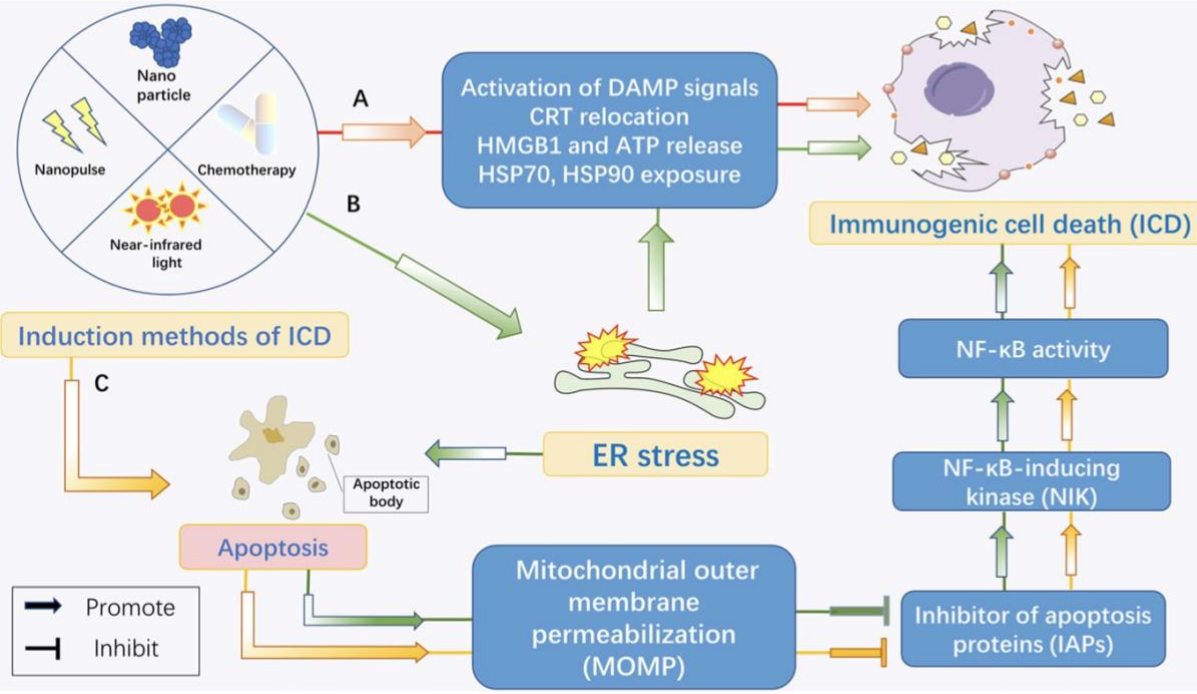

Figure 7. Pathways of ICD induction (Zhou et al., 2019).

The study explores the cytotoxic efficacy of violacein against human pancreatic, liver, and colon cancer cells, examining its viability as an anticancer agent. Moreover, the effect of violacein on proliferation was assessed in the above-mentioned tumor entities. Additionally, this chapter delves into evaluating violacein's potential to induce immunogenic cell death through NFκB activation by utilizing reporter cells.

4.1.2 Results

The results of this section have been published in:

Charlotte Dahlem, **Shilpee Chanda**, Jan Hemmer, Hanna Schymik, Michael Kohlstedt, Christoph Wittmann, Alexandra K. Kiemer. Characterization of Anti-Cancer Activities of Violacein: Actions on Tumor Cells and the Tumor Microenvironment. Frontiers in Oncology. 2022 May 11; 12:872223.

The cytotoxic effects of violacein were assessed using an MTT assay at 48 h post-treatment. The IC_{50} concentrations were in the low micromolar range for HCT116 (8.22 µM), Huh7 (1.88 µM), and PANC-1 (1.44 µM) cells, derived from human colon, liver, and pancreatic cancer, respectively.

The impact of violacein on 2D cell proliferation of HCT116, Huh7, and PANC-1 cells was examined, revealing a dose-dependent inhibition within the tested concentration range of 0.1-10 µM for each cell line (**Figure 8**).

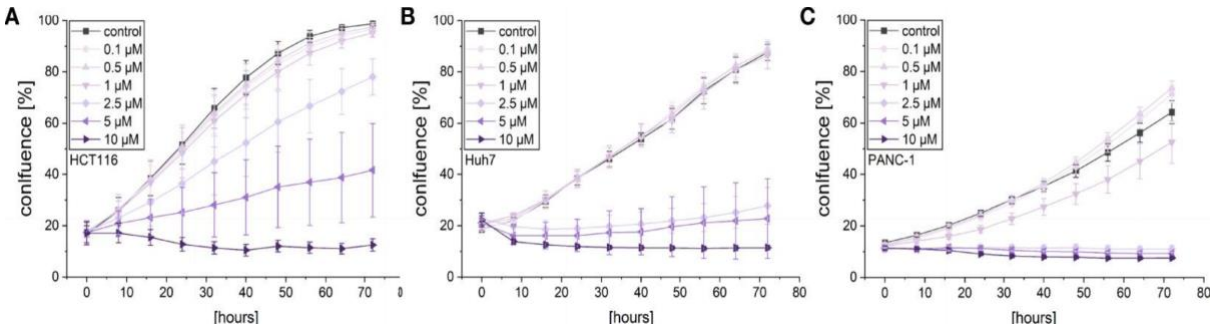

Figure 8. Effect of violacein treatment on the 2D proliferation of (A) HCT116, (B) Huh7, and (C) PANC-1 cells (Dahlem, Chanda, et al., 2022).

To explore violacein's potential in inducing immunogenic cell death, NFκB reporter cells were utilized. These cells were exposed to dead tumor-conditioned media (dTCM) from cancer cell lines (HCT116, Huh7, and PANC-1) treated with either violacein (dTCM-vio) or oxaliplatin (dTCM-oxa). Oxaliplatin served as a positive control for ICD induction. Additionally, the TLR4 agonist lipopolysaccharide (LPS) was used as a macrophage activation positive control.

Exposure of RAW-Blue™ cells to dTCM resulted in significant inflammatory activation (**Figures 9A–C**). However, only a slight NFκB activation was observed in THP1-Xblue™ cells, except for PANC-1-derived dTCM-Vio, which exhibited a notable activation (**Figure 9D-F**). To investigate whether violacein-induced ICD involves binding of HMGB1 to TLR4, HEK-Blue™ hTLR4 cells were employed to study the TLR4 receptor-mediated macrophage activation. Intriguingly, treatment with dTCM-vio did not activate HEK-Blue™ hTLR4 cells (**Figures 9G–I**), whereas significant activation occurred in HEK-Blue™ Null cells lacking TLR4 (**Figures 9J–L**).

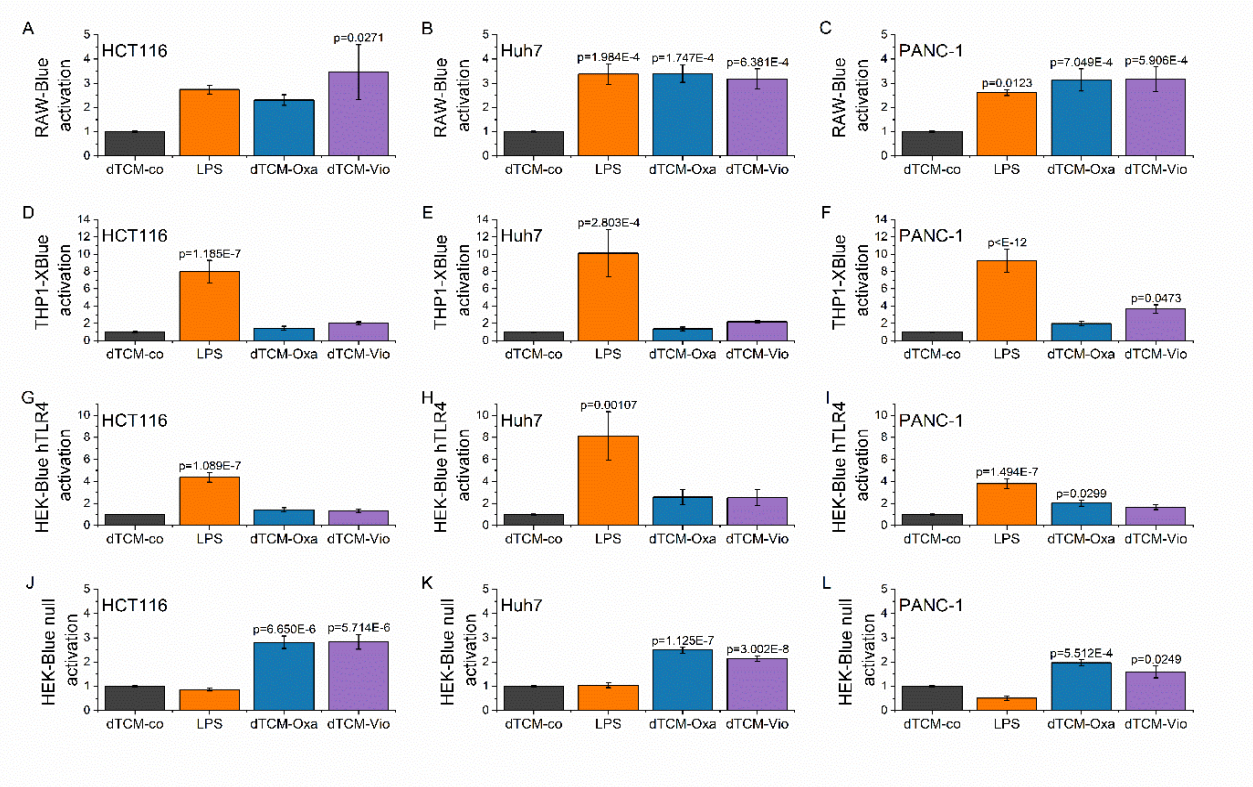

Figure 9. Violacein-killed tumor cell supernatant mediated macrophage activation. Treatment with 50 µM violacein (vio) or oxaliplatin (oxa) upon HCT116, Huh7, and PANC-1 cells for 4 h, followed by media change. 24 h post-treatment, supernatants from untreated (co) and vio or oxa-treated cells were collected. Reporter cells were incubated for 24 h with dead tumor cell-conditioned medium (dTCM-50% v/v); or lipopolysaccharide (LPS-100 ng/ml for RAW-Blue™ and 10 ng/ml for all other reporter cell lines), and the activation was assessed by QUANTI-Blue™ assay (Dahlem, Chanda, et al., 2022).

4.1.3 Discussion

The observed effects of violacein on colon, liver, and pancreatic cancer cells are consistent with previous studies on colon (de Carvalho et al., 2006), melanoma (Gonçalves et al., 2016), head and neck cancer (Masuelli et al., 2016), and breast cancer (Alshatwi et al., 2016). Additionally, violacein's anti-proliferative effects have been noted in other tumor types (Neroni et al., 2022; Kim et al., 2021).

The cytotoxic effects of violacein were also studied in several other tumor entities, namely SK-MEL5, SW620, A549, HeLa, MCF-7, CC-SW-1, and HepG2 with the IC_{50} concentrations also noted to be in the low micromolar range (Dahlem, Chanda, et al., 2022). Furthermore, the cytotoxic effect of violacein was observed in 3D spheroid models of HCT116 cells, when tested up to 40 µM, and an abolished growth of the spheroid as well as the detachment of the cells present on the outer layer was noted (Dahlem, Chanda, et al., 2022). To investigate the effect of violacein in normal cells, Huh7 cells were cultivated long-term in human serum, and the cells showed a transition towards a normal hepatocyte-like phenotype, and violacein did not produce cytotoxic effects (Dahlem, Chanda, et al., 2022). The effect of violacein treatment on doxorubicin-resistant and wild-type Huh7 cells was studied and showed that the treatment killed both cell types.

Violacein was also studied for its effect on other cancer hallmarks such as migration. However, violacein did not affect cell migration in HCT116 cells, whereas inhibition was observed in Huh7 and PANC-1 cells (Dahlem, Chanda, et al., 2022).

To assess violacein's potential for inducing immunogenic cell death, NFκB reporter cells were employed. Oxaliplatin, a known inducer of ICD in colon cancer cells, served as a positive control (Tesniere et al., 2009). TLR4-agonist HMGB1 is known as a marker in immunogenic cell death induction. To investigate the ability of violacein to explicitly activate TLR4, we employed reporter cell lines RAW-Blue™, THP1-Xblue™, and HEK-Blue™ hTLR4 cells, all of which express TLR4. However, in our applied assay conditions, the supernatant from violacein-treated cells showed the potential to activate RAW-Blue™ cells and to a lesser extent THP1-Xblue™ cells. Moreover, we observed an activation of HEK-Blue™ Null cells, which lack TLR4, and rather express TLR3, TLR5, and nucleotide-binding oligomerization domain (NOD) proteins-1 (NOD1). In addition, HEK-Blue™ Null cells lack TLR8, further hinting that the effects of violacein seen in RAW-Blue™ and THP1-Xblue™ reporter cells are not only due to the previously known TLR8 receptor-mediated macrophage activation (Venegas et al., 2019).

5. Part II: Validation of RNA binding proteins as potential anticancer targets

5.1 Validation of HuR as a potential anticancer target and characterization of potential natural HuR inhibitors

5.1.1 Introduction

The role of HuR in cancer was previously described in section *1.4.1*. This chapter aimed to validate HuR as an anticancer target using gene editing techniques. The correlation of HuR overexpression with survival rate among breast and liver cancer patients was previously investigated using Kaplan-Meier analysis. Results showed that the survival rate is significantly reduced with high HuR expression as per data provided in the Human Protein Atlas; available from www.proteinatlas.org (Uhlen et al., 2017) (**Figure 10**).

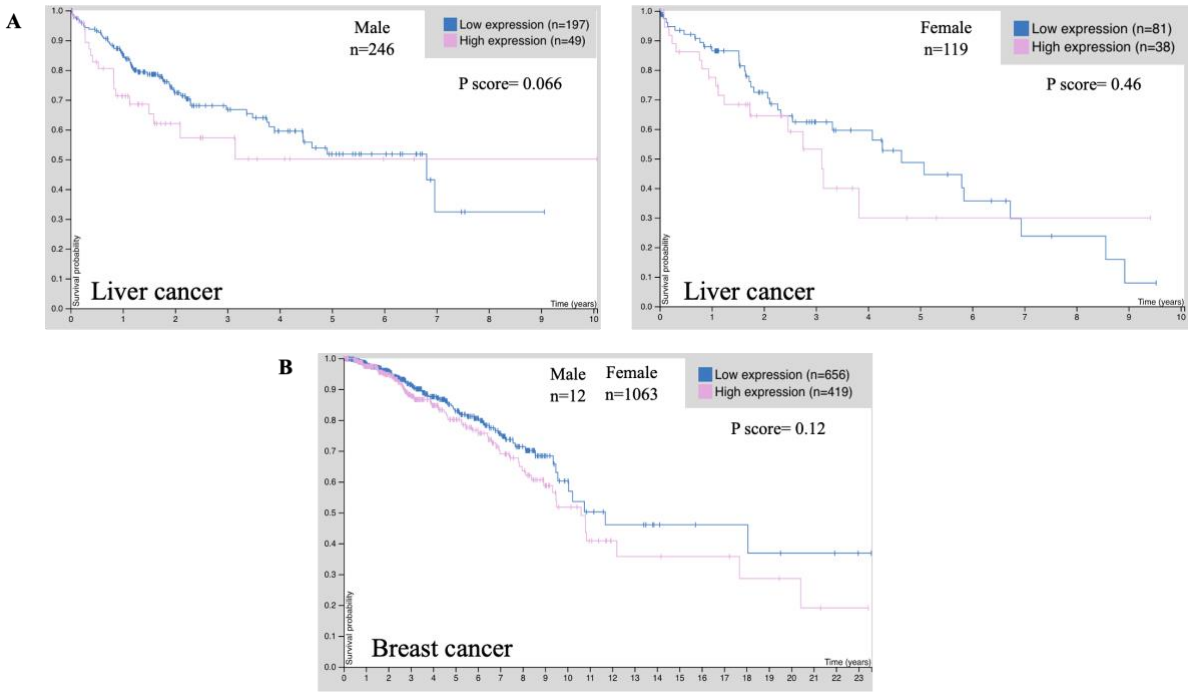

Figure 10. The association of *ELAVL1* expression with survival rate in human (A) liver (left panel- male; right panel- female) and (B) breast cancer (male and female combined). Based on the fragments per kilobase per million mapped read (FPKM) values of HuR expression, patients were classified into high (indicated by pink line) and low (indicated by blue line) expression groups. Association between HuR expression and patient survival rate was examined using Kaplan-Meier analysis. P score is the log-rank P value for Kaplan-Meier plot showing results from analysis of correlation between mRNA expression level and patient survival. 'n' denotes the number of patients. The figure was adapted from the Human Protein Atlas; available from www.proteinatlas.org (Uhlen et al., 2017).

We investigated the role of HuR in these cancer types by employing the ribonucleoprotein complex-based CRISPR/Cas9 approach to generate HuR knockouts in MDAMB-231 (human breast cancer) and HepG2 (human hepatocellular carcinoma) cell lines. These cell lines were selected for two reasons. Firstly, they exhibit high RNA expression of HuR, as supported by

the Human Protein Atlas; available from www.proteinatlas.org (Uhlen et al., 2017) (**Figure 11**).

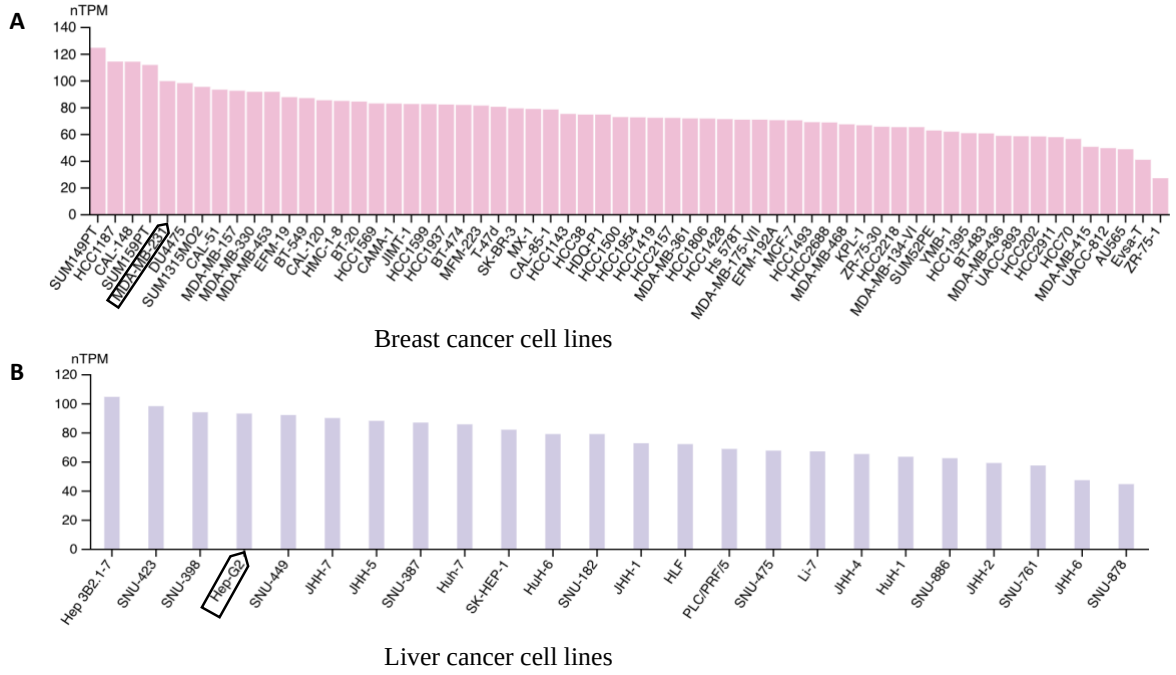

Figure 11. RNA expression of ELAVL1, in human (A) breast and (B) liver cancer cell lines. RNA expression data as normalized transcript per million (nTPM) values of cancer cell lines. The figure was adapted from the Human Protein Atlas; available from www.proteinatlas.org (Uhlen et al., 2017).

Secondly, the cell lines have low ploidy, increasing the probability of the CRISPR/Cas9-based approach in achieving a biallelic knockout. The success of the CRISPR/Cas9 knockout procedure was validated at the gene level through Sanger sequencing analysis and at the protein level through Western blotting. The impact of monoallelic HuR knockout in MDAMB-231 cells was studied on 2D cell proliferation.

Previous docking results from our collaborators, Prof. Simona Collina at the University of Pavia (Italy), and Prof. Anna K. Hirsch at the Helmholtz Institute of Pharmaceutical Sciences Saarland (HIPS, Germany), demonstrated that a series of natural compounds tested interact with HuR in the same region as the target RNAs (Nasti et al., 2017). Building upon these preliminary data, they conducted a more detailed investigation into the ligand-HuR interaction, focusing on a small number of natural compounds such as those belonging to the flavonoid and coumarin families, utilizing STD-NMR experiments (Vasile et al., 2018). Out of the 13 compounds studied, our collaborators shared with us two potential HuR inhibitors: epicatechin (EC) (**Figure 12A**) and novobiocin (NovNa) (**Figure 12B**).

To investigate whether epicatechin's anticancer mechanisms involve interactions with HuR, Vasile et al., 2018 analyzed the binding affinity between epicatechin and HuR. The STD data, presented in **Figure 12A**, pinpoint the primary interaction site within the epicatechin and HuR interface: specifically, the protons located at positions 6 and 8 within the chroman-3-ol nucleus of epicatechin. Novobiocin also displayed substantial binding affinity toward multiple sites

within HuR (**Figure 12B**). This discovery provided an initial reference point for subsequent *in vitro* studies. In this work, epicatechin and novobiocin were assessed for their effect on the 2D cell proliferation *in vitro* using various human cancer cell lines, including colon (HCT116, SW480), hepatocellular (Huh7), and breast cancer (MCF7, T47D, MDAMB-231) cell lines.

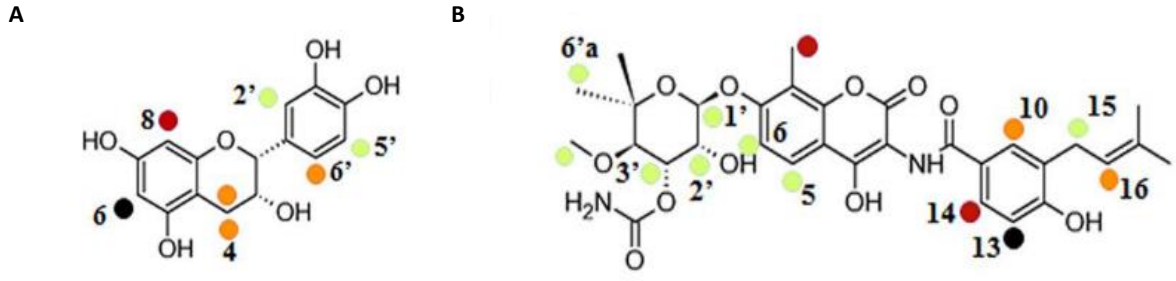

Figure 12. Chemical structure and STD results for (A) epicatechin and (B) novobiocin. Group epitope mapping is highlighted (Vasile, et al., 2018). Relative STD percentages are shown by color-coded dots: black: the most intense signal (100% relative STD), dark red: over 80%, orange 40%, and lime green: under 40% relative to the most intense STD signal.

In the realm of cancer therapy, numerous naturally derived dietary supplements have gained recognition for their potential roles as preventive and therapeutic agents. A prominent example of these supplements is flavonoids, which consist of multiple phenolic units. Specifically, those belonging to the catechin family have been extensively studied and demonstrated to possess anticancer properties (Yang & Wang, 2016). Among these bioactive molecules, epicatechin has garnered notable attention due to its well-established anticancer effects (Kim et al., 2012; Papiez et al., 2010; Shay et al., 2015).

Novobiocin, a prominent member of the coumermycin antimicrobial family, operates by binding to the ATP-binding pocket of DNA gyrase, effectively impeding ATP hydrolysis and serving as a well-known antimicrobial agent (Laurin et al., 1999). Its interaction within the DNA gyrase's B subunit and ADP co-crystal structures, assuming a bent conformation, mirrors the binding pattern observed between HSP 90 and ADP (Schwartz et al., 1993). Drawing from this insight, novobiocin has demonstrated cytotoxic effects attributed to its inhibition of HSP 90 via ADP binding. Notably, novobiocin's potential in antitumor activities was initially recognized in human breast cancer cells (Donnelly et al., 2008).

5.1.2 Results

Validation of HuR knockout on the gene level

The sgRNAs, gRNA3, and gRNA4 (**Table 1),** were delivered as ribonucleoprotein (RNP) complexes. While gRNA4 failed to produce HuR knockout clones in MDAMB-231 cells, gRNA3 successfully generated two monoallelic HuR knockout clones, designated as mKO#1 and mKO#2, with a CG deletion at the expected cut site, as confirmed by Sanger sequencing results (**Figure 13**).

After achieving successful editing with gRNA3 in MDAMB-231 cells, the same gRNA was used to generate HuR knockouts in HepG2 cells. Sanger sequencing revealed a monoallelic CG deletion in two HepG2 HuR knockout clones, namely mKO#1 and mKO#2 (similar to the editing observed in MDAMB-231 HuR knockout clones) (**Figure 13**).

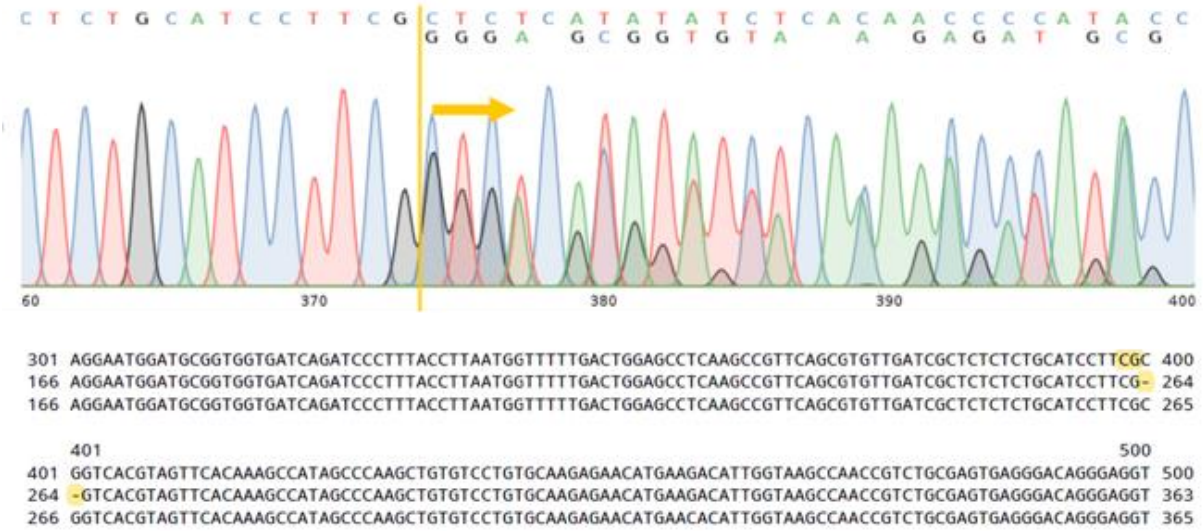

Figure 13. Monoallelic CG deletion in MDAMB-231 and HepG2 HuR knockout clones resulting from RNP delivery-based CRISPR/Cas9 approach using gRNA3 detected by Sanger sequencing**.** The first line of the alignment represents the wild-type sequence. The two lines below the reference indicate different sequences of each allele (monoallelic editing). Yellow arrows highlight the start site of at least two different sequences/alleles in cell clones. Color code visualizes matches in aligned sequences. A: adenine (green), C: cytosine (blue), G: guanine (black), and T: thymine (red). -: missing DNA base.

Validation of HuR knockout on protein level

Western blots confirmed reduced HuR expression in the monoallelic knockouts. The MDAMB-231 HuR knockout clone mKO#1 expressed 17.56% of the protein, while clone mKO#2 expressed 92.06% of the protein, both in comparison to the wild-type cells (**Figure 14A, C).** Based on this, clone mKO#1 was selected for another round of CRISPR/Cas9-knockout procedure using gRNA3; however, this did not result in biallelic editing.

In the case of HepG2 HuR knockout clones, mKO#1 and mKO#2, both showed close to 65% HuR expression compared to wild-type cells (**Figure 14B, C).** Due to the significant amount of HuR still expressed in the HepG2 clones, no further studies were undertaken using these clones.

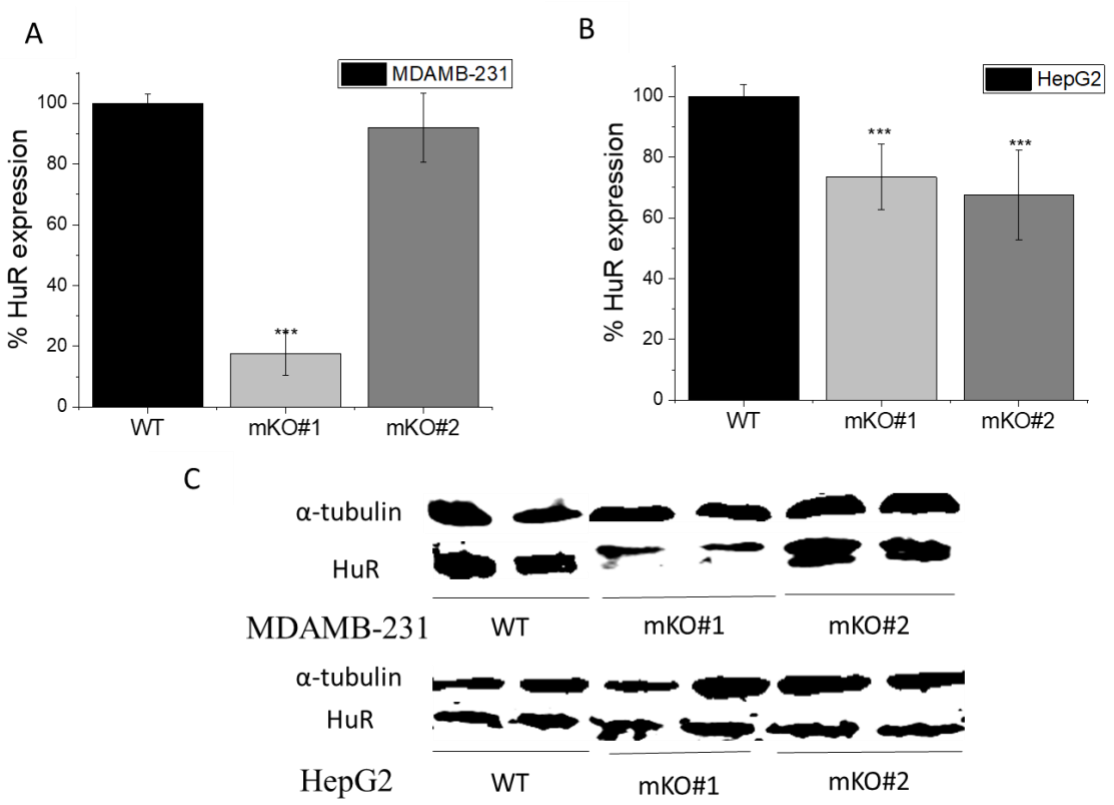

Figure 14. Western blot analyses of MDAMB-231 and HepG2 knockout clones resulting from RNP delivery-based CRISPR/Cas9 approach using gRNA3. (A) Quantification of protein expression of MDAMB-231 monoallelic HuR knockout clones. (B) Quantification of protein expression of HepG2 monoallelic HuR knockout clones. (C) Representative blots of MDAMB-231 and HepG2 HuR monoallelic knockout clones. Quantification of the protein levels of HuR (36 kDa) was performed using alpha-tubulin (55 kDa) as an internal control/housekeeping protein. Bars represent mean ± SEM. n=2 (duplicates). *$p < 0.05$, **$p < 0.01$, and ***$p < 0.001$ when compared to values of wild-type (WT).

In vitro HuR target validation

To study the impact of HuR on cancer cell proliferation, a 2D proliferation assay was conducted using the monoallelic HuR knockout MDAMB-231 clones. However, no significant difference in the rate of proliferation was observed between the knockout clones and the wild-type/control (Co) cells (**Figure 15**). As the biallelic knockout of HuR was not achieved, further characterization of the knockout clones was not pursued.

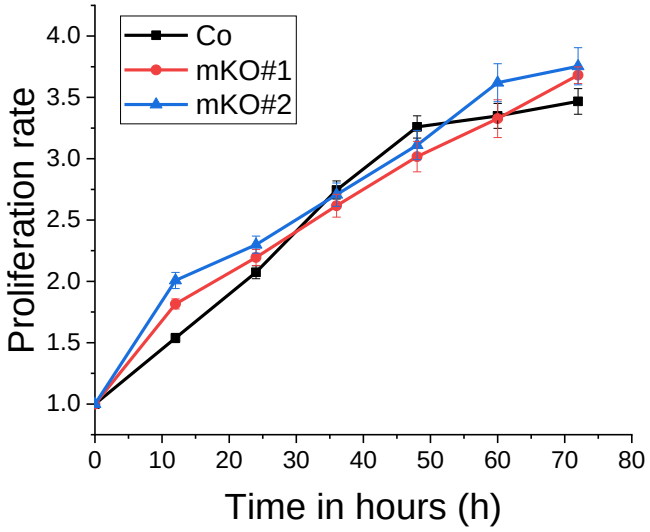

Figure 15. Effect of HuR knockout on the 2D cell proliferation. MDAMB-231 cells were assessed for the effect of HuR knockout on the 2D cell proliferation using the IncuCyte® S3 live cell imaging system. The HuR MDAMB-231 knockout clones mKO#1 and mKO#2 were monoallelic. Data were normalized to time point 0 h and represent means ± SEM, n=3, quadruplicates. Values were compared to the wild-type/control (Co) cells. The proliferation rate was determined based on the cell confluence.

Testing of potential HuR inhibitors

The two compounds, epicatechin (EC) (**Figure 16**) and novobiocin (NovNa) (**Figure 17**) (Vasile et al., 2018) did not show any significant anti-proliferative effect on the tested tumor cell lines at low to moderate concentrations. Only very high concentrations of 300 µM showed a slight reduction in proliferation; an effect that can be explained most likely by unspecific activities. Hence, no further work was undertaken using these compounds. There is a need to search for other potential HuR inhibitors that are potent and demonstrate better anti-proliferative activity.

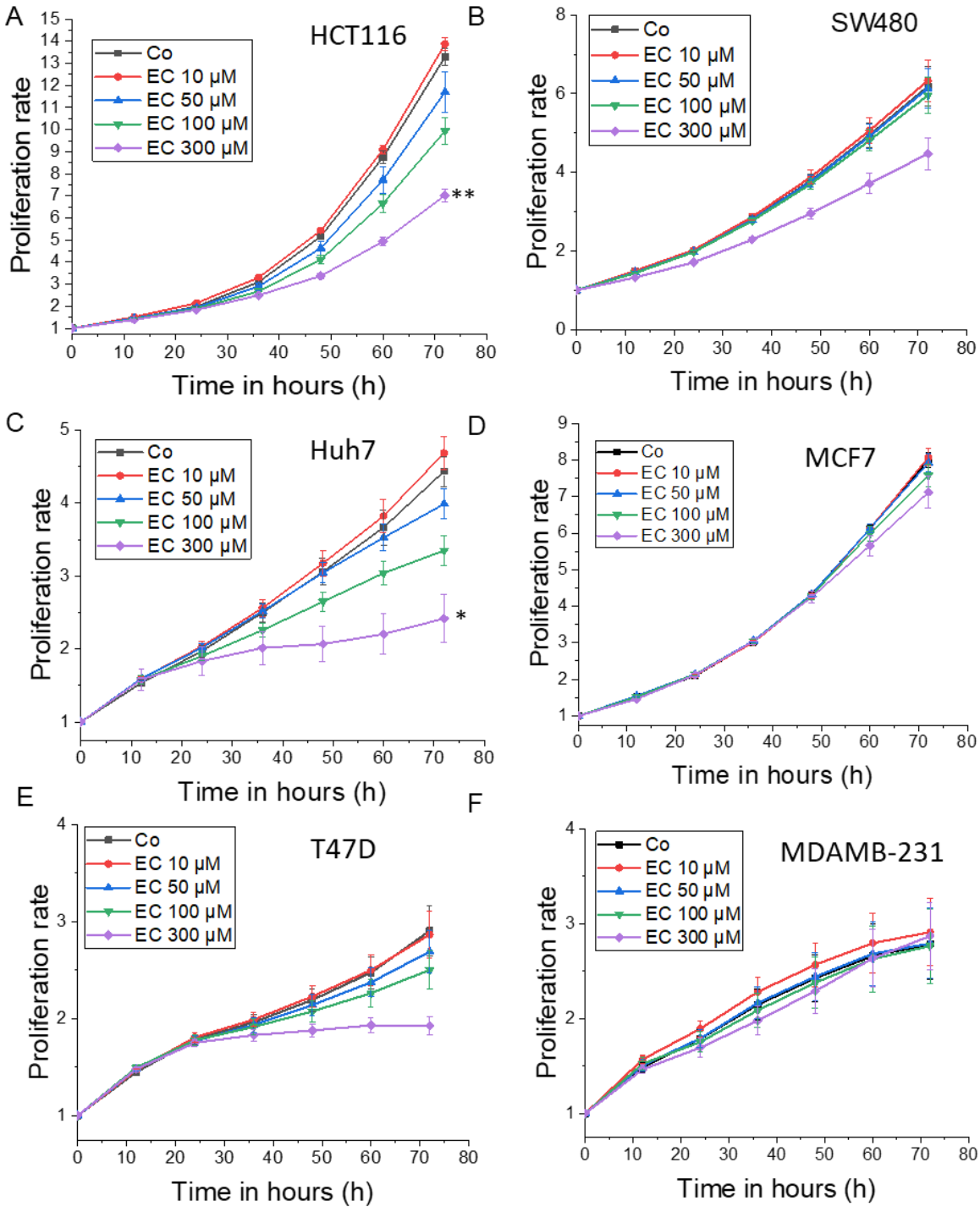

Figure 16. Effect of epicatechin (EC) on the 2D cell proliferation over 3 days tested at various concentrations up to 300 µM upon (A) HCT116 (B) SW480 (C) Huh7 (D) MCF7 (E) T47D (F) MDAMB-231 cells using the live cell imaging system, IncuCyte® S3. Data were normalized to time point 0 h and represented as mean ± SEM, n=3, quintuplicates. *p < 0.05, **p < 0.01, and ***p < 0.001 compared to values of solvent control (Co). The proliferation rate was determined based on the cell confluence.

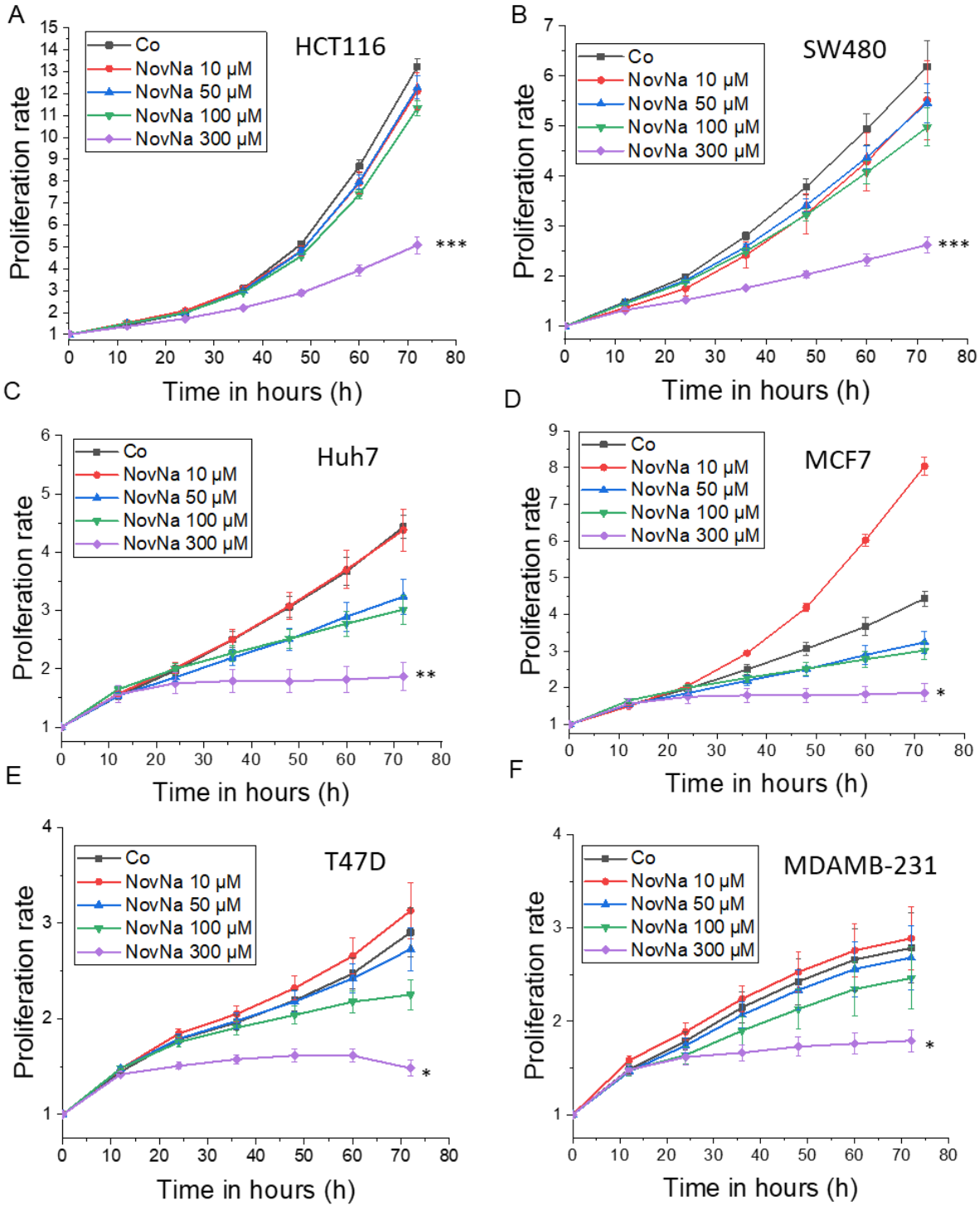

Figure 17. Effect of novobiocin (NovNa) on the 2D cell proliferation over 3 days tested at various concentrations up to 300 µM upon (A) HCT116 (B) SW480 (C) Huh7 (D) MCF7 (E) T47D (F) MDAMB-231 cells using the live cell imaging system, IncuCyte® S3. Data were normalized to time point 0 h and represented as mean ± SEM, n=3, quintuplicates. *p < 0.05, **p < 0.01, and ***p < 0.001 compared to values of solvent control (Co). The proliferation rate was determined based on the cell confluence.

5.1.3. Discussion

The primary aim of targeting exons 3 and 4 of the *ELAVL1* gene was to induce indel mutations at the initiation sites of the HuR protein's RNA recognition motif (RRM). The intention was to introduce frameshift mutations that would disrupt protein formation. While gRNA3 led to monoallelic edits at the target site of exon 3, gRNA4 failed to produce any edits in exon 4.

Genomic instability, including chromosomal abnormalities and aneuploidy, is a recognized hallmark of cancer and must be taken into account (Hanahan, 2022). For this study, MDAMB-231 and HepG2 cell lines were chosen due to the elevated RNA expression of HuR in breast and liver cancer, respectively, as indicated by the Human Protein Atlas database. MDAMB-231 cells were aneuploid, with a modal chromosome count of 64 and a range from 52 to 68, exhibiting near-triploidy. Similarly, HepG2 cells had a modal chromosome count of 55, spanning 50 to 60. The decision to exclude the widely used MCF7 breast cancer cell line was based on its modal chromosome counts, ranging from hypertriploidy to hypo tetraploidy, posing challenges in achieving comprehensive gene edits using the CRISPR/Cas9 system.

The lack of a significant impact of HuR knockout on the 2D proliferation could be attributed to the monoallelic knockout clones still expressing substantial HuR levels. These findings underscore the intricate nature of gene expression regulation and the complexities in achieving complete gene knockout with the CRISPR/Cas9 system.

Epicatechin's demonstrated IC_{50} of 350 µM in breast cancer cells (MDAMB-231 and MCF7) aligns with this study's results, reaffirming its low potency against cancer cells (Pereyra-Vergara et al., 2020). Similarly, Novobiocin's IC_{50} of around 700 µM in breast cancer cell lines is consistent with the data obtained in this thesis (Donnelly et al., 2008). Efforts to enhance the inhibitory effects on cancer cell lines have led to the synthesis of various novobiocin analogs (Burlison et al., 2008; Dlugosz & Janecka, 2017; Hall et al., 2016). Consequently, there is a demand for testing alternative HuR inhibitors or improved structural analogs to achieve potent anticancer effects. These endeavors pave the way for developing more effective therapeutic interventions with enhanced anti-proliferative activity.

5.2 Validation of IMP2 as a potential target for cancer therapy

5.2.1 Introduction

IMP2 has emerged as a crucial participant in carcinogenesis across various cancer types, including hepatocellular carcinoma, colorectal carcinoma, and lung carcinoma (Huang et al., 2018; Kessler et al., 2015; Li et al., 2019). Given IMP2's significant role in cancer, the underlying hypothesis of this work was that disruption of the function of IMP2 can substantially hinder tumor growth, offering a promising avenue for therapeutic intervention. To validate IMP2 as an anticancer target, gene editing techniques and small molecule inhibitors of IMP2 were employed in this study.

Biallelic IMP2 knockouts in HCT116 cells using the CRISPR/Cas9-prime editing approach and monoallelic IMP2 knockouts in SW480, HepG2, and Huh7 cells using RNP delivery-based CRISPR/Cas9, have been previously generated (Dahlem, Abuhaliema, et al., 2022). Building on these achievements, this study aimed to generate biallelic IMP2 knockouts in other human and murine tumor cell lines.

To establish a negative control for the prime editing-based knockout generation, pegRNA constructs were designed to disrupt a safe harbor locus (SHL) in both human (HCT116) and murine (LLC1) tumor cells. While a biallelic AAVS1 knockout HCT116 clone was achieved by prime editing, the technique failed to generate a Rosa26 knockout in LLC1 cells. The biallelic AAVS1 knockout HCT116 clone was characterized based on 2D cell proliferation in comparison with wild-type and biallelic IMP2 knockout HCT116 cells.

Efforts to obtain a biallelic IMP2 knockout in SW480, HepG2, Huh7, A549, and LLC1 cells using prime editing were unsuccessful due to the inability to acquire proliferating single cell-derived clones. Consequently, a plasmid-based CRISPR/Cas9 approach was employed in Huh7 and A549 cell lines, which also did not result in proliferating IMP2 knockout clones. To test the hypothesis that IMP2 is essential for cell proliferation in A549 and Huh7 cells, the editing efficiency of the gRNAs used in the plasmid-based CRISPR/Cas9 approach was verified through next-generation sequencing. The plasmid-based CRISPR/Cas9 approach successfully generated biallelic-edited IMP2 knockouts in LLC1 cells. Validation of IMP2 knockout in the IMP2 knockout LLC1 clones was performed at both the gene and protein levels.

Additionally, this thesis aimed to confirm IMP2 as an anticancer target *in vitro*. The target specificity of IMP2 in the biallelic IMP2 knockout HCT116 cells was studied by performing rescue experiments through overexpression of IMP2/p62 in the previously generated IMP2 knockout HCT116 clones, KO#1 (RNP-delivery based CRISPR/Cas9 generated) and KO#2 (prime editing generated). Furthermore, the impact of IMP2 knockout on the expression of several known IMP2 targets: *IMP1, IMP3, TSC1, PPAR-γ, IGF1R, IGF2, HMGA1, HMGA2, DANCR,* and *MYC* were assessed (Dai et al., 2017; Hu et al., 2019; Wang et al., 2019). Gene expression of *IGF2BP2* and *p62* was also verified in the biallelic IMP2 knockout HCT116 cells.

Small molecule IMP2 inhibitors were previously identified, showing target-dependent effects in wild-type and knockout cells (Dahlem, Abuhaliema, et al., 2022). The impact of three IMP2 inhibitor compounds, namely 4, 6, and 9, were tested on HCT116 and SW480 cells by measuring the expression of IMP2 targets *DANCR, MYC,* and *HMGA1* in both the 2D and 3D cell culture models (Dahlem, Abuhaliema, et al., 2022). The effect of these compounds on gene and protein expression of IMP2 in both HCT116 and SW480 cells was studied (Dahlem, Abuhaliema, et al., 2022).

Furthermore, the effect of IMP2 knockout and IMP2 inhibitor treatment on the hallmarks of cancer was studied in monoallelic IMP2 knockout HepG2, Huh7, SW480 cells, and biallelic IMP2 knockout LLC1 cells. To investigate IMP2-dependent effects of the inhibitors, we studied the effect on wild-type and biallelic IMP2 knockout LLC1 cells in terms of 2D cell proliferation and metabolic activity.

By exploring the potential of IMP2 as a therapeutic target, this chapter contributes to understanding IMP2's role in cancer and provides insights into novel therapeutic strategies for cancer treatment.

5.2.2 Results

Parts of this section are to be/ have been published in:

Shilpee Chanda, Konstantin Lepikhov, Charlotte Dahlem, Hanna S. Schymik, An-Kristin Geber, Konrad Wagner, Sonja M. Kessler, Martin Empting, Alexandra K Kiemer. Characterization of the RNA binding protein IGF2BP2/IMP2 as an anti-cancer drug target: gene editing strategies and small molecule inhibitors. Frontiers in Bioscience Landmark. Manuscript in revision. September 2023.

Charlotte Dahlem, Ali Abuhaliema, Sonja M. Kessler, Tarek Kröhler, Ben G. E. Zoller, **Shilpee Chanda**, Yingwen Wu, Simon Both, Fabian Müller, Konstantin Lepikhov, Susanne H. Kirsch, Stephan Laggai, Rolf Müller, Martin Empting, and Alexandra K. Kiemer. First Small-Molecule Inhibitors Targeting the RNA-Binding Protein IGF2BP2/IMP2 for Cancer Therapy, ACS Chemical Biology, 2022, 17 (2), 361-375.

Negative controls in the prime editing approach

To establish knockout controls using prime editing in the human cell line HCT116 (since biallelic IMP2 knockout was generated previously in HCT116 cells), the safe harbor locus *AAVS1* was targeted. This was achieved by designing two pegRNAs, referred to as pegRNA1 and pegRNA2, as outlined in **Table 2**.

For assessing transfection efficiency, the cells were individually transfected with each of the pegRNAs. 24 h post-transfection, successful transfection, i.e., green fluorescence, was

observed in 20% of the cells. Upon transfection with pegRNA1, out of the initially seeded 40 GFP-positive cells, only 20 managed to undergo growth. However, subsequent sequencing analysis revealed that none of these clones displayed any detectable editing, with their sequences remaining identical to the wild-type.

In contrast, pegRNA2 transfection resulted in 18 out of 40 GFP-positive cells successfully proliferating into single-cell-derived clones. Importantly, a specific clone designated as bKO#1 exhibited biallelic T insertion near the intended editing site. This particular outcome is represented in **Figure 18**.

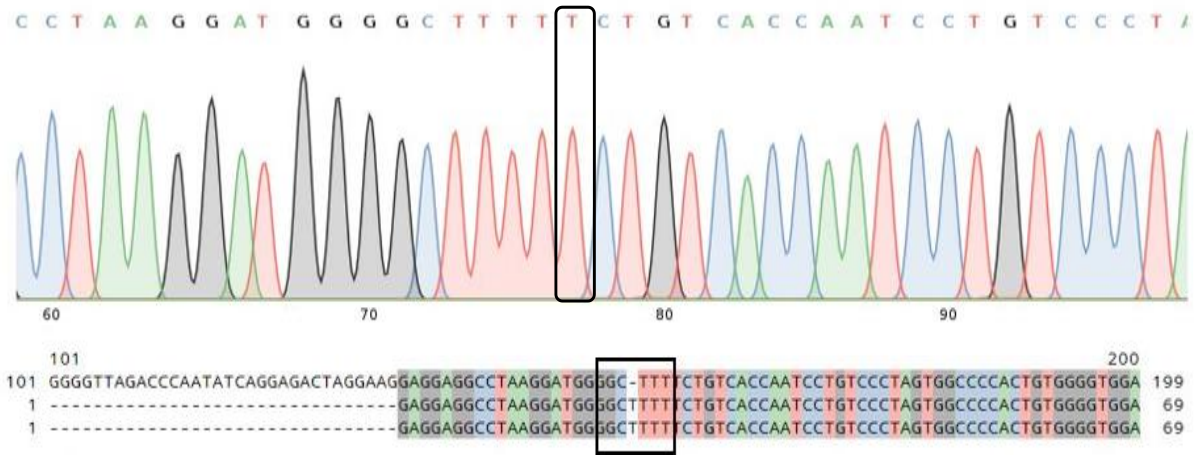

Figure 18. Biallelic T insertion in AAVS1 knockout HCT116 clone bKO#1 using prime editing approach. The first line of the alignment represents the wild-type sequence. Black frames in the sequence alignments demonstrate the section shown in the chromatograms above. Color code visualizes matches in aligned sequences. A: adenine (green), C: cytosine (blue), G: guanine (black), and T: thymine (red). -: missing DNA base.

Validation of AAVS1 knockout in HCT116 cells

The impact of AAVS1 knockout in HCT116 cells on cell proliferation in both the 2D and 3D models was investigated. To ensure a reliable comparison, we examined the effects of the previously generated PE-mediated biallelic IMP2 knockout HCT116 cells (Dahlem, Abuhaliema, et al., 2022). We evaluated the proliferative capacity of the biallelic AAVS1 knockout clone bKO#1 and its metabolic activity in the 2D models, comparing them with wild-type/control cells in both the 2D and 3D settings.

Our findings indicated that bKO#1 showed no significant differences in proliferative ability or metabolic activity compared to the control cells in either the 2D or 3D models (**Figure 19A-C**). In contrast, as expected, a substantial reduction in both proliferative capacity in the 2D and 3D cultures, as well as metabolic activity in the 2D model, was observed in the biallelic IMP2 knockout HCT116 cells (**Figure 19A-C**). Additionally, it was observed that the spheroids formed by the IMP2 knockout cells were smaller than those formed by both the AAVS1

knockout and wild-type cells, reflecting the reduced cell proliferation because of IMP2 knockout (**Figure 19D**).

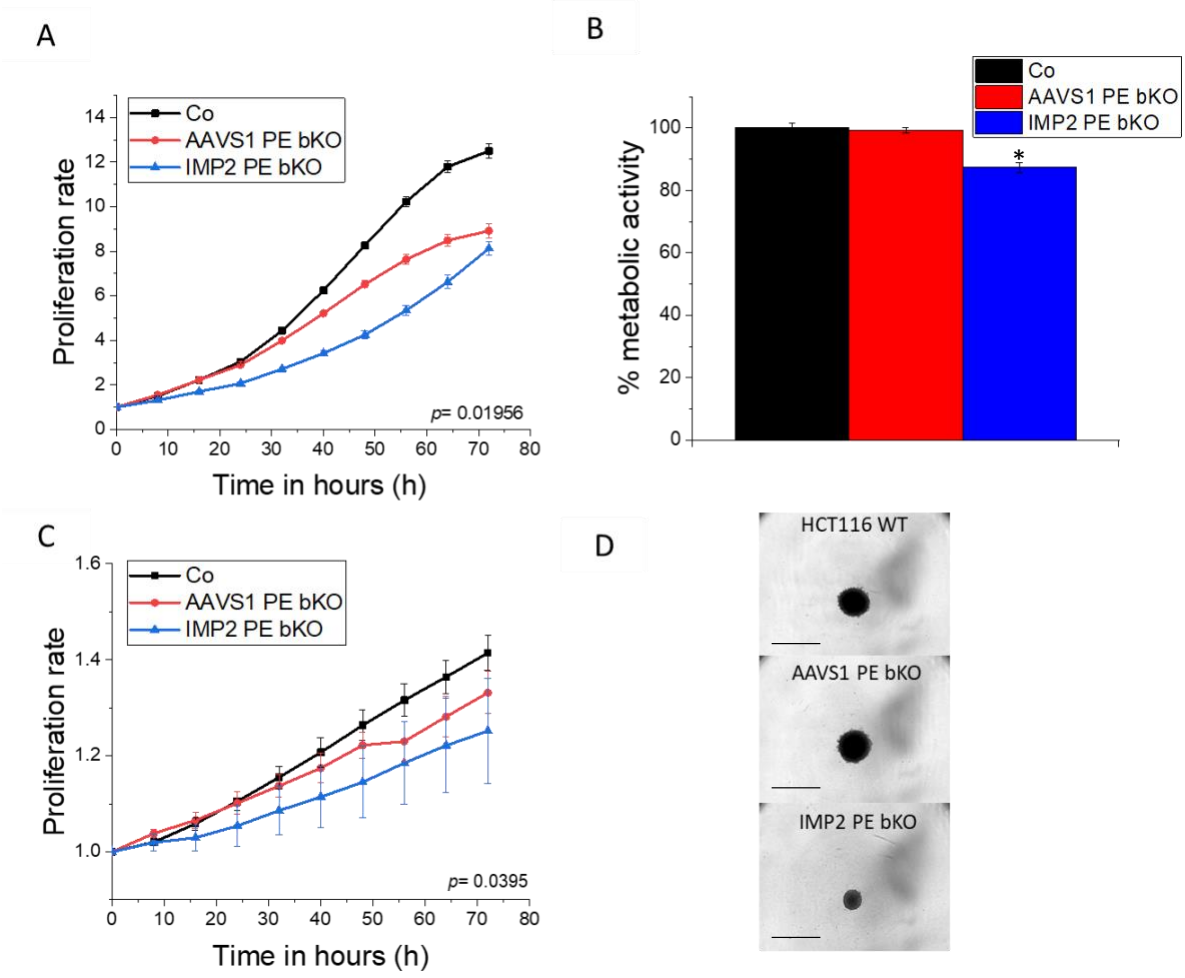

Figure 19. 2D and 3D proliferation study of biallelic AAVS1 and IMP2 knockout HCT116 cells generated by the prime editing approach. (A) 2D cell proliferation rate over 3 days was monitored using the IncuCyte® S3 system. Values were normalized to the time point of seeding (0 h). The proliferation rate was measured based on cell confluence. (B) Metabolic activity was measured *via* MTT assay at 72 h of the 2D cell proliferation assay. (C) Upon 2-d spheroid formation, the spheroid areas were monitored by an IncuCyte® S3 system for the next 3 days. The area was normalized to 2-d old spheroids (0 h). (D) Representative pictures of 5-d old spheroids (scale bar = 1 mm); Data are represented as means ± SEM, n=3 (quintuplicates). Statistical analysis was performed for the last acquired time point using one-way ANOVA followed by Bonferroni's post-hoc analysis. Significance values were determined by comparing the knockout cells to the control (Co) cells/wild-type HCT116 cell line. The p-value indicated in the graph shows a significant difference between biallelic IMP2 knockout HCT116 cells with the wild-type/control (Co).

To establish a negative knockout control for the prime editing method in the murine cell line LLC1 (since prior attempts were made to achieve IMP2 knockout in these cells), two pegRNAs were designed, denoted as pegRNAa and pegRNAb, targeting the Rosa26 region, details of which can be found in **Table 2.**

Transfection efficiency for each of the pegRNAs was approximately 20%, as illustrated in **Figure 20**. Upon transfection with pegRNAa, a total of 7 out of the 40 GFP-positive cells seeded managed to develop into single-cell colonies. However, subsequent Sanger sequencing analysis revealed that all of these clones carried sequences identical to the wild-type. Similarly, when pegRNAb was utilized for transfection, 18 out of the 60 GFP-positive cells seeded successfully grew into single-cell colonies. However, sequencing results indicated that all the clones shared an identical sequence with the wild-type.

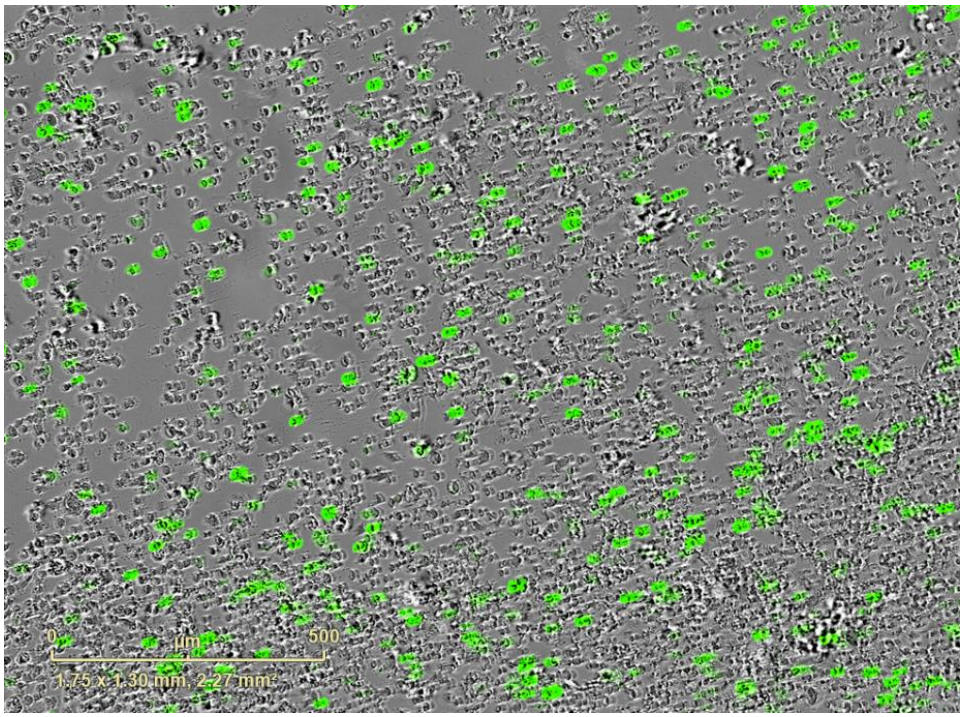

Figure 20. Proof of transfection in LLC1 cells using the prime editing approach. Representative picture of LLC1 cells co-transfected with Rosa26 knockout pegRNAa construct and PE2 at 24 h post-transfection. Cells appearing green indicate GFP expression confirming successful transfection of LLC1 cells. Scale bar = 500 µm. Image taken using IncuCyte® S3 system.

Prime editing-mediated IMP2 knockout trials

SW480 cells

To achieve an IMP2 knockout in SW480 cells, the prime editing approach employing pegRNA4_16 was pursued (**Table 2**). The transfection efficiency of this method in SW480 cells was 10%, as depicted in **Figure 21**.

To explore whether the f.sight™ settings, employed to obtain single cell-derived colonies, could inadvertently favor the growth of non-transfected SW480 cells, a controlled trial was conducted by seeding non-transfected SW480 cells. The results indicated that 9 out of 15 cells initially seeded in a 96-well plate were able to thrive, confirming the applicability of the f.sight™ setting for acquiring single-cell colonies of SW480 cells. However, despite three

attempts, the f.sight^{TM} settings did not facilitate the growth of transfected GFP-positive SW480 cells in the 96-well plate.

Alternatively, the manual picking method was employed, resulting in the successful growth of around 8 out of 30 GFP-positive SW480 cells seeded. However, subsequent Sanger sequencing confirmed that all the clones were identical to the wild-type sequence.

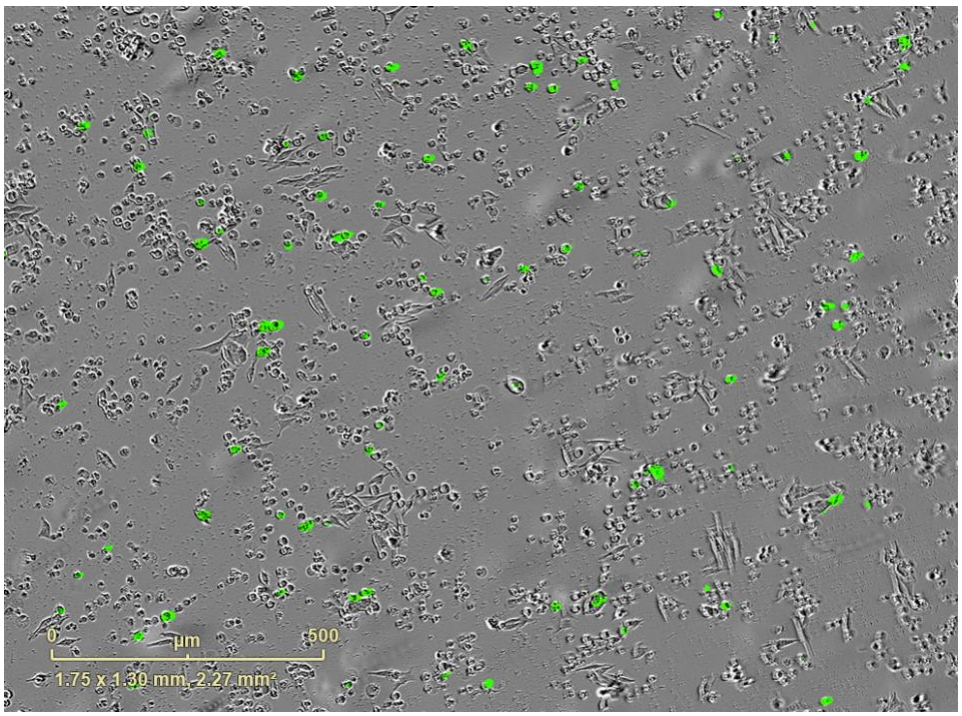

Figure 21. Proof of transfection in SW480 cells using the prime editing approach. Representative picture of SW480 cells co-transfected with pegRNA_16 and the PE2 system 24 h post-transfection. Cells appearing green indicate GFP expression confirming successful transfection of SW480 cells. Scale bar = 500 µm. The image was taken using the IncuCyte® S3 system.

Huh7 cells and HepG2

To achieve co-transfection of hepatocellular carcinoma cells (Huh7 and HepG2) using pegRNA_16 and PE2, an initial attempt was made employing the lipofectamine 3000 reagents. However, this approach yielded very low transfection efficiency (0.1%). To enhance transfection efficiency, an alternative approach with the use of the jetPEI hepatocyte DNA transfection reagents was adopted. Unfortunately, even up to 48 h post-transfection, no GFP-positive cells were observed.

To confirm the efficacy of the jetPEI hepatocyte transfection system, additional experiments were conducted on both Huh7 and HepG2 cells. These cells were transfected with an *IMP2* overexpressing plasmid (**Supplementary Figure 7**) and an *IMP2* control plasmid (**Supplementary Figure 8**). To optimize transfection conditions with minimal cellular toxicity from transfection components, media was changed at 4 h and 24 h post-transfection. At various

time points up to 24 h post-transfection, no GFP-positive cells were detected microscopically in either the *IMP2* overexpressing or control-transfected cells.

However, Huh7 and HepG2 cells were collected at 24 h post-transfection to evaluate *IMP2* expression using qPCR analysis. Additionally, HepG2 cells were collected at both 4 h and 24 h post-transfection to assess IMP2 expression through Western blot analysis. The results confirmed the success of transfection using the jetPEI hepatocyte system, demonstrated by the overexpression of *IMP2* in both tested cell lines (**Figure 22A**). Furthermore, the protein level of IMP2 was higher in HepG2 cells transfected with the IMP2 overexpressing plasmid compared to cells transfected with the control plasmid, as well as wild-type HepG2 cells (**Figure 22B, C**).

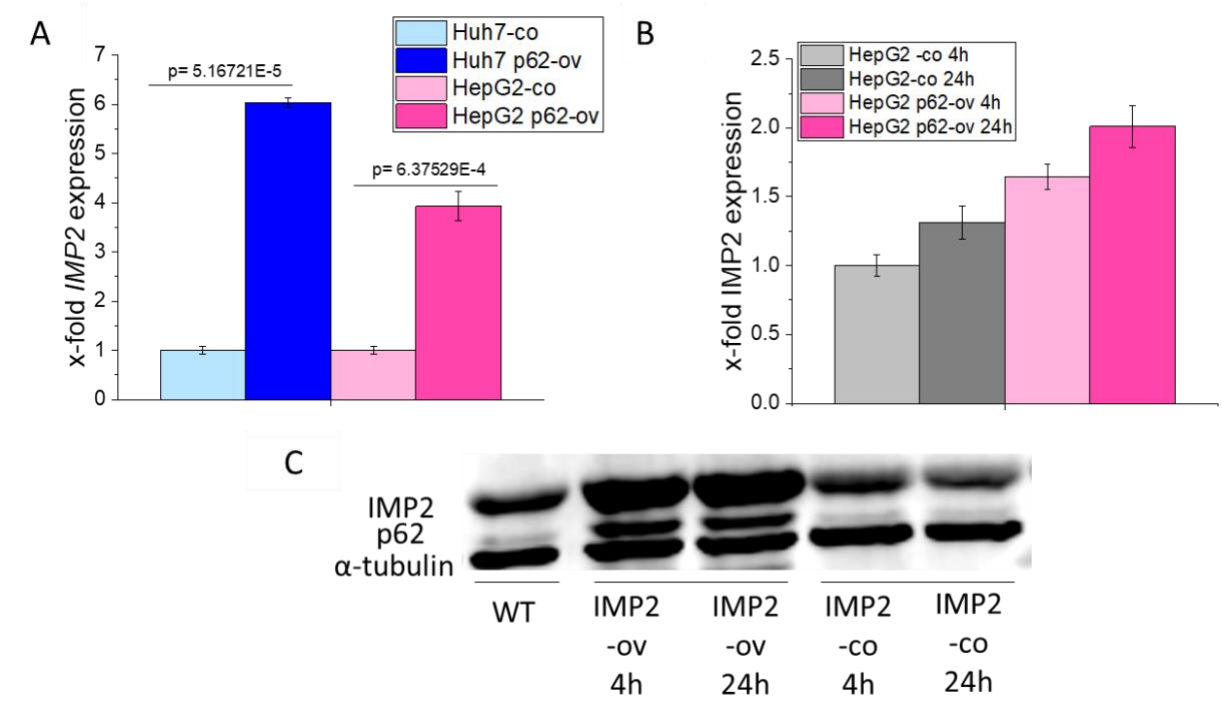

Figure 22. *IMP2* gene expression in Huh7 and Western blot quantification of IMP2/p62 in HepG2 cells upon transfection with *IMP2/p62* overexpressing plasmid. (A) *IMP2* gene expression was determined in Huh7 and HepG2 cells transfected with *IMP2* control (co) and *IMP2* overexpressing (ov) plasmid by qPCR. Values were normalized to the housekeeping gene *RNA18SN5*. Data has been shown as x-fold of Huh7-co. (B) Quantification of protein levels and (C) Western blot representation of IMP2/p62 expression in HepG2 upon transfection with co and *IMP2* ov plasmid, after media was changed 4 h and 24 h post-transfection. Data has been shown as x-fold of HepG2-co 4 h in panel (B). The IMP2 (66 kDa) was analyzed against alpha-tubulin (55 kDa) as a housekeeping protein. Representative blots were shown in (C) and (B) is not the quantification of the blot shown in (C). The expression was compared to wild-type (WT) HepG2 cells. Data are represented as mean ± SEM. n=2 (duplicates).

To proceed with the subsequent steps and verify successful transfection when co-transfecting PE2 and pegRNA_16, primers were designed to amplify the GFP region of the PE2 plasmid (**Supplementary Figure 9**). Media changes were performed at 4 h, 24 h, and 48 h post-transfection. At 48 h, cells were collected to assess GFP expression using qPCR analysis. The

results confirmed successful transfection, as evident from GFP expression in both Huh7 (**Figure 23A**) and HepG2 (**Figure 23B**) cells. In contrast, non-transfected cells showed no GFP expression, in line with expectations (data not shown).

Based on these results, the optimal parameters for media change were established as 4 h post-transfection, and single-cell selection was set at 24 h post-transfection, given the robust GFP expression and overall good cell health observed. Notably, Huh7 cells exhibited superior GFP expression and cell viability compared to HepG2 cells at the 24 h time point post-transfection, prompting further work to be conducted using Huh7 as the hepatocellular cell line for achieving IMP2 knockout.

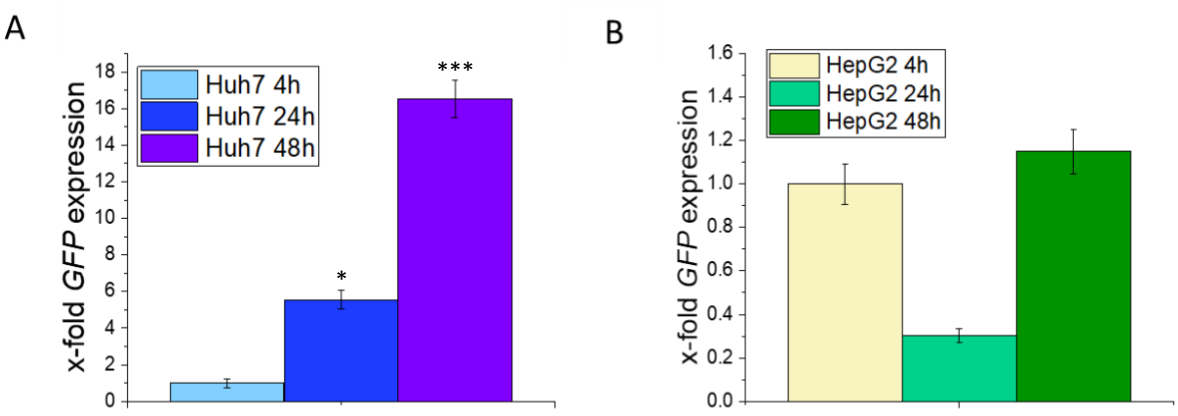

Figure 23. *GFP* expression was determined in (A) Huh7 and (B) HepG2 cells transfected with PE2 plasmid and media changed after 4 h, 24 h, and 48 h post-transfection by qPCR analysis. Values were normalized to the housekeeping gene *RNA18SN5*. Data are represented as mean ± SEM. n=2 (triplicates). *p < 0.05, **p < 0.01, and ***p < 0.001 compared to values of Huh7 4 h in panel (A). Data has been shown as x-fold of Huh7 4 h in panel (A) and HepG2 4 h in panel (B).

To address the challenges posed by low transfection efficiency and the absence of microscopically visible GFP-positive cells encountered in attempting IMP2 knockout through the prime editing approach, an alternative method was adopted. The plasmid-based CRISPR/Cas9 approach was chosen as the subsequent strategy for achieving IMP2 knockout in hepatocellular carcinoma (Huh7) cells, as outlined in the forthcoming section of this thesis.

A549 cells

Initially, the A549 cell line's capability to develop as single-cell colonies using the manual cell-picking method was evaluated. Non-transfected cells were individually picked 48 h post-seeding and permitted to grow for one week. Out of the 50 cells initially seeded, 36 clones successfully grew, underscoring their potential to establish single-cell colonies. Upon conducting co-transfection with PE2 and pegRNA_16, a transfection efficiency of approximately 20% was achieved 24 h post-transfection. Nevertheless, none of the 50 GFP-positive cells seeded were able to evolve into single-cell colonies.

LLC1 cells

The prime editing approach was employed in LLC1 cells to achieve an IMP2 knockout. Two pegRNAs, named pegRNAI and pegRNAII, were employed (**Table 3**). The transfection efficiency for each pegRNA was approximately 20%. Upon transfection with pegRNAI, 60 out of 80 GFP-positive cells that were seeded managed to develop into single-cell colonies. However, all the resulting clones were found to possess sequences identical to the wild-type, as confirmed by Sanger sequencing. Conversely, upon transfection with pegRNAII, none of the 40 GFP-positive cells seeded were able to grow into single-cell colonies.

Plasmid-based CRISPR/Cas9 approach for IMP2 knockout

Huh7 cells

To eliminate any impact from the manual single-cell picking procedure and subsequent culturing, we applied the entire single-cell colony expansion process to non-transfected Huh7 cells. Interestingly, both non-transfected cells and GFP-negative cells subjected to the same transfection technique managed to form colonies. This result further confirmed that Huh7 cells can indeed proliferate and develop into single-cell colonies.

In this approach, the CRISPR/Cas9-based method was utilized to generate IMP2 knockout in Huh7 cells. Two gRNAs, gRNA1, and gRNA2, were employed in three different approaches: gRNA1 alone, gRNA2 alone, and a combination of gRNA1 and gRNA2. The transfection efficiency for all three approaches was approximately 10% when observed 24 h post-transfection, as depicted in **Figure 24**. Unfortunately, only one clone from the gRNA2-transfected Huh7 cells was able to grow out of all the attempts. This clone, designated as clone 1, was further cultured until sequencing results were obtained. Sanger sequencing analysis revealed a monoallelic T substitution near the expected cut site (**Figure 25**). However, such an edit does not result in the knockout of IMP2, and therefore, no further investigation was carried out using clone 1.

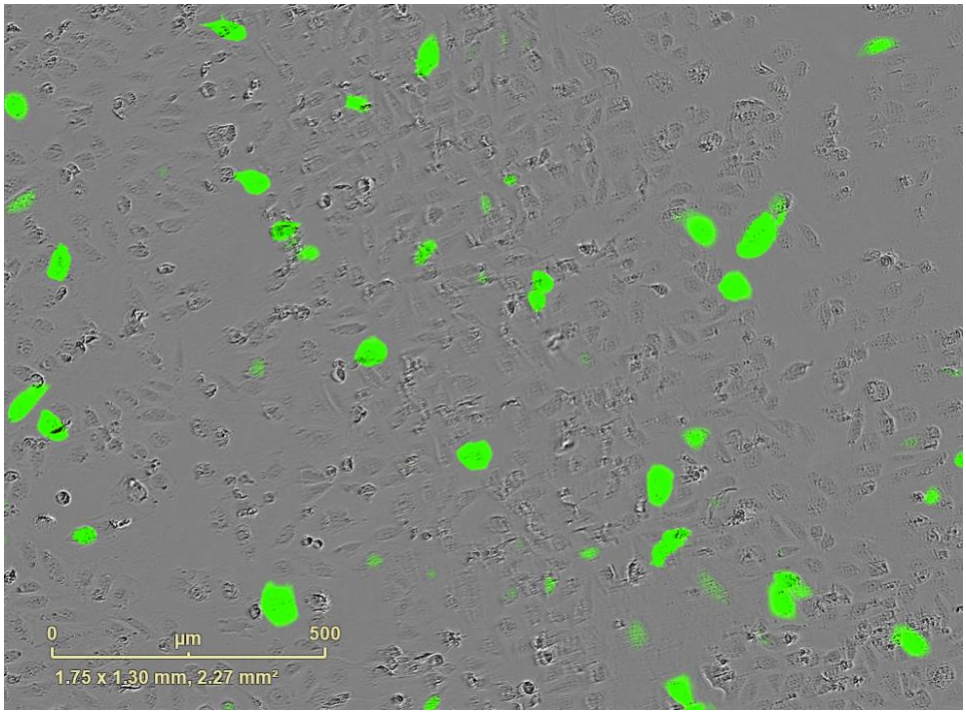

Figure 24. Proof of transfection in Huh7 cells using CRISPR/Cas9 approach. Representative picture of Huh7 cells transfected with gRNA1, 24 h post-transfection. Scale bar = 500 µm. Cells appearing green indicate GFP expression confirming successful transfection of Huh7 cells. Image taken using IncuCyte® S3.

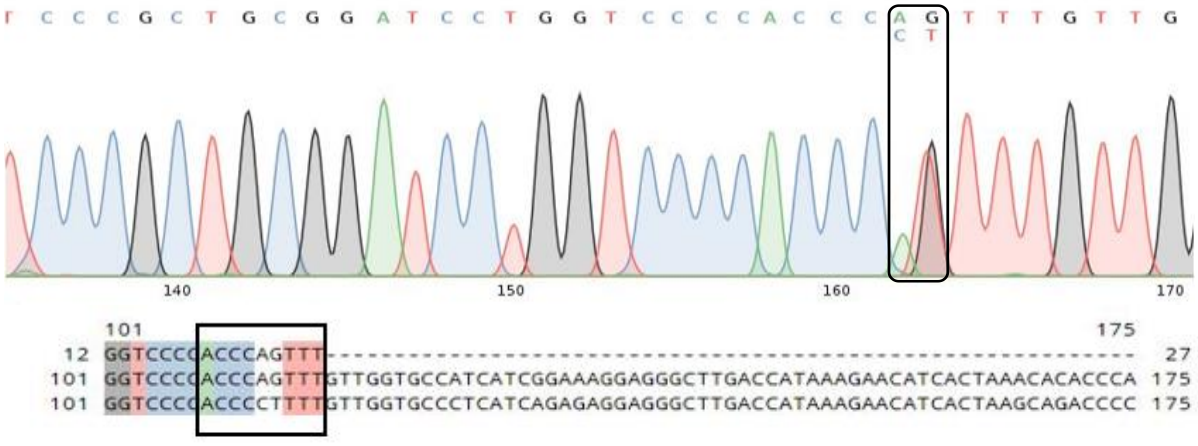

Figure 25. Monoallelic T substitution in clone 1 (Huh7) using gRNA2-mediated CRISPR/Cas9 approach detected by Sanger sequencing. The first line of the alignment represents the wild-type sequence. Two lines below the reference indicate different sequences of each allele (monoallelic editing). Black frames in the sequence alignments demonstrate the section shown in the chromatograms above. Color code visualizes matches in aligned sequences. A: adenine (green), C: cytosine (blue), G: guanine (black), and T: thymine (red).

To test the hypothesis that the inability of successfully edited single cells to proliferate into a colony stems from IMP2's role in cell survival and proliferation, we conducted next-generation sequencing of GFP-positive cells picked 24 h post-transfection. These cells were either individually transfected with gRNA1 or co-transfected with a combination of gRNA1 and gRNA2 in Huh7 cells. Additionally, we included a control batch of non-transfected Huh7 cells to validate the next-generation sequencing method.

In the case of Huh7 cells transfected with gRNA1, the analysis revealed an editing efficiency of 22.41% (**Figure 26B**). Conversely, analysis of non-transfected Huh7 cells using gRNA1 adapter primers demonstrated that 98.33% of alleles (**Figure 26A**) aligned with the reference sequence near the gRNA1 target site. Notably, the modifications illustrated in **Figure 26** include base insertions, deletions, and substitutions.

Next-generation sequencing analysis of Huh7 cells transfected with both gRNA1 and gRNA2 unveiled a 96-base pair deletion between the anticipated cut sites of the two sgRNAs, as determined *via* the gRNA1 adapter primer system (**Figure 27**). This offers additional evidence substantiating the high editing efficiency of gRNA1 and gRNA2.

In summary, the observed lack of growth in transfected single cells can be attributed to the knockout of IMP2, which compromises their ability to proliferate and form colonies. For a detailed reference, **Supplementary Table 2** presents the comprehensive NGS sequencing data.

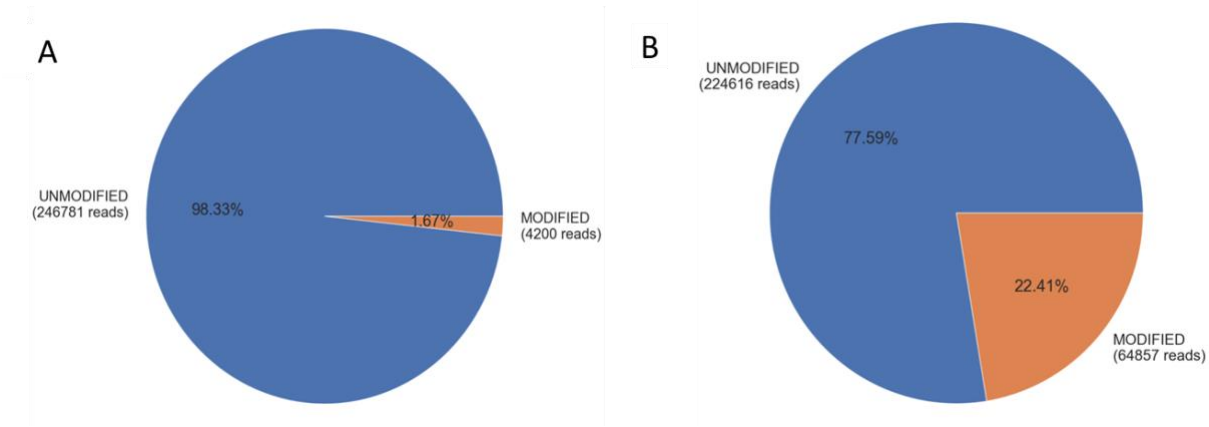

Figure 26. Next-generation sequencing results of non-transfected Huh7 cells and gRNA1-transfected Huh7 cells using gRNA1 adapter primers. Panel (A) represents non-transfected Huh7 cells and (B) gRNA1-transfected Huh7 cells. Both were analyzed using gRNA1 adapter primers. The pie charts illustrate the percentage and number of reads, indicating unmodified alleles (blue) and modified alleles (orange).

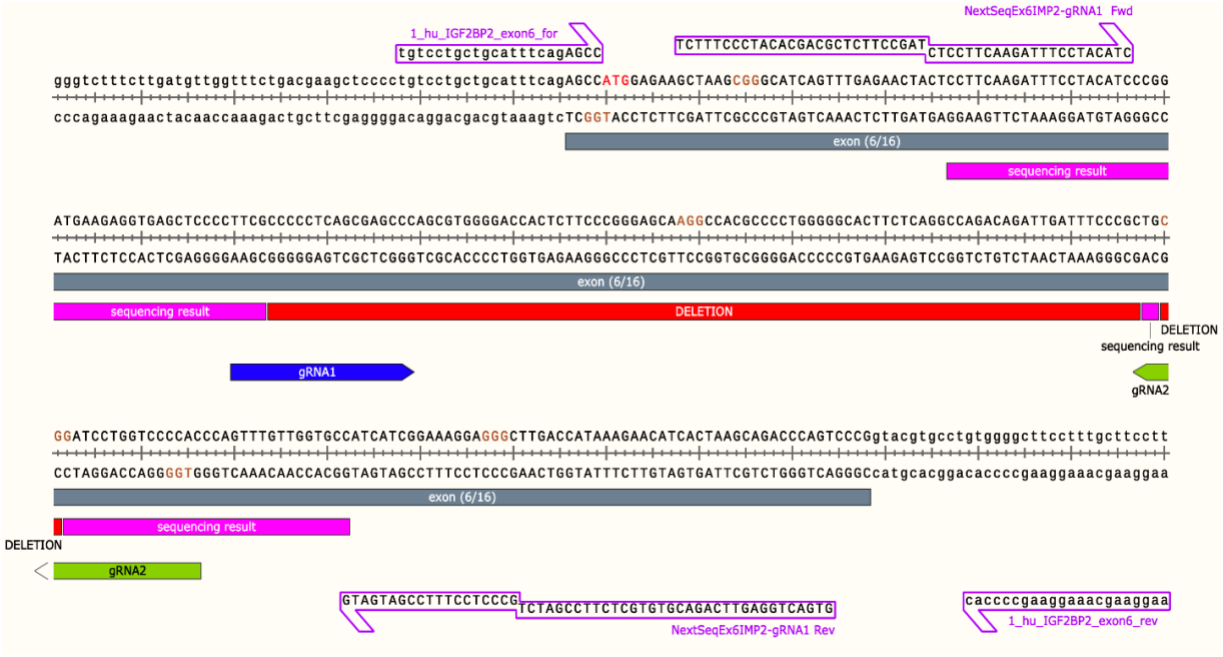

Figure 27. Editing efficiency of gRNA1 and gRNA2 in combination in Huh7 cells. Sequence view of the sequence alignment with the reference genome. Nucleotides indicated by the pink bar represent the sequencing result and the red bar indicates the 96 bp deletion between the gRNA1 and gRNA2 shown in blue and green bars respectively in the target region of exon 6 of *IGF2BP2*. The image was created using SnapGene®.

A549 cells

Attempts to generate IMP2 knockouts in A549 using the CRISPR/Cas9 approach also proved unsuccessful (**Supplementary Table 1**). To eliminate any influence of the manual single-cell picking procedure and subsequent culture, we applied the entire single-cell colony expansion procedure to non-transfected A549 cells. Both non-transfected cells and GFP-negative cells that underwent the same transfection technique managed to form colonies. This outcome further confirmed that A549 cells indeed possess the capacity to proliferate and develop into single-cell colonies.

To achieve A549 IMP2 knockout, we employed the plasmid-based CRISPR/Cas9 approach using gRNA1 and gRNA2 individually (**Table 3**). The transfection efficiency for both gRNA1 and gRNA2 was approximately 50% at 24 h post-transfection, as depicted in **Figure 28**. However, only one clone of A549 cells transfected with gRNA1 was able to grow successfully. This clone, referred to as clone 1, was cultured until sequencing results were obtained. Sanger sequencing analysis revealed a monoallelic T substitution at the expected cut site (**Figure 29**). Unfortunately, this edit alone would not result in IMP2 knockout, rendering further work with this clone unfeasible.

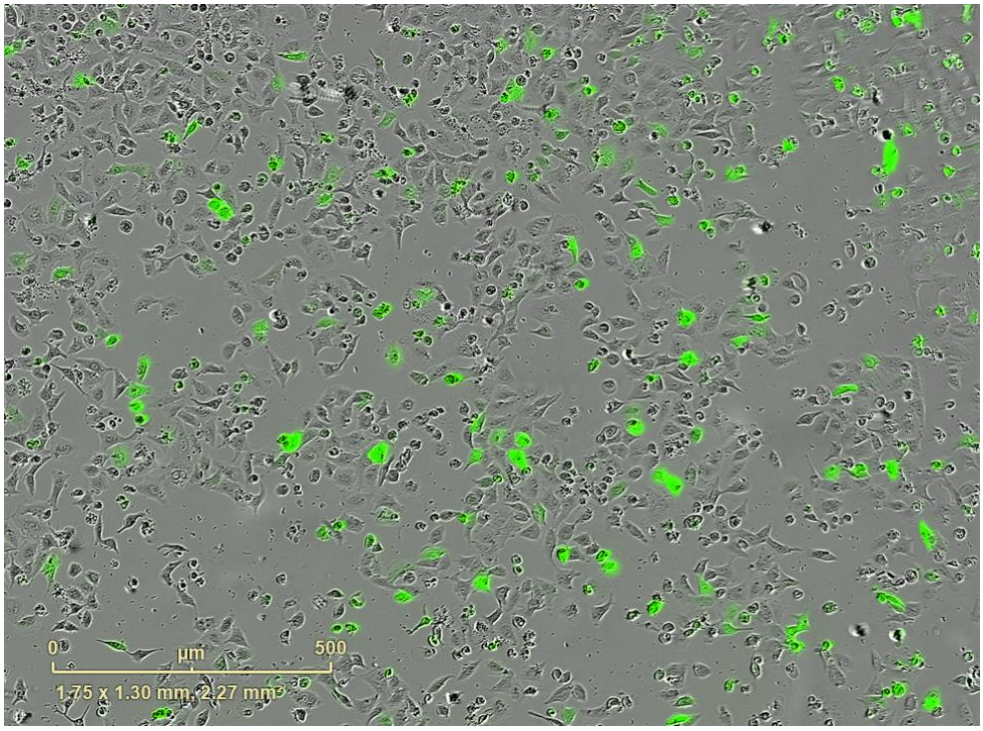

Figure 28. Proof of transfection in A549 cells using CRISPR/Cas9 approach. Representative picture of A459 cells transfected with gRNA2 24 h post-transfection. Cells appearing green indicate GFP expression and therefore successful transfection of A549 cells. Scale bar = 500 µm shown in the lower left corner. Image taken using IncuCyte® S3.

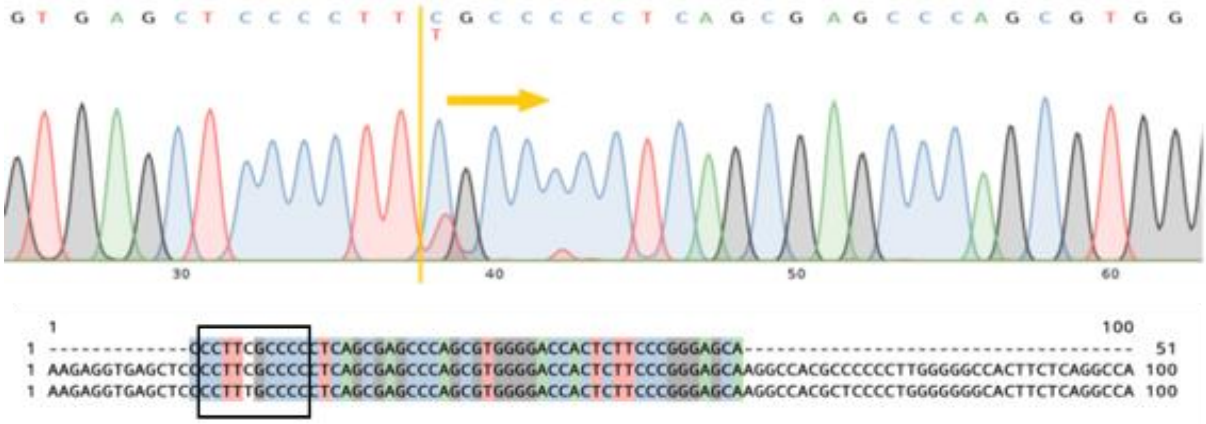

Figure 29. Monoallelic T substitution in clone 1 (A549) using gRNA1-mediated CRISPR/Cas9 approach detected by Sanger sequencing. The first line of the alignment represents the wild-type sequence. Two lines below the reference indicate different sequences of each allele (monoallelic editing). Black frames in the sequence alignments demonstrate the section shown in the chromatograms above. Yellow arrows highlight the start site of at least two different sequences/alleles in cell clones. Color code visualizes matches in aligned sequences. A: adenine (green), C: cytosine (blue), G: guanine (black), and T: thymine (red).

The lack of growth observed in transfected single cells could potentially be attributed to the knockout of IMP2, as IMP2 may play a crucial role in the proliferation of A549 cells. To investigate this hypothesis, next-generation sequencing (NGS) was performed on the transfected A549 cells using gRNA1 and gRNA2 to assess the editing efficiency of the employed gRNAs.

Transfection of A549 cells with gRNA1 and gRNA2 resulted in successful editing at the intended cut site, with modifications of 21.97% for gRNA1 (**Figure 30B**) and 83.66% for gRNA2 (**Figure 30D**), showcasing the high editing efficiency of gRNA2. Notably, the modifications illustrated in **Figure 30** encompass base insertions, deletions, and substitutions. Sequencing control A549 cells with gRNA1 and gRNA2 adapter primers showed sequences with 99% and 98.9% similarity to the reference sequence, respectively (**Figure 30A, C**). The sequence reads are provided in **Supplementary Table 2**.

In conclusion, these findings bolster the hypothesis that IMP2 is essential for A549 cell proliferation, as evidenced by the lack of colony formation in transfected single cells and the successful editing outcomes observed.

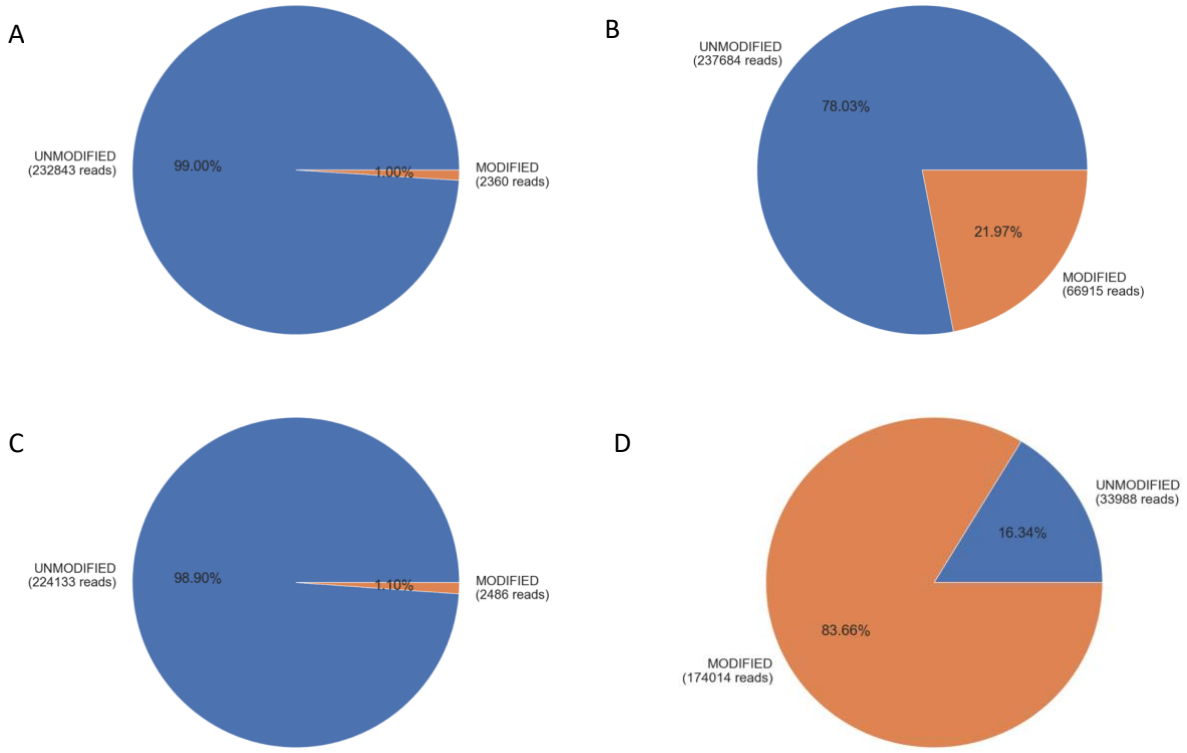

Figure 30. Editing efficiency of gRNA1 and gRNA2 in A549 cells and NGS results for non-transfected A549 cells using gRNA1 and gRNA2 adapter primers. Panel (A) represents non-transfected A549 cells analyzed with gRNA1 adapter primers, while panel (B) represents gRNA1-transfected A549 cells. Panel (C) represents non-transfected A459 cells analyzed with gRNA2 adapter primers, while panel (D) represents gRNA2-transfected A459 cells. The pie charts illustrate the percentage and number of reads, indicating unmodified alleles (blue) and modified alleles (orange).

LLC1 cells

Two gRNAs, namely gRNAI and gRNAII, were employed for IMP2 knockout in LLC1 cells (**Table 3**). Three approaches were undertaken as follows: (1) gRNAI alone, (2) gRNAII alone, and (3) a combination of gRNAI and gRNAII. The transfection efficiency 24 h post-transfection for all three approaches was approximately 20%. In the first approach using gRNAI, 14 out of 30 GFP-positive cells seeded were able to grow. In the second approach using gRNAII, 28 out of 35 GFP-positive cells seeded exhibited growth. In the third approach, using both gRNAs, 15 out of 30 GFP-positive cells successfully grew. **Figure 31** presents the diverse types of editing observed in the IMP2 knockout LLC1 clones, as discerned from the sequencing data.

Validation of IMP2 knockout on gene level in LLC1 cells

Six different mutation types were observed as follows:

1. biallelic editing with different mutations per allele, i.e., AAGAGG deletion in one allele and GAAG deletion in the other allele (clone bKO1),
2. biallelic editing with different mutations per allele like CA deletion in one allele and A deletion in the other allele (clone bKO2).
3. biallelic editing with different mutations per allele T deletion in one allele and TTGTTG deletion in the other allele (clone bKO3),
4. biallelic T deletion (clone bKO4),
5. biallelic 41 bp deletion (clone bKO5), and
6. biallelic T insertion (clone bKO6).

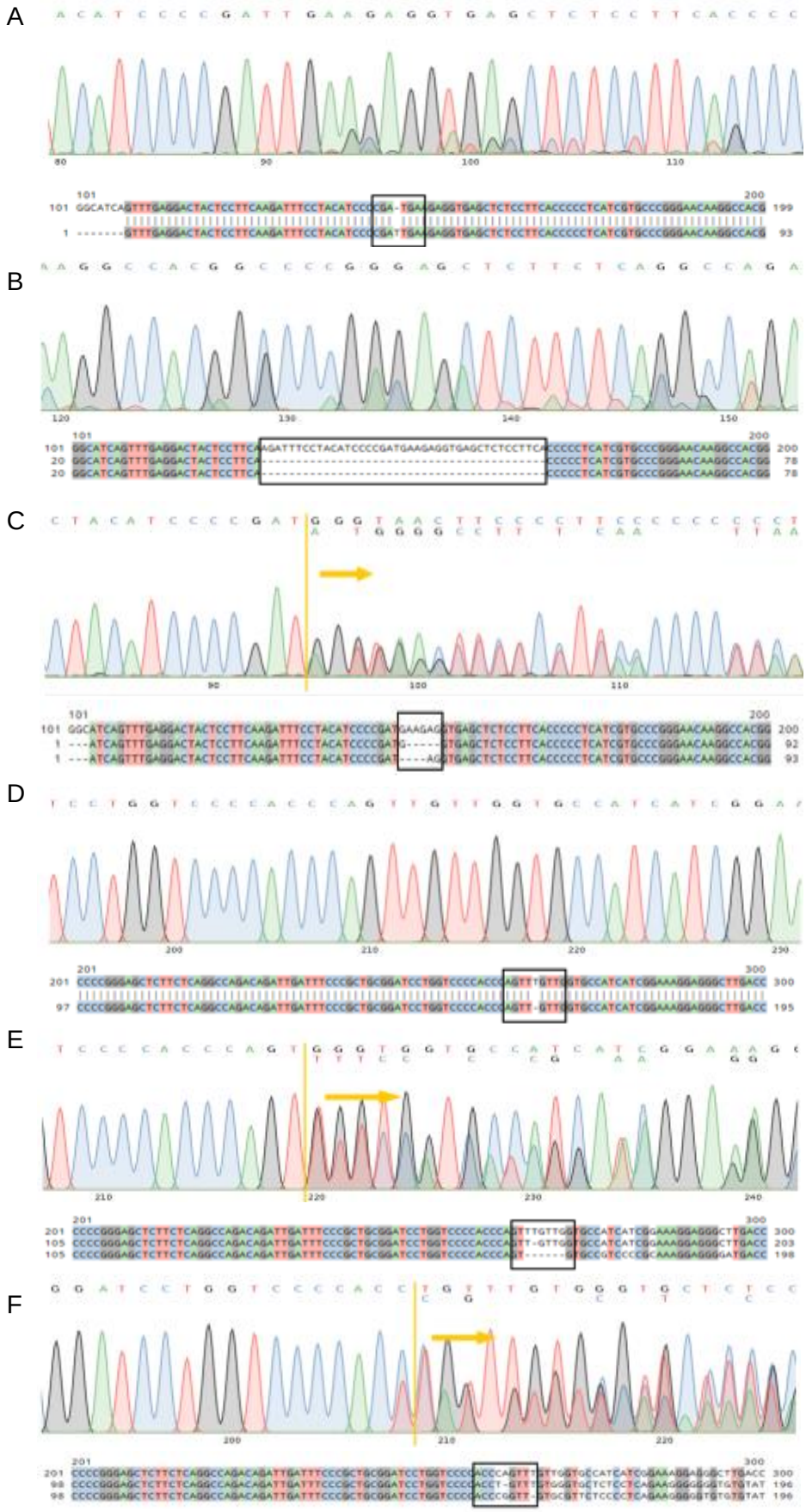

Figure 31. Mutations were observed through Sanger sequencing in LLC1 IMP2 knockout clones resulting from CRISPR/Cas9 approach. The sequencing chromatograms and corresponding sequence

alignments with wild-type reference are presented above, depicting different editing events in the *Igf2bp2* target locus. Panels show (A) biallelic T insertion (clone bKO6), (B) biallelic 41 bp deletion (clone bKO5), (C) biallelic editing with different mutations per allele (AAGAGG deletion in one allele and GAAG deletion in the other allele (clone bKO1), (D) biallelic T deletion (clone bKO4), (E) biallelic editing with different mutations per allele T deletion in one allele and TTGTTG deletion in the other allele (clone bKO3), and (F) biallelic editing with different mutations per allele like CA deletion in one allele and A deletion in the other allele (clone bKO2). The first line of the alignment represents the reference sequence, while the line/lines below represent the edited sequence. The site of editing is highlighted by a black frame. The yellow arrow highlights the start site of the edit in the clone. Nucleotides are visually represented using the following color codes; A: adenine (green), C: cytosine (blue), G: guanine (black), and T: thymine (red). A missing DNA base is indicated by a dash (-).

Validation of biallelic IMP2 knockout LLC1 cells on protein level

The reduction in IMP2 expression in the biallelic IMP2 knockout LLC1 clone was verified through Western blot analysis (**Figure 32**). To assess the possible off-target effects of the transfection procedure, an editing control LLC1 clone named WT2 was incorporated into the experimental analysis. This control clone was derived from an experiment where cells were transfected with both gRNAI and gRNAII but chosen from non-GFP-positive cells. Sanger sequencing confirmed WT2 as a wild-type clone.

Quantification of protein levels in the LLC1 clones revealed a significant reduction, with approximately 5-10% residual IMP2 expression in comparison to the parental wild-type (WT1) cells, as evident in clone bKO4 (**Figure 32A, B**). Western blots of biallelic edited clones displayed a faint band at the position of the IMP2 66 kDa protein (**Figure 32B**), except for clone bKO6. Furthermore, a faint and barely visible band was observed at the position of p62 at 62 kDa (**Figure 32B**), signifying a noteworthy reduction in IMP2 and p62 expression in the knockout clones. Given that clone bKO6 exhibited up to 65% IMP2 expression, this clone was excluded from further characterization, focusing on the investigation of the other five clones (KO1-5).

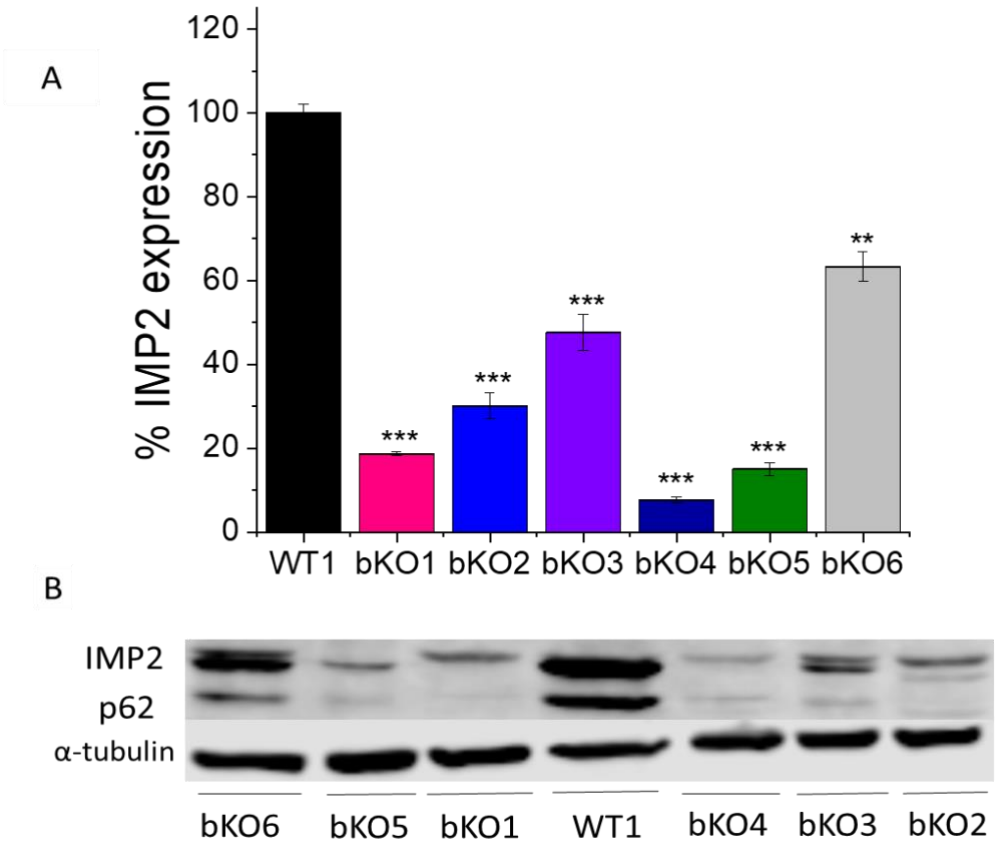

Figure 32. Western blot analyses of biallelic IMP2 knockout LLC1 clones resulting from CRISPR/Cas9 approach. (A) The protein levels of IMP2 and p62 were quantified in biallelic knockout (bKO) LLC1 clones and compared to wild-type/bulk (WT1) LLC1 cells. IMP2 (66 kDa) and its splice variant p62 (62 kDa) were analyzed against alpha-tubulin (55 kDa) serving as the housekeeping protein. (B) Representative Western blots are shown. The bars represent mean ± SEM. n=2 (duplicates). *p < 0.05, **p < 0.01, and ***p < 0.001 compared to values of WT1 cells.

IMP2 target validation in vitro

Target specificity of IMP2 knockout in HCT116 cells

Rescue experiments were conducted by Dr. Charlotte Dahlem, involving the overexpression of *IMP2/p62* in the biallelic IMP2 knockout HCT116 clones KO#1 (CRISPR/Cas9-generated) and KO#2 (prime editing-generated). The rescue process resulted in the restoration of both the 2D proliferative capacity and the metabolic activity of the knockout clones (Dahlem, Abuhaliema, et al., 2022).

The gene expression levels of *IMP2* and *p62* were quantified in the parental HCT116 cells, followed by the biallelic IMP2 knockout clones, and upon *IMP2/p62* overexpression in clone KO#1. As anticipated, reduced *IMP2* and *p62* expression were observed in both knockout

clones, and a substantial increase in expression was evident upon *IMP2/p62* overexpression in clone KO#1 (**Supplementary Figure 3**).

Subsequently, the impact of IMP2 knockout on the expression of established IMP2 targets, including *IMP1*, *IMP3*, *TSC1*, *PPAR-γ, IGF1R, IGF2, HMGA1, HMGA2, DANCR*, and *MYC*, was analyzed. The knockout cells displayed a noteworthy reduction in the expression of *DANCR* (analyzed by Dr. Charlotte Dahlem) and the oncogene *MYC* (**Figure 33A, B**), both of which were restored through *IMP2/p62* overexpression (**Figure 33C, D**). However, the knockout clones did not exhibit reduced expression in the case of the other tested targets listed above, and no consistent trend in expression change was observed upon *IMP2/p62* overexpression (**Supplementary Figure 4**).

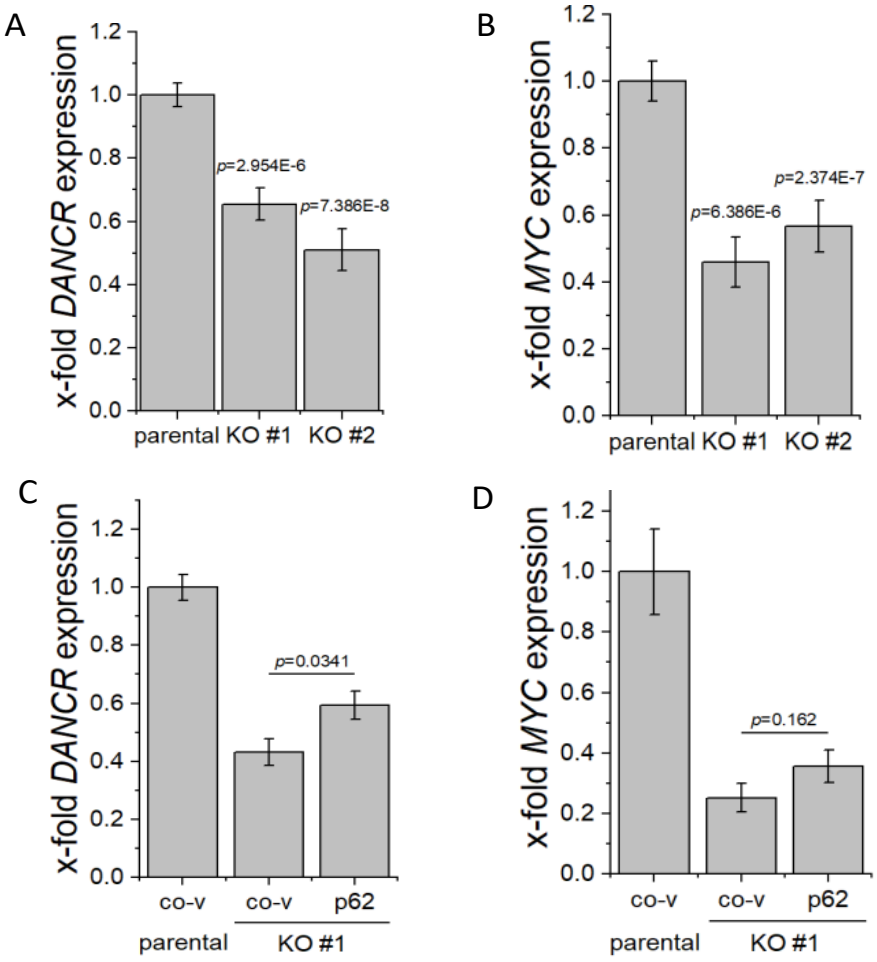

Figure 33. *DANCR* and *MYC* gene expression were determined in biallelic IMP2 knockout HCT116 clones and *IMP2/p62* overexpressing parental and knockout cells by qPCR (Dahlem, Abuhaliema, et al., 2022).

Effect of IMP2 inhibitors on IMP2 target expression in HCT116 and SW480 cells

The treatment of IMP2 inhibitor compounds 4, 6, and 9 on wild-type HCT116 and SW480 cells resulted in decreased expression of IMP2 targets, namely *DANCR*, *MYC*, and *HMGA1*, in both the 2D and 3D culture conditions (**Figure 34**). The analysis of the 3D data was conducted and evaluated by Mr. Simon Both. Conversely, treatment with the compounds had no observable impact on the expression of other IMP2 targets, namely *HMGA2*, *PPAR-γ, TSC1,* and *IGF2*, in the 2D culture of both HCT116 and SW480 cells (**Supplementary Figure 5**). A notable exception was observed when treating HCT116 cells with compound 6, resulting in a significant reduction in *HMGA2, PPAR-γ,* and *TSC1* expression. Furthermore, treatment with compounds 4 and 6 on SW480 cells led to a significant increase in *PPAR-γ* expression.

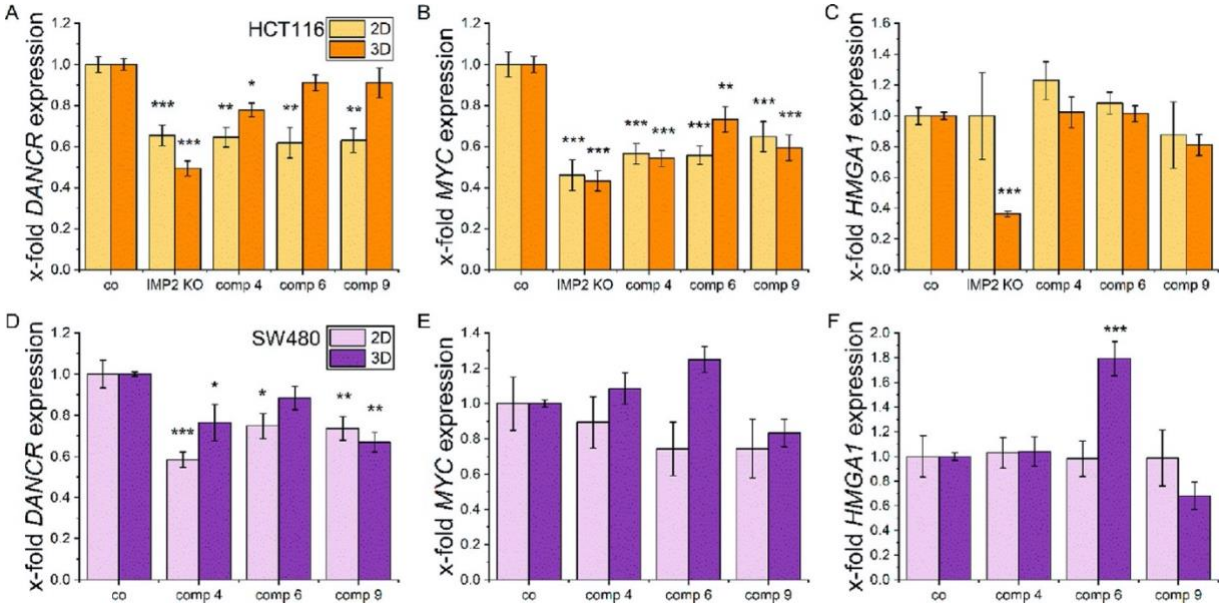

Figure 34. Expression of tumor-promoting *DANCR, MYC, and HMGA1* upon IMP2 inhibitor compound treatment in both the 2D and 3D cell culture models of wild-type HCT116 and SW480 cells (Dahlem, Abuhaliema, et al., 2022).

The IMP2 inhibitor compounds showed no significant changes in the gene and protein expression of IMP2 in both HCT116 and SW480 cells. An exception is the treatment with compound 4 which showed a reduction of IMP2 in the SW480 cells **(Figure 35**).

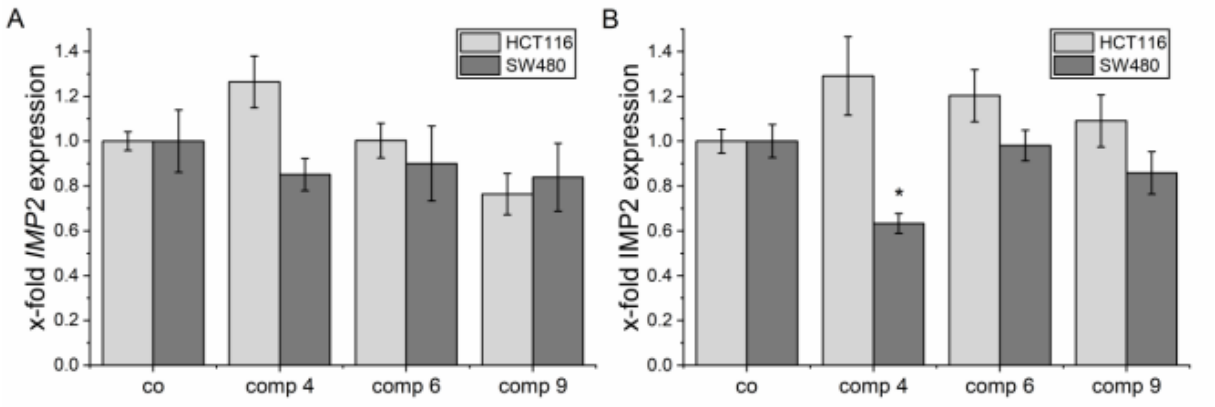

Figure 35. Quantification of IMP2 expression on gene and protein levels of wild-type HCT116 and SW480 cells upon IMP2 inhibitor compound treatment (Dahlem, Abuhaliema, et al., 2022).

Characterization of IMP2 knockout cells and small molecule IMP2 inhibitors in vitro

To conduct the *in vitro* IMP2 target analysis, biallelic knockout clones were utilized where available. However, for cell lines in which achieving a biallelic knockout (bKO) was not possible, monoallelic knockout (mKO) clones were employed. The IMP2 protein levels in the monoallelic knockouts have been previously published. The mean values were close to 80% for Huh7, 44% for HepG2, and 57% for SW480 (Dahlem, Abuhaliema, et al., 2022), while the expression of IMP2 in the biallelic LLC1 knockouts is shown in **Figure 32**.

The 2D proliferation data and the metabolic activity assessed indicated that there were no significant differences between the parental cells and the biallelic IMP2 knockout LLC1 cells (**Figure 36A-B**). However, the growth rate of the two wild-type controls varied quite strongly. Compared to the WT2 control, which had undergone the same treatment as the knockout clones, clones #bKO1-3 and 5 showed a trend toward reduced proliferation. No apparent morphological changes were observed in the wild-type and biallelic IMP2 knockout LLC1 cells (**Supplementary Figure 6A**). No effect was seen in the proliferation of the monoallelic knockout clones of Huh7 (**Figure 36C**). Although not statistically significant, a trend towards reduced proliferation was observed for the SW480 monoallelic knockout clone at later time points (**Figure 36D**). Importantly, a significant reduction in proliferation was observed in the HepG2 IMP2 knockout clone (**Figure 36B**).

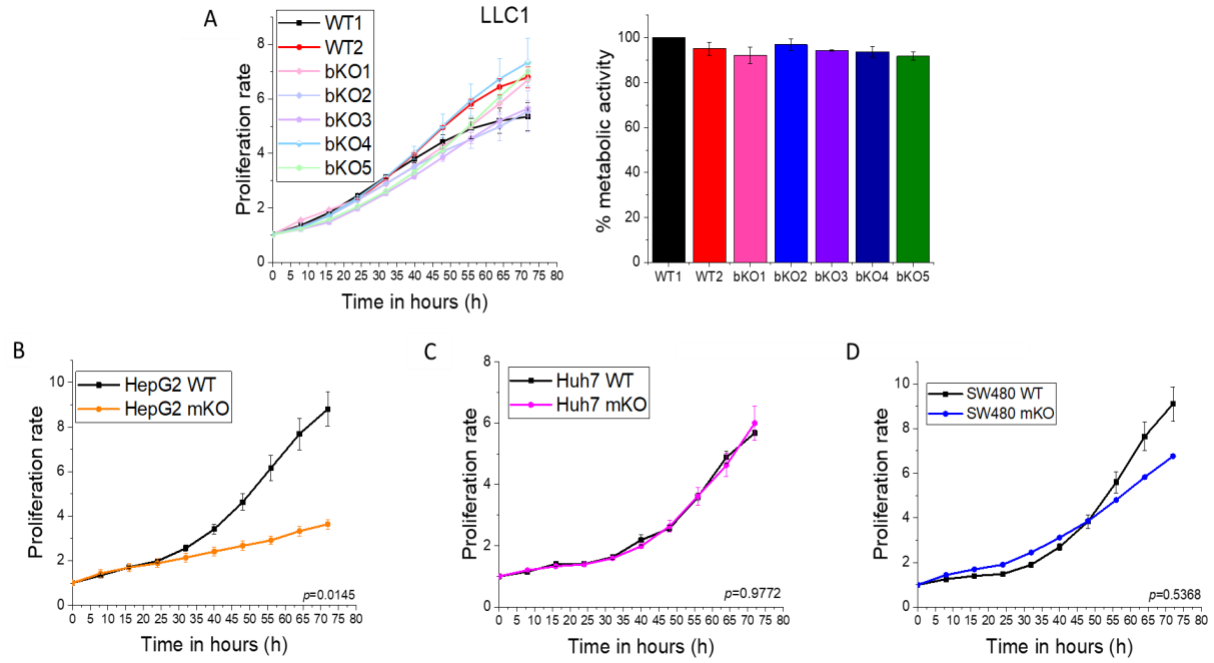

Figure 36. Effect of IMP2 knockout on the 2D cell proliferation. (A) LLC1, (B) HepG2, (C) Huh7, and (D) SW480 were assessed for their effect on the 2D cell proliferation using the IncuCyte® S3 live cell imaging system. (A) The right panel shows the metabolic activity measured *via* MTT assay at 72 h of the 2D cell proliferation of LLC1 IMP2 knockout clones. LLC1 IMP2 knockouts were biallelic, while the Huh7, HepG2, and SW480 cells were monoallelic IMP2 knockouts. Data normalized to WT1 for LLC1 KO clones and WT cells for other knockouts. WT1 is the bulk LLC1 and WT2 is the editing control LLC1. Data were normalized to time point 0 h, and are represented as mean ± SEM, n=3, quintuplicates. Significance values were determined by comparing the knockout cells to those obtained from the wild-type (WT) cells at all time points. The proliferation rate was determined based on the cell confluence.

3D cell culture models, also known as multicellular tumors (MCTs) or spheroids, closely resemble the structural organization, oxygen and nutrient gradients, and pH conditions of *in vivo* solid tumors (Han et al., 2021). Based on compactness, spheroid/multicellular tumors (MCTs) are categorized as compact spheroids and loose aggregates of cells (Han et al., 2021). Compact spheroids are tightly bound to each other, making it difficult to distinguish single cells, whereas loose spheroids cannot form complete spheres and can be easily disintegrated (Han et al., 2021). In some tumor cell types, they fail to aggregate into one single entity and exist as several small colonies of cells, which are referred to as satellite colonies. We observed a loss in the ability to form compact spheroids upon the knockout of IMP2. All wild-type clones except for Huh7 successfully formed compact spheroids three days after seeding. In contrast, the biallelic IMP2 knockout LLC1 cells and the monoallelic IMP2 knockout SW480 cells showed a change in cell adhesion and formed loose aggregates, while the monoallelic HepG2 IMP2 knockouts formed satellite colonies. This characteristic persisted even after 6 days of observation (**Figure 37**). Parental Huh7 cells also showed the formation of satellite colonies and did not form spheroids throughout the 6-day observation period (data not shown).

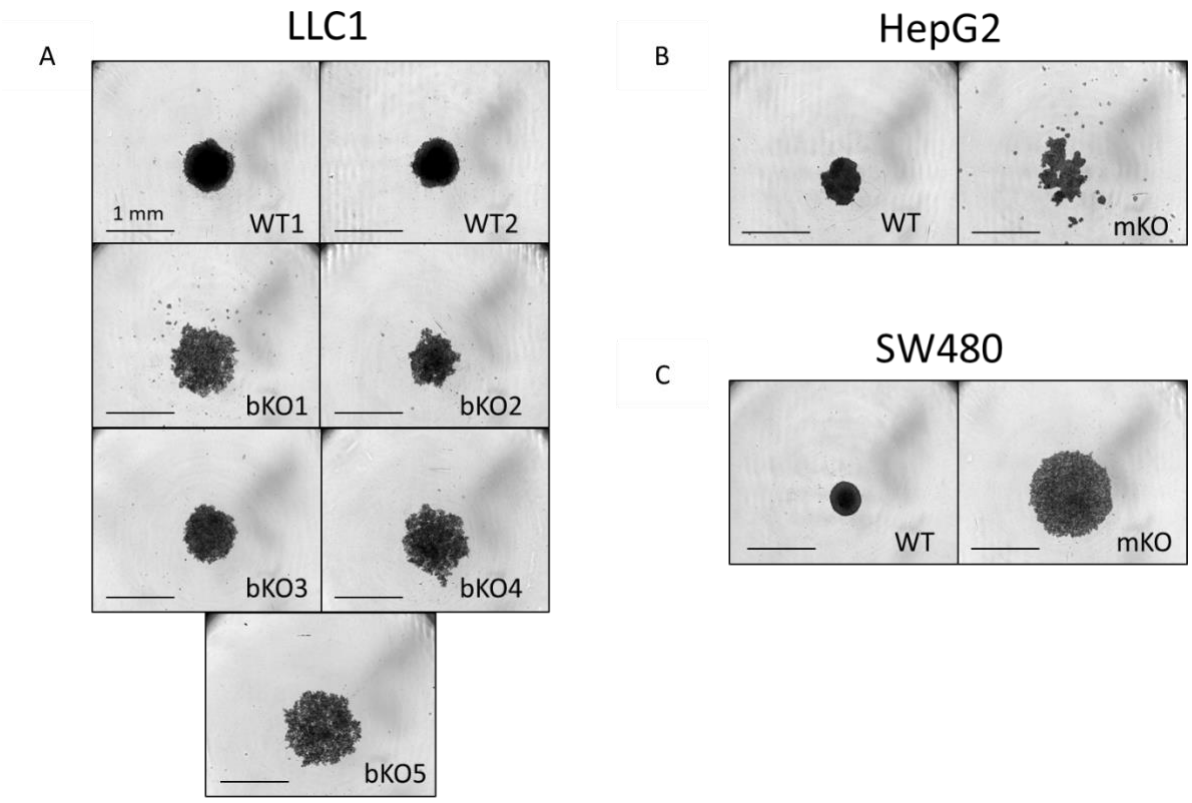

Figure 37. Comparison of spheroid images of wild-type and IMP2 knockout clones. (A) LLC1, (B) HepG2, and (C) SW480 clones were assessed for their spheroid forming ability using the live cell imaging system IncuCyte® S3 at the 6-day time point after cell seeding. Representative images were chosen and the scale = 1 mm. The HepG2 and SW480 IMP2 knockout cells were monoallelic knockouts.

The colony formation assay (CFA) was employed to understand the role of IMP2 in tumor growth. The LLC1 IMP2 biallelic knockout cells exhibited a significant decrease in both the number of colonies formed (**Figure 38A**) and the average area of the colonies (**Figure 38B**). While the wild-type cells formed colonies in the form of spheroids, the knockout clones lost this ability and displayed migration away from each other (**Figure 38C**). Furthermore, monoallelic IMP2 knockouts of Huh7, HepG2, and SW480 cells also exhibited a significant reduction in colony formation ability, as observed in terms of both colony number and area (**Figure 39**).

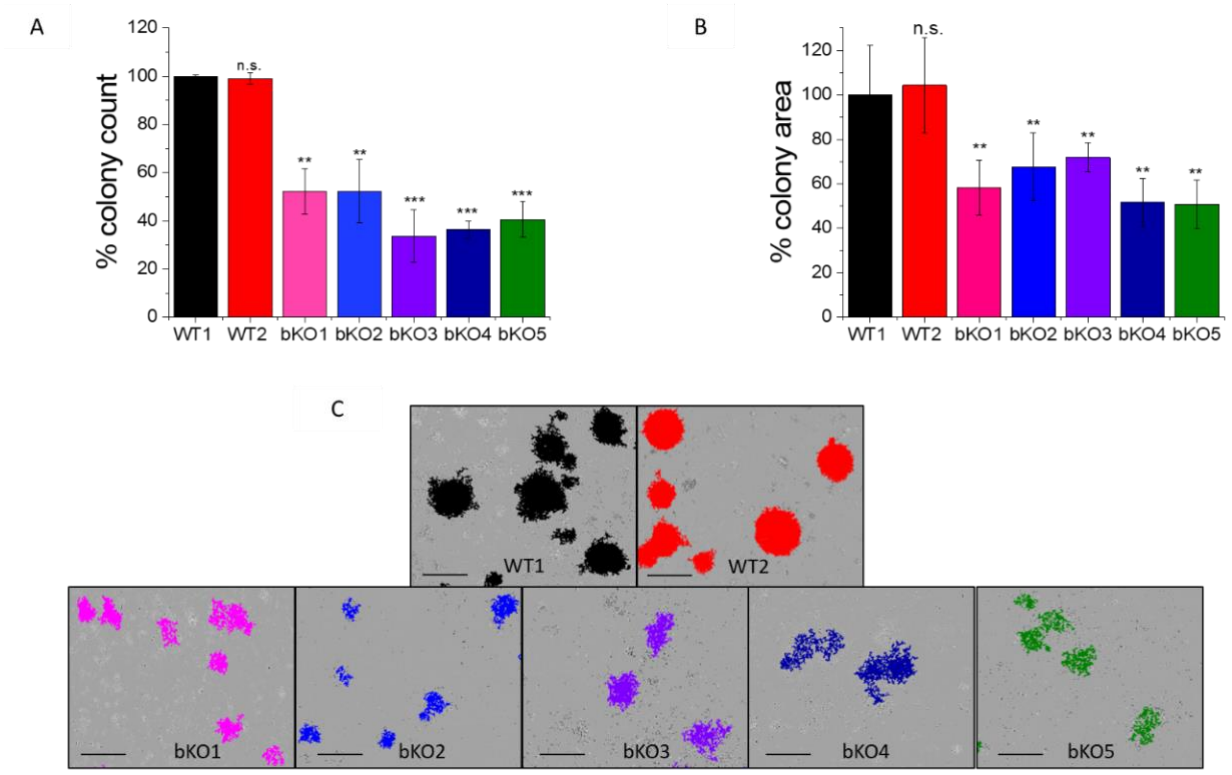

Figure 38. Effect of IMP2 knockout in LLC1 cells on the colony formation ability. The results are presented as follows: (A) number of colonies, (B) average area of colonies, and (C) representative images of colonies with the scale = 1 mm. Colony counting and measurement of the average area were performed using the IncuCyte® S3 live cell imaging system. It should be noted that WT1 represents the bulk LLC1 wild-type clone, while WT2 serves as the LLC1 editing control. Data were normalized to the WT1 cells and are represented as mean ± SEM, n= 4, triplicates. *p < 0.05, **p < 0.01, and ***p < 0.001 when compared to values of WT1 cells. n.s. indicates no significant difference.

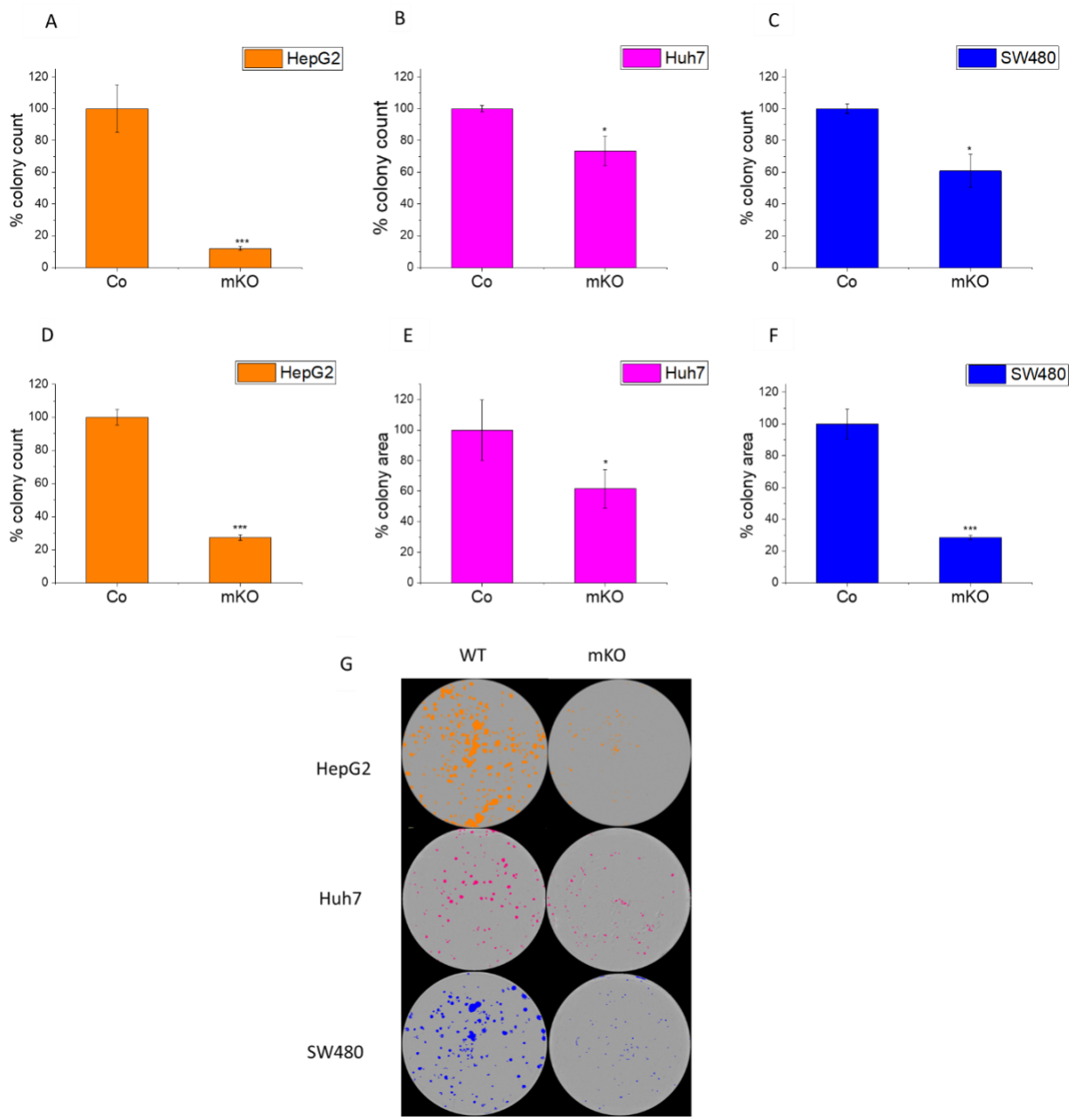

Figure 39. Effect of IMP2 knockout on colony formation ability of Huh7, HepG2, and SW480 cells. Figures illustrate the number of colonies for wild-type (WT) or monoallelic IMP2 knockout (mKO) (A) Huh7, (B) HepG2, and (C) SW480 cells, and the average area of colonies for (D) Huh7, (E) HepG2, and (F) SW480. (G) Representative images of colonies seen in a 6-well plate. The colonies were counted, and the average colony area was measured using the IncuCyte® S3 live cell imaging system. Huh7, HepG2, and SW480 were monoallelic IMP2 knockouts. Data were normalized to wild-type cells/control (Co) and represented as mean ± SEM, n=3, duplicates. *p < 0.05, **p < 0.01, and ***p < 0.001 when compared to values of control.

Furthermore, we investigated the impact of IMP2 inhibitor compounds # 4, 6, and 9, which had been identified by a screening approach (Dahlem, Abuhaliema, et al., 2022), on the 2D proliferation and metabolic activity of wild-type LLC1 cells. The compounds demonstrated a significant reduction in the proliferation rate at a concentration of 30 µM (**Figure 40A-C**), and

a dose-dependent decrease in the cells' metabolic activity as assessed by MTT assay, was observed at concentrations ranging from 5 µM to 100 µM (**Figure 41A-C**). The cells did not exhibit distinct morphological changes upon compound treatment (**Supplementary Figure 6B**).

To investigate the specificity of the compounds on IMP2 in terms of their effect on 2D proliferation (**Figure 40D-F**) and metabolic activity (**Figure 41D-F**), we compared their action on bulk WT1 and the editing control WT2 and the five biallelic IMP2 knockout LLC1 clones. Notably, the knockout clones bKO1-4 displayed a lower sensitivity to the treatments compared to wild-type LLC1 cells (WT1 and WT2). The bKO5 displayed a similar response to the wild-type LLC1 cells.

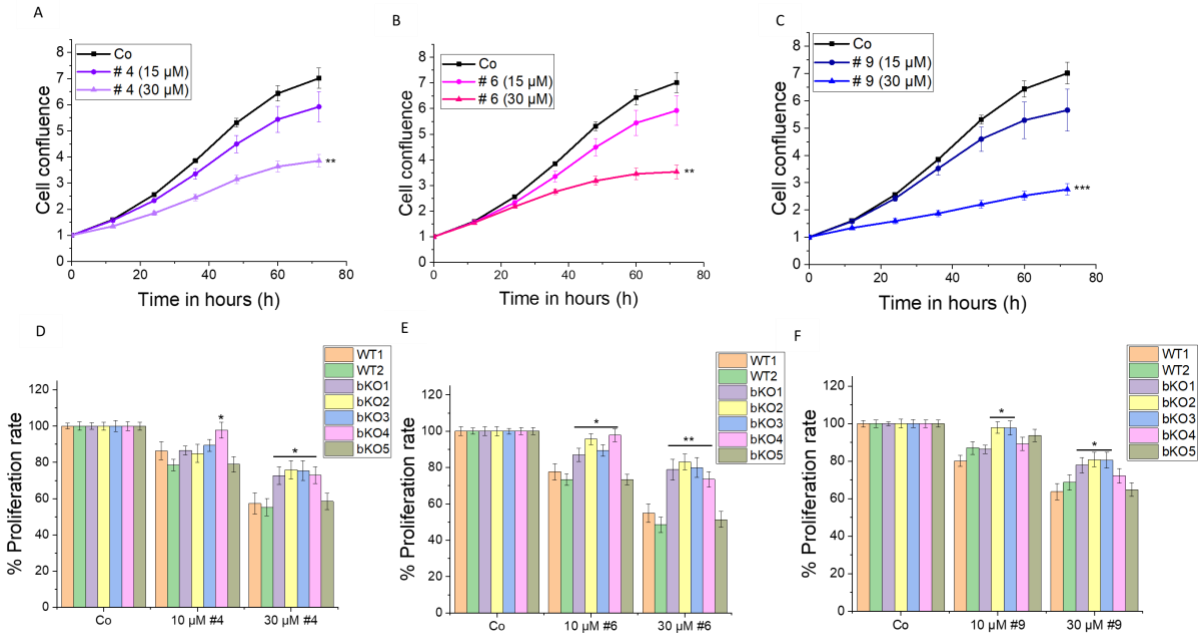

Figure 40. Effect of IMP2 inhibitors on the 2D cell proliferation of wild-type and biallelic IMP2 knockout LLC1 cells. The effects on 2D proliferation of LLC1 cells upon treatment with published IMP2 inhibitors, i.e., (A, D) compound 4, (B, E) compound 6, and (C, F) compound 9 at the indicated concentrations over 3 days were assessed using the IncuCyte® S3 live cell imaging system. The time point shown for wild-type and biallelic IMP2 knockout LLC1 clones is 72 h post-treatment. Data is normalized to time point 0 h of the respective control and represented as mean ± SEM, n=3, triplicates. *p < 0.05, **p < 0.01, and ***p < 0.001 compared to values of solvent control (Co) for graphs A-C and to the values of WT1 LLC1 cells for graphs D-F. The proliferation rate was determined based on the cell confluence.

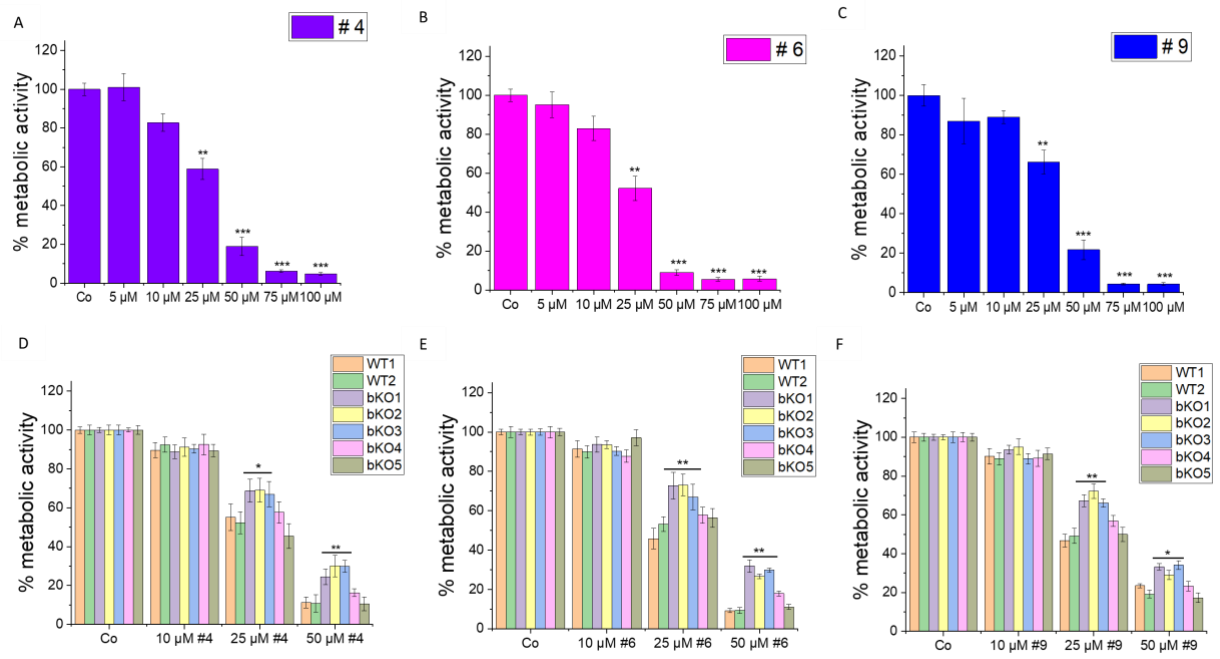

Figure 41. Effect of IMP2 inhibitors on the metabolic activity (MTT assay) of wild-type and biallelic IMP2 knockout LLC1 cells. The effects on the metabolic activity of LLC1 cells upon treatment with published IMP2 inhibitors, i.e., (A, D) compound 4, (B, E) compound 6, and (C, F) compound 9 at the indicated concentrations after 3 days were assessed by MTT assay. Data are normalized to solvent controls (Co) and represented as mean ± SEM, n=3, triplicates. *p < 0.05, **p < 0.01, and ***p < 0.001 compared to values of solvent control (Co) for graphs A-C and to the values of WT1 LLC1 cells for graphs D-F.

Based on the IC_{50} of the compounds obtained in LLC1 cells, a treatment concentration of 25 µM was chosen for our study of their effect on colony formation (**Table 9**). For HepG2, Huh7, and SW480, the previously published IC_{50} values of the three compounds were selected for the treatment (Dahlem, Abuhaliema, et al., 2022). In all tested cell lines, all three compounds exhibited a significant reduction in both the number and average size of the formed colonies. These findings provide further evidence of the essential role of IMP2 in colony formation ability (**Figure 42, 43**).

Table 9. IC_{50} of IMP2 inhibitors in wild-type LLC1 cells

Compound (#)	***IC*$_{50}$**
4	25.23 µM
6	23.90 µM
9	28.45 µM

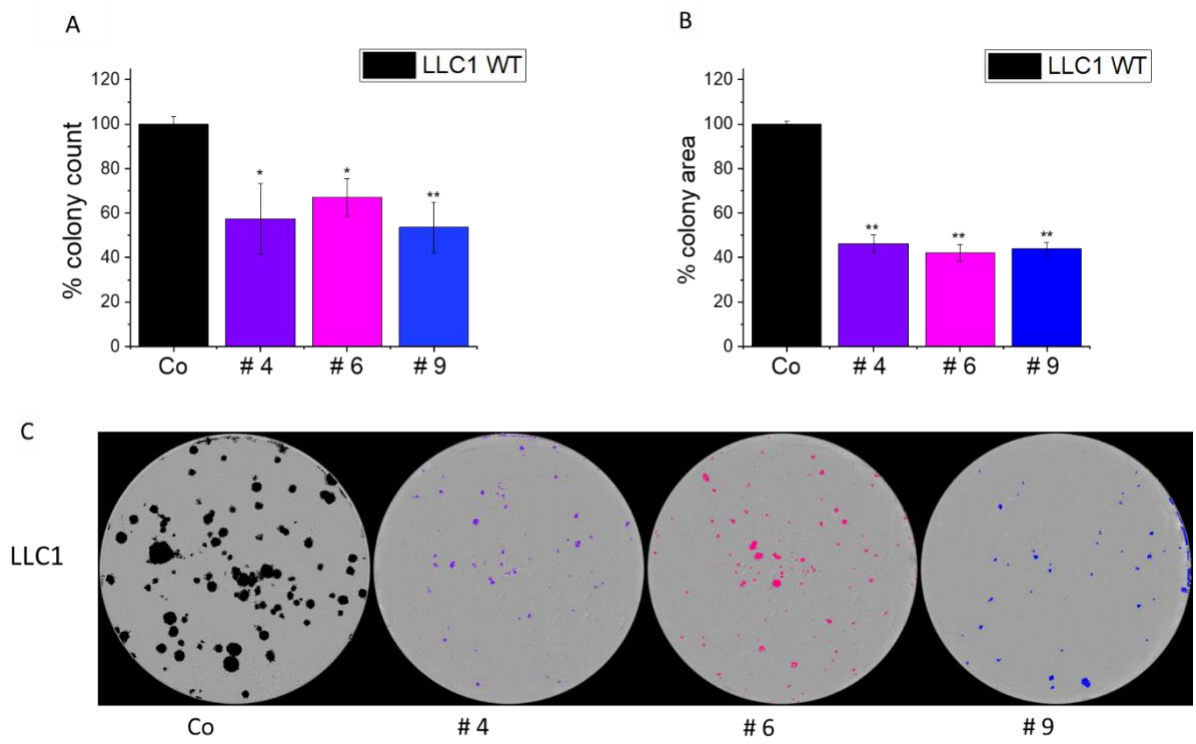

Figure 42. Effect of IMP2 inhibitors on wild-type LLC1 cells in colony formation assay. Figures illustrate the (A) number of colonies, (B) average area of colonies, and (C) representative images of colonies seen in a 6-well plate. Colonies were counted and the average area of colonies was determined using the IncuCyte® S3 live cell imaging system. A treatment concentration of 25 µM was applied for each compound. Data were normalized to untreated wild-type LLC1 cells/control (co) and represented as mean ± SEM, n=3, duplicates. *$p < 0.05$, **$p < 0.01$, and ***$p < 0.001$ compared to values of solvent control cells.

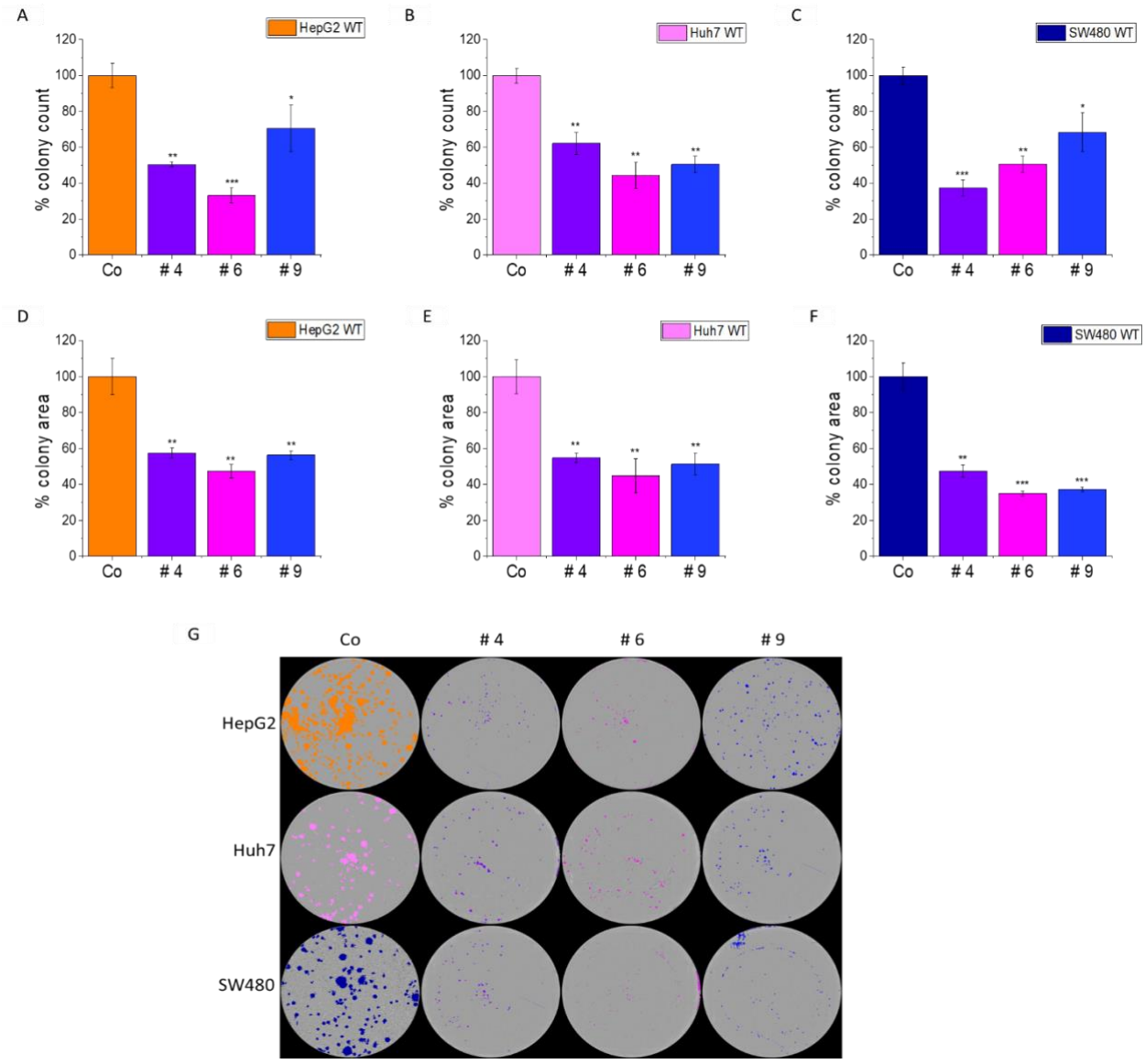

Figure 43. Effect of IMP2 inhibitors on Huh7, HepG2, and SW480 cells in colony formation assays. Results present the number of colonies for (A) Huh7, (B) HepG2, and (C) SW480, as well as the average area of colonies for (D) Huh7, (E) HepG2, and (F) SW480 cells. Additionally, (G) representative images of colonies are shown as seen in a 6-well plate. The colonies were counted, and the average colony area was determined using the live cell imaging system, IncuCyte® S3. The Huh7, HepG2, and SW480 were monoallelic IMP2 knockouts. Data were normalized to untreated wild-type cells and represented as mean ± SEM, n=2, triplicates. The treatment doses were as follows: For Huh7, comp 4- 35 µM, comp 6- 45 µM, and comp 9- 25 µM. For HepG2, comp 4- 30 µM, comp 6- 40 µM, and comp 9- 35 µM. For SW480, comp 4- 20 µM, comp 6- 50 µM, and comp 9- 35 µM. *$p < 0.05$, **$p < 0.01$, and ***$p < 0.001$ compared to values of respective wild-type (WT)/solvent control (Co) cells.

The effect of IMP2 knockout on cell migration was investigated (**Figure 44**). The IMP2 biallelic LLC1 knockout cells did not display any significant difference in cell migration ability compared to the wild-type cells, except for the clone bKO1, which exhibited a significant increase in cell migration. However, this notable increase could be attributed to a clonal artifact. A significant difference in cell migration was observed in the monoallelic IMP2 knockout HepG2 cells at early time points (8 h and 16 h). In addition, the Huh7 IMP2 monoallelic knockout cells showed an overall reduced cell migration after the 16 h time point, in comparison to the wild-type cells. The monoallelic IMP2 knockout SW480 cells showed a significant reduction in the cells' migratory ability at all time points tested.

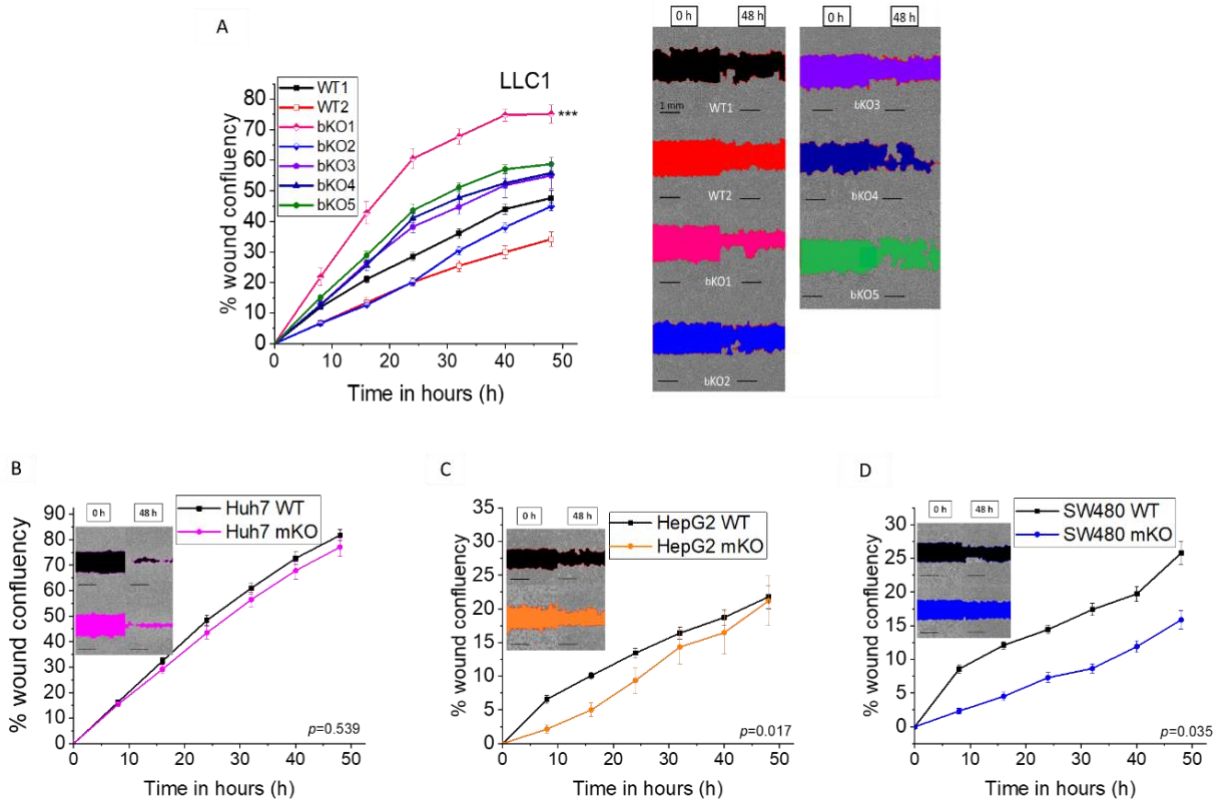

Figure 44. Effect of IMP2 knockout on cell migration. (A) LLC1 (B) Huh7, (C) HepG2, and (D) SW480 cells were analyzed for cell migration using the IncuCyte® S3 system over a 48 h period. Representative pictures show the wound area in color at the starting point, 0 h, and 48 h after wounding, and the scale = 1 mm. The LLC1 wild-type clone is referred to as WT1, and the LLC1 editing control is referred to as WT2. The Huh7, HepG2, and SW480 were monoallelic IMP2 knockouts. Data are normalized to time point 0 h. Data is represented as mean ± SEM, n=3, (quintuplicates). *p < 0.05, **p < 0.01, and ***p < 0.001 compared to values of WT1/control cells for LLC1 data. The *p*-value indicates a significant difference between the earlier time points (8 h and 16 h) for HepG2 wild-type and monoallelic knockout cells. However, for Huh7 and SW480 cells, significant differences were compared between the wild-type and monoallelic knockout cells for all time points.

5.2.3 Discussion

Overexpression of *IGF2BP2* has been reported in several cancers, highlighting its prognostic role (Dai et al., 2017). Previous studies have characterized the role of IMP2 as a tumor promoter in cancer through siRNA-mediated knockdown of *IGF2BP2* (Cao et al., 2023; Cui et al., 2021; Dong et al., 2021; Xu et al., 2019) Our study aimed to generate IMP2 knockouts using CRISPR/Cas9-prime editing approaches to validate IMP2 as a potential anticancer target.

One of the hallmarks of cancer is genomic instability (Hanahan, 2022). As a result, cancer cells typically exhibit aneuploidy and karyotypic abnormalities. Due to these factors, care has been taken to select hypotriploid cells for generating knockout clones using CRISPR/Cas9, thereby maximizing the chances of achieving a complete knockout.

The biallelic AAVS1 knockout HCT116 clone was generated to serve as a negative control for prime editing and exhibited behavior identical to that of wild-type cells when analyzed for proliferation in the 2D and 3D cell culture models. These results align with the expected outcome, as editing within a safe harbor locus (SHL) should not induce any functional changes in characteristics (Papapetrou & Schambach, 2016); instead, it should behave similarly to the wild-type clone. The biallelic knockout of IMP2 in HCT116 cells resulted in reduced proliferation in both the 2D and 3D cultures, accompanied by the formation of smaller spheroids. This further emphasizes the role of IMP2 in cell proliferation (Dahlem, Abuhaliema, et al., 2022).

Attempts to achieve Rosa26 knockout using prime editing were unsuccessful in murine (LLC1) cell lines. Our findings are consistent with previous observations that the prime editor 2 (PE2) system is challenging to use in the murine system (Aida et al., 2020). Strategies that aim to reduce the size of the PE2 system have been proposed to improve the efficiency of prime editing (Böck et al., 2022; Liu et al., 2021; Zheng et al., 2022).

Previous research has used CRISPR/Cas9 to inactivate IMP2 and observed a decrease in the 2D proliferation in various cell lines, including Hep3b, HeLa, RD, HCC-1359, MB-231, and SNU-423, over 5 days. This was determined by assessing growth and cell numbers using a mixture of edited and non-edited cells (Dai et al., 2017). These findings support our hypothesis that obtaining a single cell-derived IMP2 knockout is challenging in cancer cell lines, and thus earlier studies have rather used a polyclonal mixture for analysis, which potentially only had a monoallelic gene deletion. In our study, we encountered difficulties in generating single-cell derived IMP2 biallelic knockouts in SW480, HepG2, Huh7, and A549 cell lines using CRISPR/Cas9-prime editing approach, despite employing previously validated pegRNA constructs (Dahlem, Abuhaliema, et al., 2022) and recently validated gRNAs used in the CRISPR/Cas9 system. This suggests that the absence of IMP2 may impair the ability of cells to form colonies and affect cancer cell proliferation.

Using our CRISPR/Cas9 approach, we successfully generated biallelic IMP2 knockouts in LLC1 cells. Sanger sequencing confirmed that biallelic IMP2 knockout LLC1 cells exhibited reduced protein expression, ranging from 7% to 65%. Despite several attempts, we could not generate biallelic IMP2 knockouts in SW480, Huh7, and HepG2 cells, supporting the notion that IMP2 is crucial for cell proliferation (Dahlem, Abuhaliema, et al., 2022). These monoallelic IMP2 knockouts, verified by Sanger sequencing, also demonstrated protein expression levels of 40% to 80%, as previously reported (Dahlem, Abuhaliema, et al., 2022). While successful editing disrupted gene integrity in the IMP2 knockout clones, the genomic effects did not consistently result in reduced RNA levels or explain the protein abundance in the CRISPR-generated knockout cell lines (Smits et al., 2019).

The target specificity of IMP2 in biallelic IMP2 knockout HCT116 cells was examined through rescue experiments, focusing on its impact on various potential IMP2 targets. Notably, a decrease in the expression of *DANCR* and *MYC* was observed. However, this reduction was partially reversed when they were overexpressed along with *IMP2/p62*. Given that IMP2 influences a multitude of mRNAs via diverse mechanisms such as controlling their stability, localization, or translation (Cao et al., 2018), it is unrealistic to expect a single target to explain all of IMP2's actions.

Three IMP2 inhibitor compounds were tested in both the 2D and 3D models, resulting in reduced expression of *DANCR*, *MYC*, and *HMGA1*. These findings further substantiate the inhibitory effects of the compounds on IMP2 (Dahlem, Abuhaliema, et al., 2022). Notably, the compounds' anti-proliferative impact was primarily pronounced in the 3D models, suggesting variances in gene expression between knockout cells and differences between the 2D and 3D cell cultures, as observed for *HMGA1*. It's also plausible that other pathways contribute to the expression of the three IMP2 mRNA targets. These findings offer insights into the cellular distinctions between HCT116 and SW480 cells, as well as the observed increase in *HMGA1* following treatment with compound 6 in SW480 cells, which might be a secondary effect. Overall, the reduced expression of the tumor-promoting IMP2 targets *DANCR*, *MYC*, and *HMGA1* upon compound treatment, coupled with the discernible effects seen in parental and IMP2 knockout cells, underscores the compounds' on-target mode of action.

Other studies have investigated the impact of IMP2 knockdown using siRNA/shRNA-mediated approaches on colorectal carcinoma (CRC) cell lines. IMP2 knockdown exhibited reduced colony formation ability in HCT116 and SW480 (Liu et al., 2023), and in SW620 and SW480 cells (Ye et al., 2016b). Similarly, IMP2 knockdown in SW480, SW620, and HCT-8 cells led to the inhibition of the 2D cell proliferation and reduced migration (Cui et al., 2021). Our recent study focused on CRISPR/Cas9-prime mediated biallelic IMP2 knockout in HCT116 cells, which showed no effect on the 2D proliferation but demonstrated reduced 3D proliferation, cell migration, and adhesion (Dahlem, Abuhaliema, et al., 2022). Recent research revealed that IMP2 is involved in the induction of chemoresistance in HCT116 (Kendzia et al., 2023). Our

data exhibited reduced proliferation at later time points, as well as decreased cell migration in CRISPR/Cas9-generated monoallelic IMP2 knockout SW480 cells.

Likewise, studies on hepatocellular carcinoma (HCC) cells have also demonstrated the impact of shRNA-mediated IMP2 knockdown. In HepG2 and Huh7 cells, IMP2 knockdown impeded cell proliferation and reduced clonogenicity (Pu et al., 2020). Employing the siRNA knockdown of p62, HepG2 cells showed no effect on the 2D cell proliferation (Kessler et al., 2013). CRISPR/Cas9-mediated IMP2 knockout in HepG2 and SNU449 cells, in a polyclonal mixture of transfected cells, showed inconsistent effects on cell proliferation, but reduced colony formation upon IMP2 inactivation (Xing et al., 2020). Additionally, IMP2 inactivation in HepG2 cells reduced cell migration, while IMP2 overexpression in SNU449 cells promoted migration through epithelial-mesenchymal transition (EMT) induction *via* the Wnt/β-catenin pathway (Xing et al., 2020). Tumor cells gain their migratory and invasive ability through EMT, eventually aiding in metastasis (Dahlem et al., 2019). Similar effects on EMT induction were observed upon IMP2 overexpression in PANC-1 cells (pancreatic cancer) (Dahlem et al., 2019) and glioblastoma multiforme (malignant brain cancer) (Mu et al., 2015). Our data on IMP2 knockout HCC cells showed a tendency of reduced cell migratory ability, likely due to the monoallelic editing that still allows IMP2 expression. Nevertheless, the findings emphasize that IMP2 knockout results in reduced cell migratory ability, probably by hindering EMT. Moreover, our study confirmed reduced 2D proliferation in HepG2 IMP2 monoallelic knockout cells and clonogenicity in monoallelic IMP2 knockout HepG2 and Huh7 cells. The lack of effect observed on the 2D proliferation in Huh7 monoallelic IMP2 knockout could be attributed to the fact that the knockout clone still expresses nearly 80% of IMP2.

In non-small cell lung cancer cell lines A549 and H1975, sh-RNA-mediated IMP2 knockdown resulted in reduced proliferation and colony formation ability (Han et al., 2022). Our data showed no effect on the 2D proliferation but reduced colony formation in LLC1 biallelic IMP2 knockouts. Our data showed no consistent effect on 2D proliferation but reduced colony formation in LLC1 biallelic IMP2 knockouts. In a study by Xu et al., 2022, it was demonstrated that single-cell-derived cell lines (SCDCLs) from LLC1 cells display varying growth patterns. This discovery can help shed light on our findings regarding the proliferation of LLC1 cells. Specifically, our data indicate that bulk LLC1 cells (designated as WT1) exhibit slower growth than WT2, which have been derived from cells that underwent the CRISPR procedure without an edit of the IMP2 gene. Compared to this WT2 clone, four of the knockout clones were growing slower (bKO1-4), while bKO5 grew faster. With the action of IMP2 inhibitors on cell proliferation reduced in four of the five knockout clones, this further supports the involvement of IMP2 in cell proliferation, but it is challenging to establish a clear trend due to the heterogeneous nature of the SCDCLs.

The 3D culture models provide valuable insights into tumor characteristics, such as proliferation, invasion, and metastatic potential (Han et al., 2021). The formation of MCTs relies on cell-cell adhesion molecules that initiate loose bonds between integrins and the

extracellular matrix (ECM). The interaction through N-cadherin-to-E-cadherin plays a crucial role in the aggregation of cells into compact spheroids (Han et al., 2021). Previous studies have demonstrated a loss of spheroid-forming ability in colon cancer cells (Stadler et al., 2018). In our study, we investigated the effect of IMP2 knockout on the ability of HCC, CRC, and lung cancer cells to form spheroids. The knockout of IMP2 in all tested cell lines resulted in a loss of their ability to form compact spheroids. This can be attributed to the reduction in cell adhesion, as previously shown in biallelic edited IMP2 knockout HCT116 cells (Dahlem, Abuhaliema, et al., 2022). The role of IMP2 in spheroid formation in cancer has not been extensively studied before.

Previously, the effects of the three IMP2 inhibitors on the 2D cell proliferation in HCT116 and Huh7 cells and the 3D cell proliferation in HCT116 and SW480 cells were studied (Dahlem, Abuhaliema, et al., 2022). These inhibitors showed inhibition of both the 2D and 3D proliferation, which aligns with our findings of reduced 2D proliferation in LLC1 cells upon compound treatment. It is important to note that while the inhibition is not entirely specific to IMP2, the fact that the effect is more pronounced in wild-type cells compared to IMP2 knockout clones suggests a significant reliance on IMP2 inhibition (Dahlem, Abuhaliema, et al., 2022). In this work, novel findings are presented indicating that these compounds also exert an effect on a mouse cancer cell line, that is LLC1. Interestingly, we observed a reduced sensitivity towards these compounds in biallelic IMP2 knockout LLC1 cells when compared to their parental cell lines. It is worth mentioning that these compounds represent hits, which were identified through a screening approach (Dahlem, Abuhaliema, et al., 2022) and have not been optimized for targeting IMP2 specifically. Nevertheless, the level of specificity we observed is quite noteworthy. Additionally, we observed reduced colony formation ability in LLC1, SW480, HepG2, and Huh7 cells following compound treatment.

Summary and conclusion

This study employed two distinct strategies to explore novel therapeutic approaches for cancer treatment. One strategy involved characterizing a natural compound, violacein as a potential anticancer agent, while the second focused on validating RNA-binding proteins as prospective targets in cancer therapy.

Violacein demonstrated cytotoxic and anti-proliferative ability in colon, liver, and pancreatic cancer cells. Furthermore, it showed potential in inducing immunogenic cell death through NFκB reporter cell activation.

Monoallelic HuR knockout MDAMB-231 clones did not impact 2D cell proliferation. Notably, potential HuR inhibitors, EC and NovNa, did not exhibit significant anti-proliferative effects on the tested tumor cell lines at low to moderate concentrations, underscoring the necessity for more potent inhibitors.

CRISPR/Cas9-prime editing was utilized to generate IMP2 knockouts in colon, lung, and hepatocellular cancer cell lines. This approach highlighted the significant role of IMP2 in various cancer hallmarks. Within this study, a decrease in gene expression levels of potential IMP2 targets, *DANCR* and *MYC*, was observed in biallelic IMP2 knockout HCT116 cells. Notably, their expression was restored upon rescue/overexpression of IMP2. Treatment with small molecule IMP2 inhibitors led to reduced expression of tumor-promoting IMP2 targets *DANCR*, *MYC*, and *HMGA1*. This effect was accompanied by discernible changes in both wild-type and IMP2 knockout cells, underscoring the on-target mode of action of the compounds.

Despite multiple attempts, generating IMP2 biallelic knockouts in A549 and Huh7 cells proved unsuccessful. Next-generation sequencing results confirmed efficient editing by both sgRNAs used in the plasmid-based CRISPR/Cas9 approach. However, edited cells lost their proliferative capacity.

Monoallelic knockout cell lines of IMP2 exhibited reduction in 2D cell proliferation. In 3D cultures, IMP2 knockouts displayed a change in morphology from compact spheroids to loose aggregates. Moreover, there was a notable decrease in colony formation ability and cell migration among the IMP2 knockouts. This effect was mirrored by IMP2 inhibitor compounds, which also hindered 2D cell proliferation and colony formation. In this thesis, we showed for the first time that the compounds exert an effect on a mouse cancer cell line, that is LLC1. Interestingly, we observed a reduced sensitivity towards these compounds in biallelic IMP2 knockout LLC1 cells when compared to their parental cell lines confirming their significant reliance on IMP2. Overall, *in vitro* target validation underscores the essential role of IMP2 in tumor cell proliferation, colony formation, and migration across various cancer types.

References

Aggarwal, V., Tuli, H. S., Varol, A., Thakral, F., Yerer, M. B., Sak, K., Varol, M., Jain, A., Khan, M. A., & Sethi, G. (2019). Role of Reactive Oxygen Species in Cancer Progression: Molecular Mechanisms and Recent Advancements. *Biomolecules*, *9*(11), 735.

Aida, T., Wilde, J. J., Yang, L., Hou, Y., Li, M., Xu, D., Lin, J., Qi, P., Lu, Z., & Feng, G. (2020). Prime editing primarily induces undesired outcomes in mice. *BioRxiv*. 2020-08.

Alberts, B., Johnson, A., Lewis, J., Raff, M., Roberts, K., & Walter, P. (2002). Cancer as a Microevolutionary Process. *Molecular Biology of the Cell*. 4th edition. Garland Science.

Ali, J. A., Jackson, A. P., Howells, A. J., & Maxwell, A. (1993). The 43-Kilodalton N-Terminal Fragment of the DNA Gyrase B Protein Hydrolyzes ATP and Binds Coumarin Drugs. *Biochemistry*, *32*(10), 2717–2724.

Alshatwi, A. A., Subash-Babu, P., & Antonisamy, P. (2016). Violacein induces apoptosis in human breast cancer cells through up regulation of BAX, p53 and down regulation of MDM2. *Experimental and Toxicologic Pathology*, *68*(1), 89–97.

Anthon, C., Corsi, G. I., & Gorodkin, J. (2022). CRISPRon/off: CRISPR/Cas9 on- and off-target gRNA design. *Bioinformatics*, *38*(24), 5437.

Anzalone, A. V., Randolph, P. B., Davis, J. R., Sousa, A. A., Koblan, L. W., Levy, J. M., Chen, P. J., Wilson, C., Newby, G. A., Raguram, A., & Liu, D. R. (2019). Search-and-replace genome editing without double-strand breaks or donor DNA. *Nature*, *576*(7785), 149–157.

Barghash, A., Golob-Schwarzl, N., Helms, V., Haybaeck, J., & Kessler, S. M. (2016). Elevated expression of the IGF2 mRNA binding protein 2 (IGF2BP2/IMP2) is linked to short survival and metastasis in esophageal adenocarcinoma. *Oncotarget*, *7*(31), 49743.

Barghash, A., Helms, V., & Kessler, S. M. (2015). Overexpression of IGF2 mRNA-Binding Protein 2 (IMP2/p62) as a Feature of Basal-like Breast Cancer Correlates with Short Survival. *Scandinavian Journal of Immunology*, *82*(2), 142–143.

Bigagli, E., De Filippo, C., Castagnini, C., Toti, S., Acquadro, F., Giudici, F., Fazi, M., Dolara, P., Messerini, L., Tonelli, F., & Luceri, C. (2016). DNA copy number alterations, gene expression changes and disease-free survival in patients with colorectal cancer: a 10 year follow-up. *Cellular Oncology (Dordrecht)*, *39*(6), 545–558.

Blanco, F. F., Preet, R., Aguado, A., Vishwakarma, V., Stevens, L. E., Vyas, A., Padhye, S., Xu, L., Weir, S. J., Anant, S., Meisner-Kober, N., Brody, J. R., & Dixon, D. A. (2016). Impact of HuR inhibition by the small molecule MS-444 on colorectal cancer cell tumorigenesis. *Oncotarget*, *7*(45), 74043.

Böck, D., Rothgangl, T., Villiger, L., Schmidheini, L., Matsushita, M., Mathis, N., Ioannidi, E., Rimann, N., Grisch-Chan, H. M., Kreutzer, S., Kontarakis, Z., Kopf, M., Thöny, B., & Schwank, G. (2022). *In vivo* prime editing of a metabolic liver disease in mice. *Science Translational Medicine*, *14*(636), 9238.

Boettcher, M., & Mcmanus, M. T. (2015). Molecular Cell Choosing the Right Tool for the Job: RNAi, TALEN, or CRISPR. *Molecular Cell*, *58*(4), 575-585.

Bolognani, F., Gallani, A. I., Sokol, L., Baskin, D. S., & Meisner-Kober, N. (2012). mRNA stability alterations mediated by HuR are necessary to sustain the fast growth of glioma cells. *Journal of Neuro-Oncology*, *106*(3), 531–542.

Burlison, J. A., Avila, C., Vielhauer, G., Lubbers, D. J., Holzbeierlein, J., & Blagg, B. S. J. (2008). Development of novobiocin analogues that manifest anti-proliferative activity against several cancer cell lines. *Journal of Organic Chemistry*, *73*(6), 2130–2137.

Cao, J., Mu, Q., & Huang, H. (2018). The Roles of Insulin-Like Growth Factor 2 mRNA-Binding Protein 2 in Cancer and Cancer Stem Cells. *Stem Cells International*, 2018.

Cao, P., Wu, Y., Sun, D., Zhang, W., Qiu, J., Tang, Z., Xue, X., & Qin, L. (2023). IGF2BP2 promotes pancreatic carcinoma progression by enhancing the stability of B3GNT6 mRNA via m6A methylation. *Cancer Medicine*, *12*(4), 4405–4420.

Cen, Y., Chen, L., Liu, Z., Lin, Q., Fang, X., Yao, H., & Gong, C. (2023). Novel roles of RNA-binding proteins in drug resistance of breast cancer: from molecular biology to targeting therapeutics. *Cell Death Discovery*, 9(1), 52.

Christiansen, J., Kolte, A. M., Hansen, T. V. O., & Nielsen, F. C. (2009). IGF2 mRNA-binding protein 2: biological function and putative role in type 2 diabetes. *Journal of Molecular Endocrinology*, *43*(5), 187–195.

Clement, K., Rees, H., Canver, M. C., Gehrke, J. M., Farouni, R., Hsu, J. Y., Cole, M. A., Liu, D. R., Joung, J. K., Bauer, D. E., & Pinello, L. (2019). CRISPResso2 provides accurate and rapid genome editing sequence analysis. *Nature Biotechnology*, *37*(3), 224–226.

Costantino, C. L., Witkiewicz, A. K., Kuwano, Y., Cozzitorto, J. A., Kennedy, E. P., Dasgupta, A., Keen, J. C., Yeo, C. J., Gorospe, M., & Brody, J. R. (2009). The role of HuR in gemcitabine efficacy in pancreatic cancer: HuR Up-regulates the expression of the gemcitabine metabolizing enzyme deoxycytidine kinase. *Cancer Research*, *69*(11), 4567–4572.

Cui, J., Tian, J., Wang, W., He, T., Li, Xin, Chenzheng Gu, Wang, L., Wu, J., & Shang, A. (2021) IGF2BP2 promotes the progression of colorectal cancer through a YAP-dependent mechanism. *Cancer Science*, *112*, 4087–4099.

Czepukojc, B., Abuhaliema, A., Barghash, A., Tierling, S., Naß, N., Simon, Y., Körbel, C., Cadenas, C., van Hul, N., Sachinidis, A., Hengstler, J. G., Helms, V., Laschke, M. W., Walter, J., Haybaeck, J., Leclercq, I., Kiemer, A. K., & Kessler, S. M. (2019). IGF2 mRNA Binding Protein 2 Transgenic Mice Are More Prone to Develop a Ductular Reaction and to Progress Toward Cirrhosis. *Frontiers in Medicine*, *6*, 179.

D'Agostino, V. G., Lal, P., Mantelli, B., Tiedje, C., Zucal, C., Thongon, N., Gaestel, M., Latorre, E., Marinelli, L., Seneci, P., Amadio, M., & Provenzani, A. (2015). Dihydrotanshinone-I interferes with the RNA-binding activity of HuR affecting its post-transcriptional function. *Scientific Reports*, *5*(1), 16478.

Dahlem, C., Abuhaliema, A., Kessler, S. M., Kröhler, T., Zoller, B. G. E., Chanda, S., Wu, Y., Both, S., Müller, F., Lepikhov, K., Kirsch, S. H., Laggai, S., Müller, R., Empting, M., & Kiemer, A. K. (2022). First Small-Molecule Inhibitors Targeting the RNA-Binding Protein IGF2BP2/IMP2 for Cancer Therapy. *ACS Chemical Biology*, *17*(2), 361–375.

Dahlem, C., Barghash, A., Puchas, P., Haybaeck, J., & Kessler, S. M. (2019). The Insulin-Like Growth Factor 2 mRNA Binding Protein IMP2/IGF2BP2 is Overexpressed and Correlates with Poor Survival in Pancreatic Cancer. *International Journal of Molecular Sciences*, *20*(13), 3204.

Dahlem, C., Chanda, S., Hemmer, J., Schymik, H. S., Kohlstedt, M., Wittmann, C., & Kiemer, A. K. (2022). Characterization of Anti-Cancer Activities of Violacein: Actions on Tumor Cells and the Tumor Microenvironment. *Frontiers in Oncology*, *12*, 2026.

Dahlem, C. (2020). *In vitro* and *in vivo* characterization of therapeutic approaches for solid tumors :natural compounds and novel targets. Dissertation zur Erlangung des Grades des Doktors der Naturwissenschaften der Naturwissenschaftlich-Technischen Fakultät der Universität des Saarlandes.

Dai, N. (2020). The Diverse Functions of IMP2/IGF2BP2 in Metabolism. *Trends in Endocrinology and Metabolism*, *31*(9), 670–679.

Dai, N., Ji, F., Wright, J., Minichiello, L., Sadreyev, R., & Avruch, J. (2017). IGF2 mRNA binding protein-2 is a tumor promoter that drives cancer proliferation through its client mRNAs IGF2 and HMGA1. *Elife*, 6, e27155.

de Carvalho, D. D., Costa, F. T. M., Duran, N., & Haun, M. (2006). Cytotoxic activity of violacein in human colon cancer cells. *Toxicology in Vitro*, *20*(8), 1514–1521.

De Ravin, S. S., Reik, A., Liu, P. Q., Li, L., Wu, X., Su, L., Raley, C., Theobald, N., Choi, U., Song, A. H., Chan, A., Pearl, J. R., Paschon, D. E., Lee, J., Newcombe, H., Koontz, S., Sweeney, C., Shivak, D. A., Zarember, K. A., … Malech, H. L. (2016). Targeted gene addition in human CD34+ hematopoietic cells for correction of X-linked chronic granulomatous disease. *Nature Biotechnology*, *34*(4), 424–429.

Dehairs, J., Talebi, A., Cherifi, Y., & Swinnen, J. V. (2016). CRISP-ID: decoding CRISPR mediated indels by Sanger sequencing. *Scientific Reports*, *6*(1), 28973.

Deng, X., Jiang, Q., Liu, Z., & Chen, W. (2020). Clinical Significance of an m6A Reader Gene, IGF2BP2, in Head and Neck Squamous Cell Carcinoma. *Frontiers in Molecular Biosciences*, *7*, 68.

Denkert, C., Koch, I., Von Keyserlingk, N., Noske, A., Niesporek, S., Dietel, M., & Weichert, W. (2006). Expression of the ELAV-like protein HuR in human colon cancer: association with tumor stage and cyclooxygenase-2. *Modern Pathology*, *19*(9), 1261–1269.

Denkert, C., Weichert, W., Winzer, K. J., Müller, B. M., Noske, A., Niesporek, S., Kristiansen, G., Guski, H., Dietel, M., & Hauptmann, S. (2004). Expression of the ELAV-like protein HuR is associated with higher tumor grade and increased cyclooxygenase-2 expression in human breast carcinoma. *Clinical Cancer Research : An Official Journal of the American Association for Cancer Research*, *10*(16), 5580–5586.

Dharmaraja, A. T. (2017). Role of reactive oxygen species (ROS) in therapeutics and drug resistance in cancer and bacteria. *Journal of Medicinal Chemistry*, *60*(8), 3221-3240.

Diez, B., Genovese, P., Roman-Rodriguez, F. J., Alvarez, L., Schiroli, G., Ugalde, L., Rodriguez-Perales, S., Sevilla, J., Heredia, C. D. de, Holmes, M. C., Lombardo, A., Naldini, L., Bueren, J. A., & Rio, P. (2017). Therapeutic gene editing in CD34+ hematopoietic progenitors from Fanconi anemia patients. *EMBO Molecular Medicine*, *9*(11), 1574–1588.

Dlugosz, A., & Janecka, A. (2017). Novobiocin Analogs as Potential Anticancer Agents. *Mini Reviews in Medicinal Chemistry*, *17*(9), 728–733.

Doench, J. G. (2017). Am I ready for CRISPR? A user's guide to genetic screens. *Nature Reviews Genetics*, *19*(2), 67–80.

Dong, L., Geng, Z., Liu, Z., Tao, M., Pan, M., & Lu, X. (2021). IGF2BP2 knockdown suppresses thyroid cancer progression by reducing the expression of long non-coding RNA HAGLR. *Pathology - Research and Practice*, *225*, 153550.

Donnelly, A. C., Mays, J. R., Burlison, J. A., Nelson, J. T., Vielhauer, G., Holzbeierlein, J., & Blagg, B. S. J. (2008). The Design, Synthesis and Evaluation of Coumarin Ring Derivatives of the Novobiocin Scaffold that Exhibit Anti-proliferative Activity. *The Journal of Organic Chemistry*, *73*(22), 8901.

Durán, N., Justo, G. Z., Durán, M., Brocchi, M., Cordi, L., Tasic, L., Castro, G. R., & Nakazato, G. (2016). Advances in Chromobacterium violaceum and properties of violacein-Its main secondary metabolite: A review. *Biotechnology Advances*, 34(5), 1030-1045.

Durán, N., Nakazato, G., Durán, M., Berti, I. R., Castro, G. R., Stanisic, D., Brocchi, M., Fávaro, W. J., Ferreira-Halder, C. V., Justo, G. Z., & Tasic, L. (2021). Multi-target drug with potential applications: violacein in the spotlight. *World Journal of Microbiology and Biotechnology 2021 37:9*, *37*(9), 1–20.

ELAVL1 (ELAV (embryonic lethal, abnormal vision, Drosophila)-like 1 (Hu antigen R)). (2008) from https://atlasgeneticsoncology.org/gene/44237/.

Feng, P., Chen, D., Wang, X., Li, Y., Li, Z., Li, B., ... & Ji, C. (2022). Inhibition of the m6A reader IGF2BP2 as a strategy against T-cell acute lymphoblastic leukemia. *Leukemia*, *36*(9), 2180-2188.

Ferreira, C. V., Bos, C. L., Versteeg, H. H., Justo, G. Z., Durán, N., & Peppelenbosch, M. P. (2004). Molecular mechanism of violacein-mediated human leukemia cell death. *Blood*, *104*(5), 1459–1464.

Filippova, N., Yang, X., Wang, Y., Gillespie, G. Y., Langford, C., King, P. H., Wheeler, C., & Nabors, L. B. (2011). The RNA-binding protein HuR promotes glioma growth and treatment resistance. *Molecular Cancer Research, 9*(5), 648.

Franken, N. A. P., Rodermond, H. M., Stap, J., Haveman, J., & van Bree, C. (2006). Clonogenic assay of cells *in vitro*. *Nature Protocols*, *1*(5), 2315–2319.

Gao, Z., Harwig, A., Berkhout, B., & Herrera-Carrillo, E. (2017). Mutation of nucleotides around the +1 position of type 3 polymerase III promoters: The effect on transcriptional activity and start site usage. *Transcription*, *8*(5), 275–287.

Giuliano, C. J., Lin, A., Girish, V., & Sheltzer, J. M. (2019). Generating Single Cell-Derived Knockout Clones in Mammalian Cells with CRISPR/Cas9. *Current Protocols in Molecular Biology*, *128*(1), e100.

Gomy, I., Wu, N., Kunej, T., Roffe, M., Rudin, C. M., Uddin, F., & Sen, T. (2020). CRISPR Gene Therapy: Applications, Limitations, and Implications for the Future. *Frontiers in Oncology*, 10, 1387.

Gonçalves, P. R., Rocha-Brito, K. J. P., Fernandes, M. R. N., Abrantes, J. L., Durán, N., & Ferreira-Halder, C. V. (2016). Violacein induces death of RAS-mutated metastatic melanoma by impairing autophagy process. *Tumor Biology*, *37*(10), 14049–14058.

Graf R., Li, X., Chu, V. T., Correspondence, K. R., & Rajewsky, K. (2019). sgRNA Sequence Motifs Blocking Efficient CRISPR/ Cas9-Mediated Gene Editing. *Cell Reports*, *26*(5), 1098-1103.

Guo, C., Ma, X., Gao, F., & Guo, Y. (2023). Off-target effects in CRISPR/Cas9 gene editing. *Frontiers in Bioengineering and Biotechnology*, *11*, 1143157.

Hall, J. A., Seedarala, S., Zhao, H., Garg, G., Ghosh, S., & Blagg, B. S. J. (2016). Novobiocin Analogues That Inhibit the MAPK Pathway. *Journal of Medicinal Chemistry*, *59*(3), 925–933.

Han, L., Lei, G., Chen, Z., Zhang, Y., Huang, C., & Chen, W. (2022). IGF2BP2 Regulates MALAT1 by Serving as an N6-Methyladenosine Reader to Promote NSCLC Proliferation. *Frontiers in Molecular Biosciences*, 8, 780089.

Han, S. J., Kwon, S., & Kim, K. S. (2021). Challenges of applying multicellular tumor spheroids in preclinical phase. *Cancer cell international*, 21, 1-19.

Hanahan, D. (2022). Hallmarks of Cancer: New Dimensions. *Cancer Discovery*, *12*(1), 31–46.

Hu, X., Peng, W. X., Zhou, H., Jiang, J., Zhou, X., Huang, D., Mo, Y. Y., & Yang, L. (2019). IGF2BP2 regulates DANCR by serving as an N6-methyladenosine reader. *Cell Death & Differentiation*, *27*(6), 1782–1794.

Huang, R. Sheng, Zheng, Y. liang, Li, C., Ding, C., Xu, C., & Zhao, J. (2018). MicroRNA-485-5p suppresses growth and metastasis in non-small cell lung cancer cells by targeting IGF2BP2. *Life Sciences*, *199*, 104–111.

Huang, S., Wu, Z., Cheng, Y., Wei, W., & Hao, L. (2019). Insulin-like growth factor 2 mRNA binding protein 2 promotes aerobic glycolysis and cell proliferation in pancreatic ductal adenocarcinoma via stabilizing GLUT1 mRNA. *Acta Biochimica et Biophysica Sinica*, *51*(7), 743–752.

Irion, S., Luche, H., Gadue, P., Fehling, H. J., Kennedy, M., & Keller, G. (2007). Identification and targeting of the ROSA26 locus in human embryonic stem cells. *Nature Biotechnology*, *25*(12), 1477–1482.

Kendzia, S., Franke, S., Kröhler, T., Golob-Schwarzl, N., Schweiger, C., Toeglhofer, A. M., Skofler, C., Uranitsch, S., El-Heliebi, A., Fuchs, J., Punschart, A., Stiegler, P., Keil, M., Hoffmann, J., Henderson, D., Lehrach, H., Yaspo, M. L., Reinhard, C., Schäfer, R., … Kessler, S. M. (2023). A combined computational and functional approach identifies IGF2BP2 as a driver of chemoresistance in a wide array of pre-clinical models of colorectal cancer. *Molecular Cancer*, *22*(1), 89.

Kessler, S. M., Laggai, S., Barghash, A., Schultheiss, C. S., Lederer, E., Artl, M., Helms, V., Haybaeck, J., & Kiemer, A. K. (2015). IMP2/p62 induces genomic instability and an aggressive hepatocellular carcinoma phenotype. *Cell Death and Disease*, *6*(10), e1894–e1894.

Kessler, S. M., Lederer, E., Laggai, S., Golob-Schwarzl, N., Hosseini, K., Petzold, J., Schweiger, C., Reihs, R., Keil, M., Hoffmann, J., Mayr, C., Kiesslich, T., Pichler, M., Kim, K. S., Rhee, H., Park, Y. N., Lax, S., Obrist, P., Kiemer, A. K., & Haybaeck, J. (2017). IMP2/IGF2BP2 expression, but not IMP1 and IMP3, predicts poor outcome in patients and high tumor growth rate in xenograft models of gallbladder cancer. *Oncotarget*, *8*(52), 89736.

Kessler, S. M., Pokorny, J., Zimmer, V., Laggai, S., Lammert, F., Bohle, R. M., & Kiemer, A. K. (2013). IGF2 mRNA binding protein p62/IMP2-2 in hepatocellular carcinoma: Antiapoptotic action is independent of IGF2/PI3K signaling. *American Journal of Physiology - Gastrointestinal and Liver Physiology*, *304*(4), G328-G336.

Kim, D., Mollah, M. L., & Kim, K. (2012). Induction of apoptosis of SW480 human colon cancer cells by (−)-epicatechin isolated from Bulnesia sarmienti. *Anticancer Research*, *32*(12), 5353-5361.

Kim, Y. J., Yuk, N., Shin, H. J., & Jung, H. J. (2021). The Natural Pigment Violacein Potentially Suppresses the Proliferation and Stemness of Hepatocellular Carcinoma Cells *In Vitro*. *International Journal of Molecular Sciences*, *22*(19), 10731.

Kroemer, G., Galluzzi, L., Kepp, O., & Zitvogel, L. (2013). Immunogenic Cell Death in Cancer Therapy. *Annual Review of Immunology*, 31, 51-72.

Laurin, P., Ferroud, D., Schio, L., Klich, M., Dupuis-Hamelin, C., Mauvais, P., Lassaigne, P., Bonnefoy, A., & Musicki, B. (1999). Structure-activity relationship in two series of aminoalkyl

substituted coumarin inhibitors of gyrase B. *Bioorganic & Medicinal Chemistry Letters*, *9*(19), 2875–2880.

Levy, N. S., Chung, S., Furneaux, H., & Levy, A. P. (1998). Hypoxic stabilization of vascular endothelial growth factor mRNA by the RNA-binding protein HuR. *The Journal of Biological Chemistry*, *273*(11), 6417–6423.

Lewis, R. J., Tsai, F. T. F., & Wigley, D. B. (1996). Molecular mechanisms of durg inhibition of DNA gyrase. *BioEssays*, *18*(8), 661–671.

Li, T., Hu, P. S., Zuo, Z., Lin, J. F., Li, X., Wu, Q. N., Chen, Z. H., Zeng, Z. L., Wang, F., Zheng, J., Chen, D., Li, B., Kang, T. B., Xie, D., Lin, D., Ju, H. Q., & Xu, R. H. (2019). METTL3 facilitates tumor progression via an m6A-IGF2BP2-dependent mechanism in colorectal carcinoma. *Molecular Cancer*, *18*(1), 1–15.

Li, X., Li, Y., & Lu, H. (2017). miR-1193 Suppresses Proliferation and Invasion of Human Breast Cancer Cells Through Directly Targeting IGF2BP2. *Oncology Research*, *25*(4), 579.

Liu, P., Liang, S. Q., Zheng, C., Mintzer, E., Zhao, Y. G., Ponnienselvan, K., Mir, A., Sontheimer, E. J., Gao, G., Flotte, T. R., Wolfe, S. A., & Xue, W. (2021). Improved prime editors enable pathogenic allele correction and cancer modelling in adult mice. *Nature Communications*, *12*(1), 1–13.

Liu, T., Han, C., Hu, C., Mao, S., Sun, Y., Yang, S., & Yang, K. (2023). Knockdown of IGF2BP2 inhibits colorectal cancer cell proliferation, migration and promotes tumor immunity by down-regulating MYC expression. *Xi Bao Yu Fen Zi Mian Yi Xue Za Zhi = Chinese Journal of Cellular and Molecular Immunology*, *39*(4), 303–310.

Liu, T.-Y., Hu, C.-C., Han, C.-Y., Mao, S.-Y., Zhang, W.-X., Xu, Y.-M., Sun, Y.-J., Jiang, D.-B., Zhang, X.-Y., Zhang, J.-X., Wang, J., Qiao, X.-P., Pan, J.-Y., Yang, S.-Y., & Yang, K. (2023). IGF2BP2 promotes colorectal cancer progression by upregulating the expression of TFRC and enhancing iron metabolism. *Biology Direct*, *18*(1), 19.

López De Silanes, I., Fan, J., Yang, X., Zonderman, A. B., Potapova, O., Pizer, E. S., & Gorospe, M. (2003). Role of the RNA-binding protein HuR in colon carcinogenesis. *Oncogene*, *22*(46), 7146–7154.

Lu, M., Nakamura, R. M., Dent, E. D. B., Zhang, J. Y., Nielsen, F. C., Christiansen, J., Chan, E. K. L., & Tan, E. M. (2001). Aberrant Expression of Fetal RNA-Binding Protein p62 in Liver Cancer and Liver Cirrhosis. *The American Journal of Pathology*, *159*(3), 945.

Ma, H., Wu, Y., Dang, Y., Choi, J. G., Zhang, J., & Wu, H. (2014). Pol III Promoters to Express Small RNAs: Delineation of Transcription Initiation. *Molecular Therapy-Nucleic Acids*, *3*(5), e161.

Maity, A., & Das, B. (2016). N6-methyladenosine modification in mRNA: machinery, function and implications for health and diseases. *The FEBS Journal*, *283*(9), 1607–1630.

Masuelli, L., Pantanella, F., La Regina, G., Benvenuto, M., Fantini, M., Mattera, R., Di Stefano, E., Mattei, M., Silvestri, R., Schippa, S., Manzari, V., Modesti, A., & Bei, R. (2016). Violacein, an indole-derived purple-colored natural pigment produced by Janthinobacterium lividum, inhibits the growth of head and neck carcinoma cell lines both *in vitro* and *in vivo*. *Tumor Biology*, *37*(3), 3705–3717.

Mehta, T., Vercruysse, K., Johnson, T., Ejiofor, A. O., Myles, E., & Quick, Q. A. (2015). Violacein induces p44/42 mitogen-activated protein kinase-mediated solid tumor cell death and inhibits tumor cell migration. *Molecular Medicine Reports*, *12*(1), 1443–1448.

Meisner, N. C., Hintersteiner, M., Mueller, K., Bauer, R., Seifert, J. M., Naegeli, H. U., Ottl, J., Oberer, L., Guenat, C., Moss, S., Harrer, N., Woisetschlaeger, M., Buehler, C., Uhl, V., & Auer, M. (2007). Identification and mechanistic characterization of low-molecular-weight inhibitors for HuR. *Nature Chemical Biology*, *3*(8), 508–515.

Menger, L., Vacchelli, E., Adjemian, S., Martins, I., Ma, Y., Shen, S., Yamazaki, T., Sukkurwala, A. Q., Michaud, M., Mignot, G., Schlemmer, F., Sulpice, E., Locher, C., Gidrol, X., Ghiringhelli, F., Modjtahedi, N., Galluzzi, L., André, F., Zitvogel, L., … Kroemer, G. (2012). Cardiac glycosides exert anticancer effects by inducing immunogenic cell death. S*cience Translational Medicine*, *4*(143). 143ra99.

Mitsunari, K., Miyata, Y., Asai, A., Matsuo, T., Shida, Y., Hakariya, T., & Sakai, H. (2016). Human antigen R is positively associated with malignant aggressiveness via upregulation of cell proliferation, migration, and vascular endothelial growth factors and cyclooxygenase-2 in prostate

cancer. *Translational Research : The Journal of Laboratory and Clinical Medicine*, *175*, 116–128.

Mu, Q., Wang, L., Yu, F., Gao, H., Lei, T., Li, P., Liu, P., Zheng, X., Hu, X., Chen, Y., Jiang, Z., Sayari, A. J., Shen, J., & Huang, H. (2015). Imp2 regulates GBM progression by activating IGF2/PI3K/Akt pathway. *Cancer Biology & Therapy*, *16*(4), 623.

Naeem, A., Hu, P., Yang, M., Zhang, J., Liu, Y., Zhu, W., & Zheng, Q. (2022). Natural Products as Anticancer Agents: Current Status and Future Perspectives. *Molecules*, *27*(23), 8367.

Nasti, R., Rossi, D., Amadio, M., Pascale, A., Unver, M. Y., Hirsch, A. K. H., & Collina, S. (2017). Compounds Interfering with Embryonic Lethal Abnormal Vision (ELAV) Protein-RNA Complexes: An Avenue for Discovering New Drugs. *Journal of Medicinal Chemistry*, *60*(20), 8257–8267.

Neroni, B., Zingaropoli, M. A., Radocchia, G., Ciardi, M. R., Mosca, L., Pantanella, F., & Schippa, S. (2022). Evaluation of the anti-proliferative activity of violacein, a natural pigment of bacterial origin, in urinary bladder cancer cell lines. *Oncology Letters*, *23*(4), 1-9.

Newman, D. J., & Cragg, G. M. (2020). Natural Products as Sources of New Drugs over the Nearly Four Decades from 01/1981 to 09/2019. *Journal of Natural Products*, *83*(3), 770–803.

Niesporek, S., Kristiansen, G., Thoma, A., Weichert, W., Noske, A., Buckendahl, A. C., Jung, K., Stephan, C., Dietel, M., & Denkert, C. (2008). Expression of the ELAV-like protein HuR in human prostate carcinoma is an indicator of disease relapse and linked to COX-2 expression. *International Journal of Oncology*, *32*(2), 341–347.

Novikov, N. M., Zolotaryova, S. Y., Gautreau, A. M., & Denisov, E. V. (2020). Mutational drivers of cancer cell migration and invasion. *British Journal of Cancer*, *124*(1), 102–114.

Otto, T., & Sicinski, P. (2017). Cell cycle proteins as promising targets in cancer therapy. *Nature Reviews Cancer*, *17*(2), 93–115.

Papapetrou, E. P., & Schambach, A. (2016). Gene Insertion Into Genomic Safe Harbors for Human Gene Therapy. *Molecular Therapy*, *24*(4), 678.

Papiez, M. A., Baran, J., Bukowska-Straková, K., & Wiczkowski, W. (2010). Antileukemic action of (−)-epicatechin in the spleen of rats with acute myeloid leukemia. *Food and Chemical Toxicology*, *48*(12), 3391–3397.

Patridge, E., Gareiss, P., Kinch, M. S., & Hoyer, D. (2016). An analysis of FDA-approved drugs: natural products and their derivatives. *Drug Discovery Today*, *21*(2), 204–207.

Pereira, B., Billaud, M., & Almeida, R. (2017). RNA-Binding Proteins in Cancer: Old Players and New Actors. *Trends in Cancer*, *3*(7), 506–528.

Pereyra-Vergara, F., Olivares-Corichi, I. M., Perez-Ruiz, A. G., Luna-Arias, J. P., & García-Sánchez, J. R. (2020). Apoptosis Induced by (−)-Epicatechin in Human Breast Cancer Cells is Mediated by Reactive Oxygen Species. *Molecules*, *25*(5), 1020.

Pu, J., Wang, J., Qin, Z., Wang, A., Zhang, Y., Wu, X., Wu, Y., Li, W., Xu, Z., Lu, Y., Tang, Q., & Wei, H. (2020). IGF2BP2 Promotes Liver Cancer Growth Through an m6A-FEN1-Dependent Mechanism. *Frontiers in Oncology*, 10, 578816.

Richards, N. G., Rittenhouse, D. W., Freydin, B., Cozzitorto, J. A., Grenda, D., Rui, H., Gonye, G., Kennedy, E. P., Yeo, C. J., Brody, J. R., & Witkiewicz, A. K. (2010). HuR status is a powerful marker for prognosis and response to gemcitabine-based chemotherapy for resected pancreatic ductal adenocarcinoma patients. *Annals of Surgery*, *252*(3), 499–505.

Rodrigues, A. L., Trachtmann, N., Becker, J., Lohanatha, A. F., Blotenberg, J., Bolten, C. J., Korneli, C., de Souza Lima, A. O., Porto, L. M., Sprenger, G. A., & Wittmann, C. (2013). Systems metabolic engineering of Escherichia coli for production of the antitumor drugs violacein and deoxyviolacein. *Metabolic Engineering*, *20*, 29–41.

Saikolappan, S., Kumar, B., Shishodia, G., Koul, S., & Koul, H. K. (2019). Reactive oxygen species and cancer: A complex interaction. *Cancer Letters*, *452*, 132–143.

Schultz, C. W., Preet, R., Dhir, T., Dixon, D. A., & Brody, J. R. (2020). Understanding and targeting the disease-related RNA binding protein human antigen R (HuR). *Wiley Interdisciplinary Reviews: RNA*, *11*(3), 1581.

Schwartz, G. N., Teicher, B. A., Eder, J. P., Korbut, T., Holden, S. A., Ara, G., & Herman, T. S. (1993). Modulation of antitumor alkylating agents by novobiocin, topotecan, and lonidamine. *Cancer Chemotherapy and Pharmacology*, *32*(6), 455–462.

Shay, J., Elbaz, H. A., Lee, I., Zielske, S. P., Malek, M. H., & Hüttemann, M. (2015). Molecular mechanisms and therapeutic effects of (-)-epicatechin and other polyphenols in cancer, inflammation, diabetes, and neurodegeneration. *Oxidative Medicine and Cellular Longevity*.

Shrestha, D., Bag, A., Wu, R., Zhang, Y., Tang, X., Qi, Q., Xing, J., & Cheng, Y. (2022). Genomics and epigenetics guided identification of tissue-specific genomic safe harbors. *Genome Biology*, *23*(1), 1–17.

Smits, A. H., Ziebell, F., Joberty, G., Zinn, N., Mueller, W. F., Clauder-Münster, S., Eberhard, D., Fälth Savitski, M., Grandi, P., Jakob, P., Michon, A. M., Sun, H., Tessmer, K., Bürckstümmer, T., Bantscheff, M., Steinmetz, L. M., Drewes, G., & Huber, W. (2019). Biological plasticity rescues target activity in CRISPR knock outs. *Nature Methods*, *16*(11), 1087–1093.

Stadler, M., Scherzer, M., Walter, S., Holzner, S., Pudelko, K., Riedl, A., Unger, C., Kramer, N., Weil, B., Neesen, J., Hengstschläger, M., & Dolznig, H. (2018). Exclusion from spheroid formation identifies loss of essential cell-cell adhesion molecules in colon cancer cells. *Scientific Reports*, *8*(1), 1151.

Stephens, C. J., Kashentseva, E., Everett, W., Kaliberova, L., & Curiel, D. T. (2018). Targeted *in vivo* knock-in of human alpha-1-antitrypsin cDNA using adenoviral delivery of CRISPR/Cas9. *Gene Therapy*, *25*(2), 139–156.

Stephens, C. J., Lauron, E. J., Kashentseva, E., Lu, Z. H., Yokoyama, W. M., & Curiel, D. T. (2019). Long-term correction of hemophilia B using adenoviral delivery of CRISPR/Cas9. *Journal of Controlled Release*, *298*, 128–141.

Sung, H., Ferlay, J., Siegel, R. L., Laversanne, M., Soerjomataram, I., Jemal, A., & Bray, F. (2021). Global Cancer Statistics 2020: GLOBOCAN Estimates of Incidence and Mortality Worldwide for 36 Cancers in 185 Countries. *CA: A Cancer Journal for Clinicians*, *71*(3), 209–249.

Surks, H. K., Richards, C. T., & Mendelsohn, M. E. (2003). Myosin Phosphatase-Rho Interacting Protein. *Journal of Biological Chemistry*, *278*(51), 51484–51493.

Suswam, E. A., Nabors, L. B., Huang, Y., Yang, X., & King, P. H. (2005). IL-1beta induces stabilization of IL-8 mRNA in malignant breast cancer cells via the 3' untranslated region: Involvement of divergent RNA-binding factors HuR, KSRP and TIAR. *International Journal of Cancer*, *113*(6), 911–919.

Tesniere, A., Schlemmer, F., Boige, V., Kepp, O., Martins, I., Ghiringhelli, F., Aymeric, L., Michaud, M., Apetoh, L., Barault, L., Mendiboure, J., Pignon, J. P., Jooste, V., Van Endert, P., Ducreux, M., Zitvogel, L., Piard, F., & Kroemer, G. (2009). Immunogenic death of colon cancer cells treated with oxaliplatin. *Oncogene*, *29*(4), 482–491.

Uhlen, M., Zhang, C., Lee, S., Sjöstedt, E., Fagerberg, L., Bidkhori, G., Benfeitas, R., Arif, M., Liu, Z., Edfors, F., Sanli, K., Von Feilitzen, K., Oksvold, P., Lundberg, E., Hober, S., Nilsson, P., Mattsson, J., Schwenk, J. M., Brunnström, H., … Ponten, F. (2017). A pathology atlas of the human cancer transcriptome. *Science*, *357*(6352).

Vasile, F., Della Volpe, S., Ambrosio, F. A., Costa, G., Unver, M. Y., Zucal, C., Rossi, D., Martino, E., Provenzani, A., Hirsch, A. K. H., Alcaro, S., Potenza, D., & Collina, S. (2018). Exploration of ligand binding modes towards the identification of compounds targeting HuR: a combined STD-NMR and Molecular Modelling approach. *Scientific Reports*, *8*(1), 13780.

Venegas, F. A., Köllisch, G., Mark, K., Diederich, W. E., Kaufmann, A., Bauer, S., Chavarría, M., Araya, J. J., & García-Piñeres, A. J. (2019). The Bacterial Product Violacein Exerts an Immunostimulatory Effect Via TLR8. *Scientific Reports*, *9*(1) 13661.

Wang, J., Wang, B., Bi, J., & Zhang, C. (2011). Cytoplasmic HuR expression correlates with angiogenesis, lymphangiogenesis, and poor outcome in lung cancer. *Medical Oncology*, *28* (1), 577-585.

Wang, J., Zhao, W., Guo, Y., Zhang, B., Xie, Q., Xiang, D., Gao, J., Wang, B., & Chen, Z. (2009). The expression of RNA-binding protein HuR in non-small cell lung cancer correlates with vascular endothelial growth factor-C expression and lymph node metastasis. *Oncology*, *76*(6), 420–429.

Wang, Y., Lu, J. H., Wu, Q. N., Jin, Y., Wang, D. S., Chen, Y. X., Liu, J., Luo, X. J., Meng, Q., Pu, H. Y., Wang, Y. N., Hu, P. S., Liu, Z. X., Zeng, Z. L., Zhao, Q., Deng, R., Zhu, X. F., Ju, H. Q., & Xu, R. H. (2019). LncRNA LINRIS stabilizes IGF2BP2 and promotes the aerobic glycolysis in colorectal cancer. *Molecular Cancer*, *18*(1), 1–18.

Weng, H., Huang, F., Yu, Z., Chen, Z., Prince, E., Kang, Y., ... & Chen, J. (2022). The m6A reader IGF2BP2 regulates glutamine metabolism and represents a therapeutic target in acute myeloid leukemia. *Cancer Cell*, *40*(12), 1566-1582.

Wong, N., Liu, W., & Wang, X. (2015). WU-CRISPR: Characteristics of functional guide RNAs for the CRISPR/Cas9 system. *Genome Biology*, *16*(1), 1–8.

Wu, X. L., Lu, R. Y., Wang, L. K., Wang, Y. Y., Dai, Y. J., Wang, C. Y., Yang, Y. J., Guo, F., Xue, J., & Yang, D. D. (2019). Long noncoding RNA HOTAIR silencing inhibits invasion and proliferation of human colon cancer LoVo cells via regulating IGF2BP2. *Journal of Cellular Biochemistry*, *120*(2), 1221–1231.

Wu, X., & Xu, L. (2022). The RNA-binding protein HuR in human cancer: A friend or foe? *Advanced Drug Delivery Reviews*, *184*, 114179.

Xing, M., Li, P., Wang, X., Li, J., Shi, J., Qin, J., Zhang, X., Ma, Y., Francia, G., & Zhang, J. Y. (2020). Overexpression of p62/IMP2 can Promote Cell Migration in Hepatocellular Carcinoma via Activation of the Wnt/β-Catenin Pathway. *Cancers*, *12*(1), 7.

Xu, B. L., Wang, X. M., Chen, G. Y., Yuan, P., Han, L., Qin, P., ... & Gao, Q. L. (2022). In vivo growth of subclones derived from Lewis lung carcinoma is determined by the tumor microenvironment. *American Journal of Cancer Research*, *12*(11), 5255.

Xu, X., Yu, Y., Zong, K., Lv, P., & Gu, Y. (2019). Up-regulation of IGF2BP2 by multiple mechanisms in pancreatic cancer promotes cancer proliferation by activating the PI3K/Akt signaling pathway. *Journal of Experimental and Clinical Cancer Research*, *38*(1), 1–14.

Yang, C. S., & Wang, H. (2016). Cancer Preventive Activities of Tea Catechins. *Molecules*, *21*(12), 1679.

Ye, S., Song, W., Xu, X., Zhao, X., & Yang, L. (2016). IGF2BP2 promotes colorectal cancer cell proliferation and survival through interfering with RAF-1 degradation by miR-195. *FEBS Letters*, *590*(11), 1641–1650.

Yi, X., Zhou, Y., Zheng, W., & Chambers, S. K. (2009). HuR expression in the nucleus correlates with high histological grade and poor disease-free survival in ovarian cancer. *The Australian & New Zealand Journal of Obstetrics & Gynaecology*, *49*(1), 93–98.

Zambrowicz, B. P., Imamoto, A., Fiering, S., Herzenberg, L. A., Kerr, W. G., & Soriano, P. (1997). Disruption of overlapping transcripts in the ROSA βgeo 26 gene trap strain leads to widespread expression of β-galactosidase in mouse embryos and hematopoietic cells. *Proceedings of the National Academy of Sciences*, *94*(8), 3789–3794.

Zheng, C., Liang, S. Q., Liu, B., Liu, P., Kwan, S. Y., Wolfe, S. A., & Xue, W. (2022). A flexible split prime editor using truncated reverse transcriptase improves dual-AAV delivery in mouse liver. *Molecular Therapy*, *30*(3), 1343–1351.

Zhou, J., Wang, G., Chen, Y., Wang, H., Hua, Y., & Cai, Z. (2019). Immunogenic cell death in cancer therapy: Present and emerging inducers. *Journal of Cellular and Molecular Medicine*, *23*(8), 4854–4865.

Zhu, H., Berkova, Z., Mathur, R., Sehgal, L., Khashab, T., Tao, R. H., Ao, X., Feng, L., Sabichi, A. L., Blechacz, B., Rashid, A., & Samaniego, F. (2015). HuR Suppresses Fas Expression and Correlates with Patient Outcome in Liver Cancer. *Molecular Cancer Research, 13*(5), 809–818.

Zhu, Y., Ouyang, Z., Du, H., Wang, M., Wang, J., Sun, H., Kong, L., Xu, Q., Ma, H., & Sun, Y. (2022). New opportunities and challenges of natural products research: When target identification meets single-cell multiomics. *Acta Pharmaceutica Sinica B*, *12*(11), 4011–4039.

8 Appendix

8.1 Abbreviations

A	Absorbance
AAVS1	Adeno-associated virus integration site 1
ANOVA	Analysis of variance
ATCC	American-type culture collection
ADP	Adenosine diphosphate
ATP	Adenosine triphosphate
BCA	Bicinchoninic acid
bp	Base pairs
BSA	Bovine serum albumin
°C	Grad celsius
Cas9	CRISPR-associated (protein) 9
cDNA	Complementary DNA
c-NHEJ	Classical non-homologous end joining
CFA	Colony formation assay
CRC	Colorectal cancer
CRT	Calreticulin
CRISPR	Clustered regularly interspaced short palindromic repeats
crRNA	CRISPR RNA
cm	Centimeter
Co	Control
Ct	Cycle threshold
d	Day
DANCR	Differentiation antagonizing non-protein coding RNA
DAMPs	Damage-associated molecular patterns
DMEM	Dulbecco's modified Eagle’s medium
DMSO	Dimethyl sulfoxide
DNA	Deoxyribonucleic acid
dTCM	Dead tumor conditioned medium
EC	Epicatechin
ECM	Extracellular matrix
E. coli	Escherichia coli
ELAVL1	ELAV-like RNA-binding protein 1
EMT	Epithelial-mesenchymal transition
EDTA	Ethylene diamine tetra acetic acid
EGFP	Enhanced green fluorescent protein
FACS	Fluorescence-activated cell sorting
FCS	Fetal calf serum

FDA	Food and Drug Administration
Fwd	Forward
g	Relative centrifugal force
gDNA	Genomic DNA
GRCh	Genome reference consortium human
h	Hour
HPLC	High-performance liquid chromatography
HuR	Human antigen R
HRP	Horseradish peroxidase
HVA	Homovanillic acid
HIPS	Helmholtz Institute for Pharmaceutical Research Saarland
HNS	Nucleoplasmic shuttling sequence
HDR	Homology-directed repair (HDR)
HMGA1, HMGA2	High mobility group AT-hook 1 or 2
HMBG1	Nuclear high mobility group box 1
HCC	Hepatocellular carcinoma
KCl	Potassium chloride
kDa	Kilodalton
KH domain	Heterogeneous nuclear ribonucleoprotein (hnrnp)-K homology (KH) domain
KH_2PO_4	Monopotassium phosphate
KO	Knockout
bKO	Biallelic knockout
mKO	Monoallelic knockout
IC_{50}	Half maximal inhibitory concentration
IFNγ	Interferon γ
ICD	Immunogenic cell death
IGF	Insulin-like growth factor
IGF2BP/IMP/VICKZ/ ZBP-1/2/3	Insulin-like growth factor 2 mRNA-binding protein 1/2/3
IL	Interleukin
Indel	Insertion and/or deletion
LB	Lysogeny broth
LBamp	Ampicillin-resistant lysogeny broth
LPS	Lipopolysaccharide
ml	Milliliter
min	Minutes
µm	Micrometer
µM	Micromolar
µl	Microlitre
m6A	N6-methyladenosine
MI	Median fluorescence intensity
mRNA	Messenger-RNA

MMLV	Wild-type Moloney murine leukemia virus
mm	Millimeter
MTT	3-(4,5-dimethylthiazol-2-yl)-2,5-diphenyltetrazolium bromide
MYC	C-MYC, MYC proto-oncogene, transcription factor
n	Number of biological replicates
NaCl	Sodium chloride
Na_2HPO_4	Disodium phosphate
NaOH	Sodium hydroxide
NFκB	Nuclear factor kappa B
n.s.	Not significant
ng	Nanogram
NGS	Next-generation sequencing
NOD1	Nucleotide-binding oligomerization domain protein-1
NovNa	Novobiocin
Oxa	Oxaliplatin
OD_{600}	Optical density measured at a wavelength of λ=600 nm
P value	Probability value
p62	Splice variant of IMP2
PAM	Protospacer adjacent motif
PBS	Primer-binding site
PBS (1X)	Phosphate buffered saline
PE	Prime editing
PE2	Prime editor 2
PMA	Phorbol-12-myristate 13-acetate
pH	Potential hydrogen
pegRNA	Prime editing guide RNA
PPP1R12C	Protein phosphatase 1 regulatory subunit 12C
PPARγ	Peroxisome proliferator-activated receptor gamma
ROS	Reactive oxygen species
RT-qPCR	Reverse transcriptase quantitative polymerase chain reaction
PVDF	Polyvinylidene difluoride
Rev	Reverse
RBB	Rockland blocking buffer
RIPA	Radio immunoprecipitation assay
RBP	RNA-binding protein
RNA	Ribonucleic acid
rRNA	Ribosomal RNA
siRNA	Small interfering RNA
shRNA	Short hairpin RNA
RNP	Ribonucleoprotein
RPMI	Roswell park memorial institute
RRM	RNA recognition motif
rpm	Rounds per minute

RT	Room temperature
Rosa26	Reverse orientation splice acceptor 26
s	Seconds
SDS-PAGE	Sodium dodecyl sulfate-polyacrylamide gel electrophoresis
SEAP	Secreted embryonic alkaline phosphatase
SEM	Standard error of the mean
(s)gRNA	(Single) guide RNA
SHL	Safe harbor locus
STD-NMR	Saturation transfer difference- non-magnetic resonance
Tris-HCl	(Hydroxymethyl)aminomethane-hydrochloride
TCM	Tumor-conditioned medium
TNF	Tumor necrosis factor
TBE	Tris/borate/edta
TAE	Tris/acetate/edta
TLR	Toll-like receptor
TSC1	Tuberous sclerosis 1
ΔTm	Melting temperature shift
UV	Ultraviolet
WHO	World health organization
WT	Wild-type

8.2 Supplementary tables

Table 1. Attempts to generate IMP2 biallelic knockout (bKO) using different gene editing approaches.

Cell line	**Approach**	**Total attempts**	**bKO generated**
Huh7	CRISPR/Cas9 (RNP-delivery)	2	No
Huh7	Prime editing	9	No
Huh7	CRISPR/Cas9 (plasmid-based)	3	No
HepG2	CRISPR/Cas9 (RNP delivery)	3	No
HepG2	Prime editing	8	No
SW480	CRISPR/Cas9 (RNP-delivery)	4	No
SW480	Prime editing	4	No
A549	Prime editing	2	No
A549	CRISPR/Cas9 (plasmid-based)	2	No
LLC1	Prime editing	7	No
LLC1	CRISPR/Cas9 (plasmid-based)	3	Yes

Note: The CRISPR/Cas9-RNP delivery approach was performed by Dr. Tarek Kröhler.

Table 2. Next-generation sequencing reads.

Cell line	**gRNA**	**NGS sequence read**
A549-control	gRNA1	NCTTCAAGATTTCCTACATCCCGGATGAAGAGGTGAGCTCCC CTTCGCCCCCTCAGCGAGCCCAGCGTGGGGGCCACTCT
A549	gRNA1	NCTTCAAGATTTCCTACATCCCGGATGAAGAGGTGAGCTCCC CTTCTGCCCCCTCAGCGAGCCCAGCGTGGGGACCACTC
A549-control	gRNA2	NCCCTCCTTTCCGATGATGGCACCAACAAACTGGGTGGGGA CCAGGATCCGCAGCGGGAAATCAATCTGTCTGGCCTGAG
A549	gRNA1	GCCCTCCTTTCCGATGATGGCACCAACAAACTGGGTGGGGA CCAGGATCCAGCGGGAAATCAATCTGTCTGGCCTGAGAA
Huh7-control	gRNA1	NCTTCAAGATTTCCTACATCCCGGATGAAGAGGTGAGCTCCC CTTCGCCCCCTCAGCGAGCCCAGCGTGGGGACCACTCT
Huh7	gRNA1	NCTTCAAGATTTCCTACATCCCGGATGAAGAGGTGAGCTCCC CTCCGCCCCCTCAGCGAGCCCAGCGTGGGGACCACTCT
Huh7	gRNA1 and gRNA2	CCTTCAAGATTTCCTACATCCCGGATGAAGAGGTGAGCTCCC CTTCGTGGATCCTGGTCCCCACCCAGTTTGTTGGTGCC

8.3 Supplementary work on auratryptanon

8.3.1 Introduction

The natural compound auratryptanon was initially discovered in an extract of *Stigmatella aurantiaca* (*Sga32*) during the search for novel anti-infectives. It has a tryptophan-based structure (**Supplementary Figure 1**) and displays significant activity against various gram-negative strains (Dahlem dissertation 2020).

The cytotoxic effects of auratryptanon were assessed in MCF7, Huh7, Huh7.5, and HCT116 cells, with IC_{50} values ranging from 1.18 to 3.35 μM, as previously published (Dahlem dissertation 2020). The 2D cell proliferation assay revealed the anti-proliferative action of auratryptanon on HCT116 cells at concentrations similar to their IC_{50} values (Dahlem dissertation 2020). The impact of auratryptanon on another cancer hallmark, migration, was evaluated in HCT116 cells. However, no significant effect was observed up to the tested concentration of 2.5 μM (Dahlem dissertation 2020).

The imbalance in redox equilibrium plays a crucial role in the formation, growth, and spread of tumor cells (Saikolappan et al., 2019). This imbalance can be attributed to elevated levels of reactive oxygen species (ROS), resulting from a decreased activity of cellular antioxidant enzymes. Consequently, this can lead to malignant transformation through specific molecular mechanisms, such as nuclear factor (erythroid-derived 2)-like-2 factor (Nrf2) and NFκB (Aggarwal et al., 2019). However, when ROS levels cross a threshold, this leads to the activation of several cell death pathways, resulting in the death of tumor cells (Dharmaraja, 2017). This in turn serves as a therapeutic strategy against cancer.

The ability of auratryptanon to induce oxidative stress was assessed by measuring the production of reactive oxygen species (ROS), specifically hydrogen peroxide levels. This assessment was conducted on both wild-type and doxorubicin-resistant Huh7 cells following treatment.

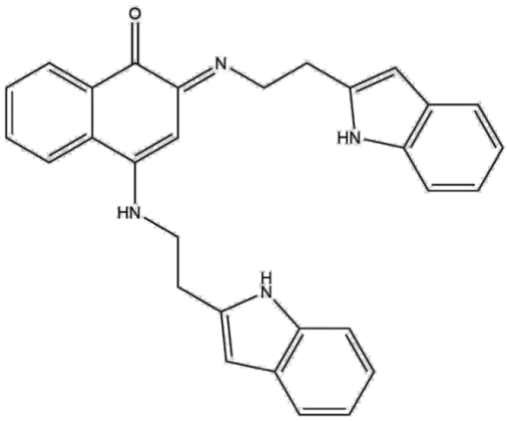

Supplementary Figure 1. Auratryptanon: chemical structure (Dahlem dissertation 2020).

8.3.2 Results

ROS production upon treatment with auratryptanon in wild-type and doxorubicin-resistant Huh7 cells was investigated. Hydrogen peroxide production was measured using the HVA assay at 6 h post-treatment. The results indicated that auratryptanon treatment did not yield a significant difference in ROS production between the wild-type and doxorubicin-resistant Huh7 cell lines when tested up to a concentration of 5 µM (**Supplementary Figure 2**).

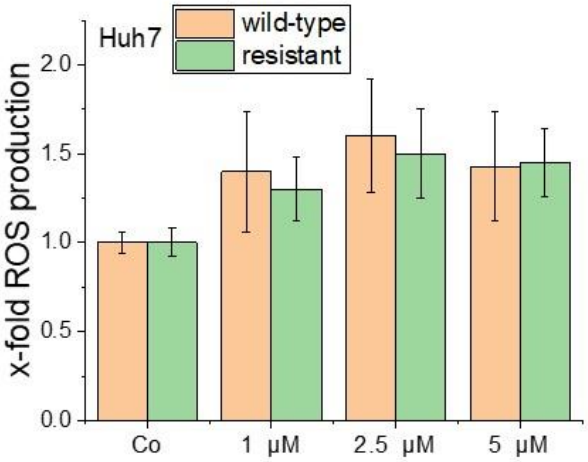

Supplementary Figure 2. Effect of auratryptanon on ROS production in wild-type and doxorubicin-resistant Huh7 cells. Cells were treated with different concentrations of auratryptanon and solvent control (Co) for 6 h and ROS production was measured by HVA assay. Statistical analysis was performed using one-way ANOVA followed by Bonferroni's post-hoc analysis, comparing auratryptanon-treated to solvent control-treated cells. Data is normalized to solvent control (Co) and expressed as mean ± SEM, n=3 (triplicates).

8.3.3 Discussion

Doxorubicin, a widely used chemotherapeutic agent, exhibited similar cytotoxic activity as auratryptanon upon Huh7 cells (Dahlem dissertation 2020). Previously, auratryptanon demonstrated an increase in hydrogen peroxide levels, consequently demonstrating elevated ROS production in A549 and Huh7.5 cells upon treatment (Dahlem dissertation 2020). This suggests that the compound might induce oxidative stress, which could lead to cancer cell death. To further corroborate these findings, the impact of auratryptanon on ROS production in Huh7 cells was examined. The 6 h time point was chosen based on prior data revealing a noteworthy ROS increase in both A549 and Huh7.5 cells treated with 2.5 µM of auratryptanon (Dahlem dissertation 2020). No difference in ROS levels was observed in either the wild-type or doxorubicin-resistant Huh7 cells. However, no conclusion could be drawn on auratryptanon's ability to induce ROS in Huh7 cells as there was no positive control included in the study and only one-time point was assessed. While preceding *in vitro* studies have emphasized the efficacy of auratryptanon as an anticancer agent, future research employing preclinical models and exploring its cellular targets could contribute to advancing the field of cancer research and natural cancer therapeutics.

8.4 Supplementary figures

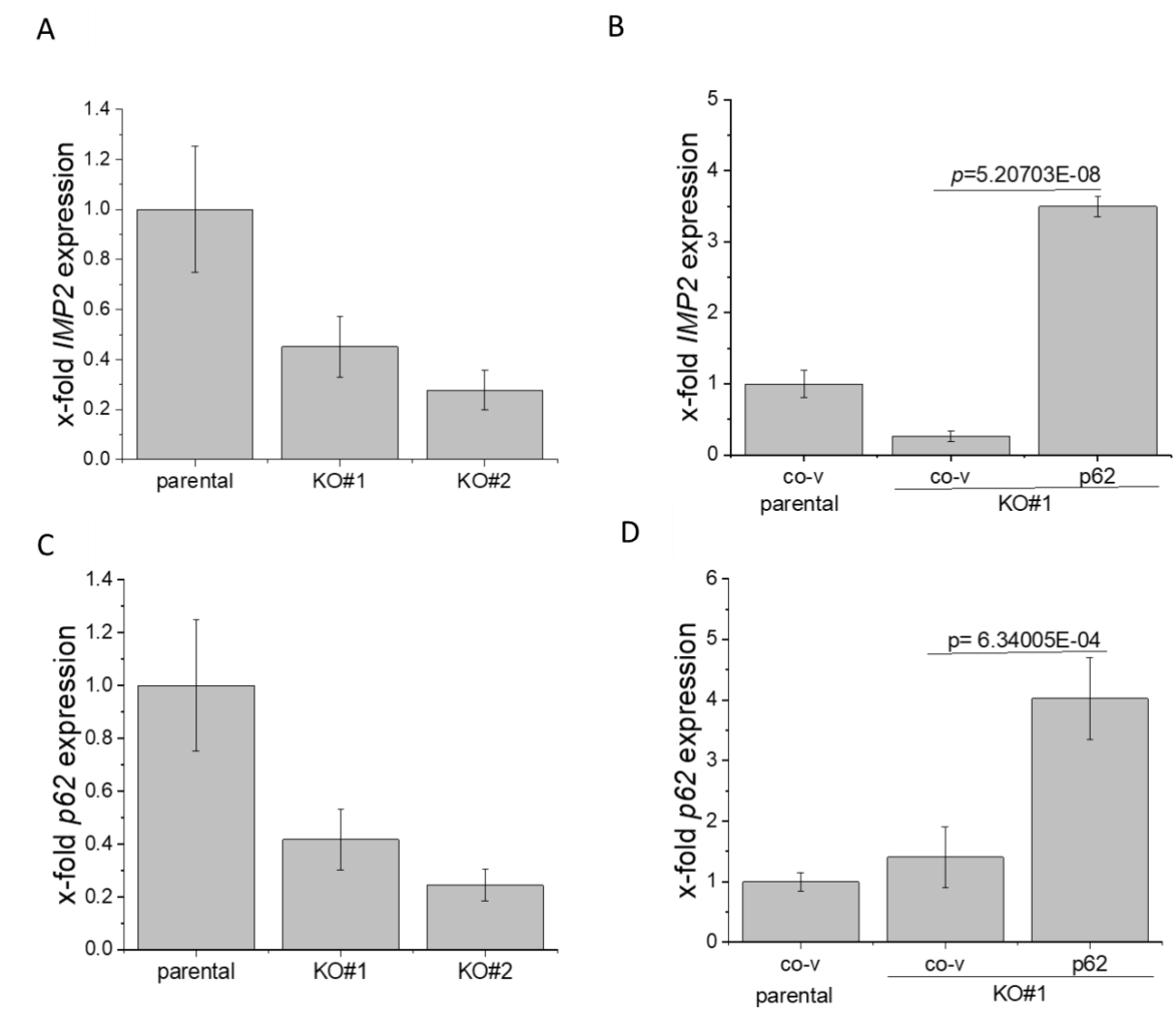

Supplementary Figure 3. *IMP2* and *p62* gene expression were determined in biallelic IMP2 knockout HCT116 cells and *IMP2/p62* overexpressing parental and knockout cells by qPCR. **(**A, C) *IMP2* and *p62* gene expression were determined in biallelic IMP2 knockout HCT116 cells and (B, D) *IMP2/p62* overexpressing parental and knockout cells by qPCR. Values were normalized to the housekeeping gene *RNA18SN5*. Data are represented as means ± SEM, n=3 (triplicates).

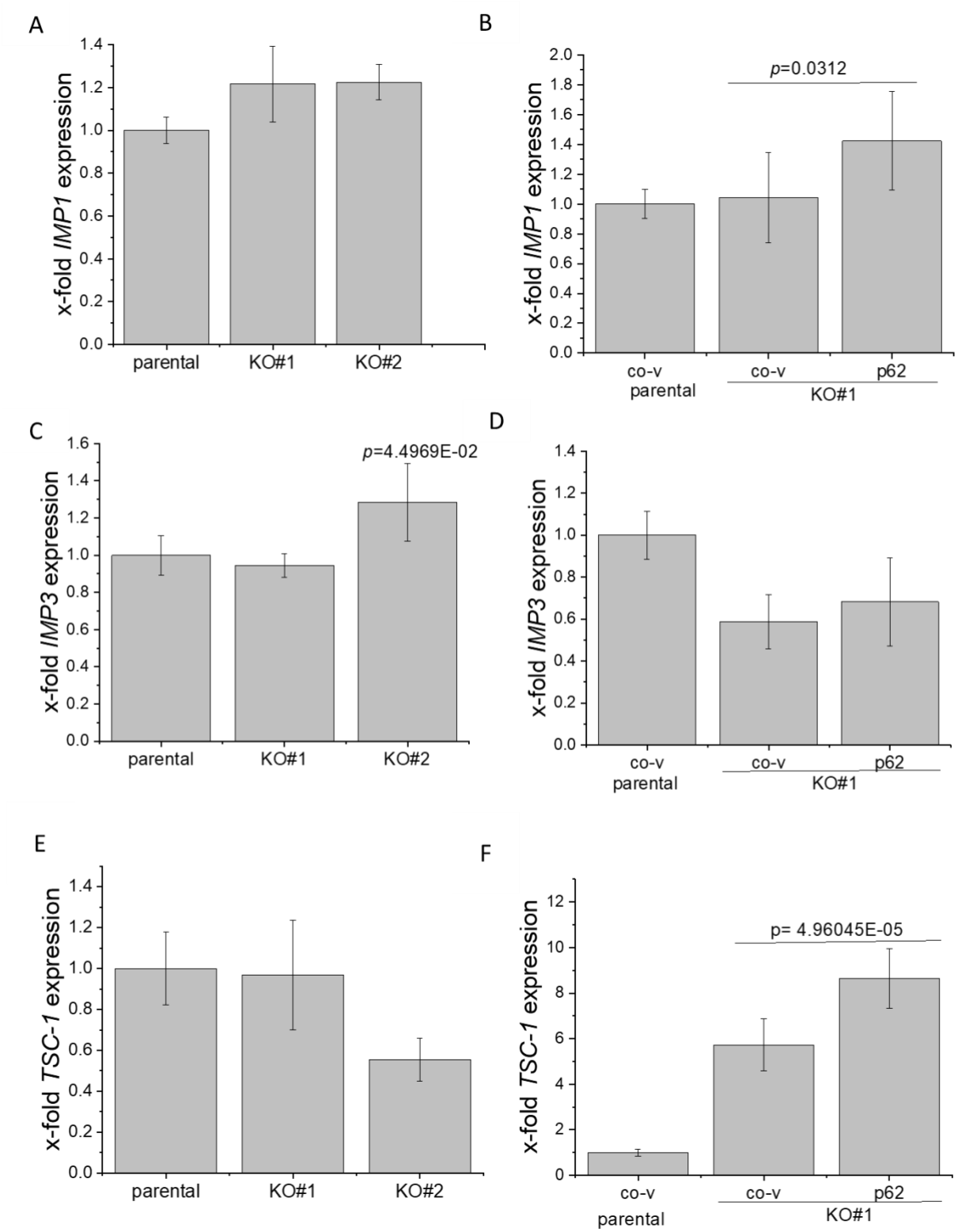
A
x-fold IMP1 expression
parental
KO#1
KO#2
B
p=0.0312
x-fold IMP1 expression
co-v
parental
co-v
p62
KO#1
C
p=4.4969E-02
x-fold IMP3 expression
parental
KO#1
KO#2
D
x-fold IMP3 expression
co-v
parental
co-v
p62
KO#1
E
x-fold TSC-1 expression
parental
KO#1
KO#2
F
p= 4.96045E-05
x-fold TSC-1 expression
co-v
parental
co-v
p62
KO#1

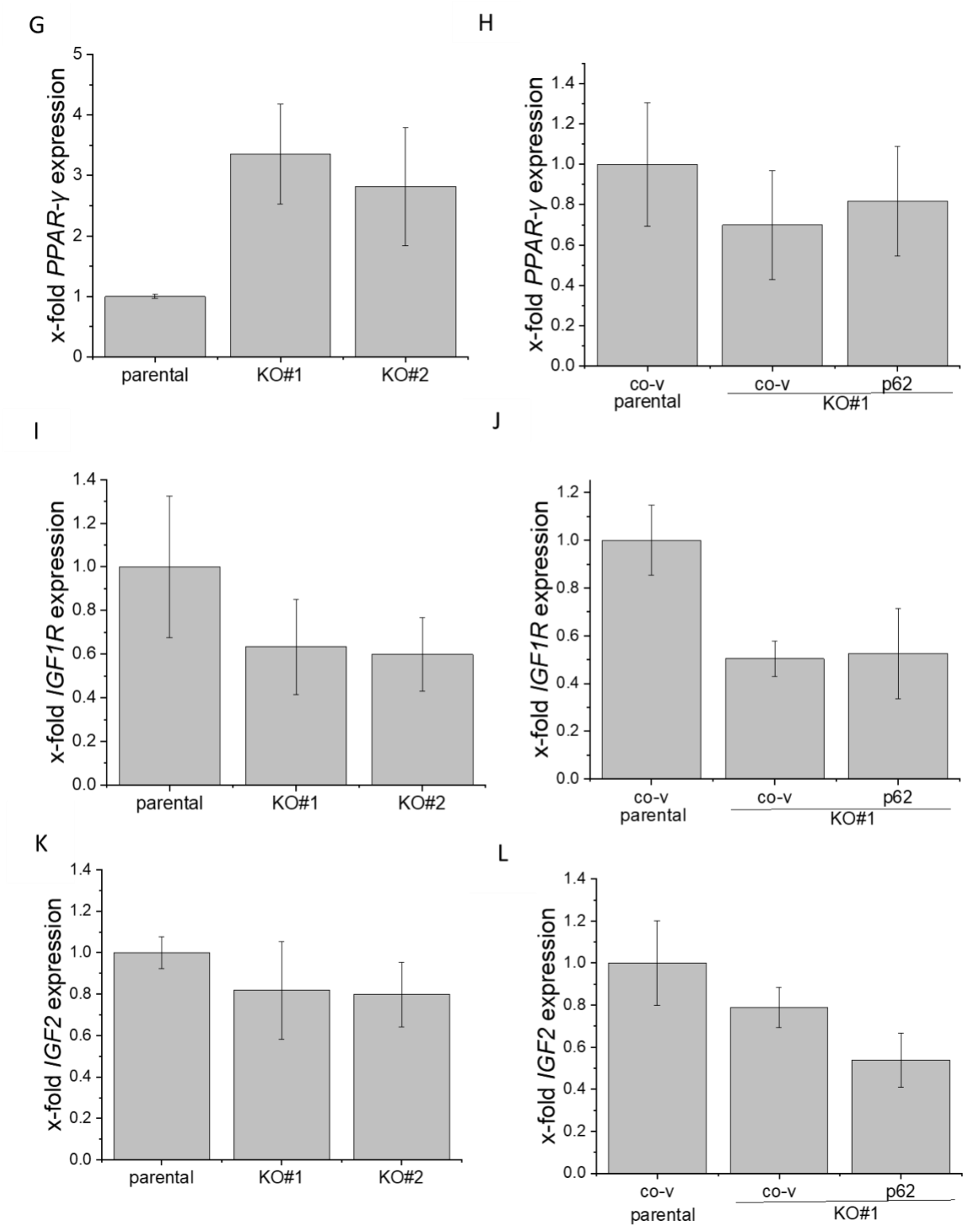
G
x-fold PPAR-γ expression
parental
KO#1
KO#2
H
x-fold PPAR-γ expression
co-v
parental
co-v
p62
KO#1
I
x-fold IGF1R expression
parental
KO#1
KO#2
J
x-fold IGF1R expression
co-v
parental
co-v
p62
KO#1
K
x-fold IGF2 expression
parental
KO#1
KO#2
L
x-fold IGF2 expression
co-v
parental
co-v
p62
KO#1

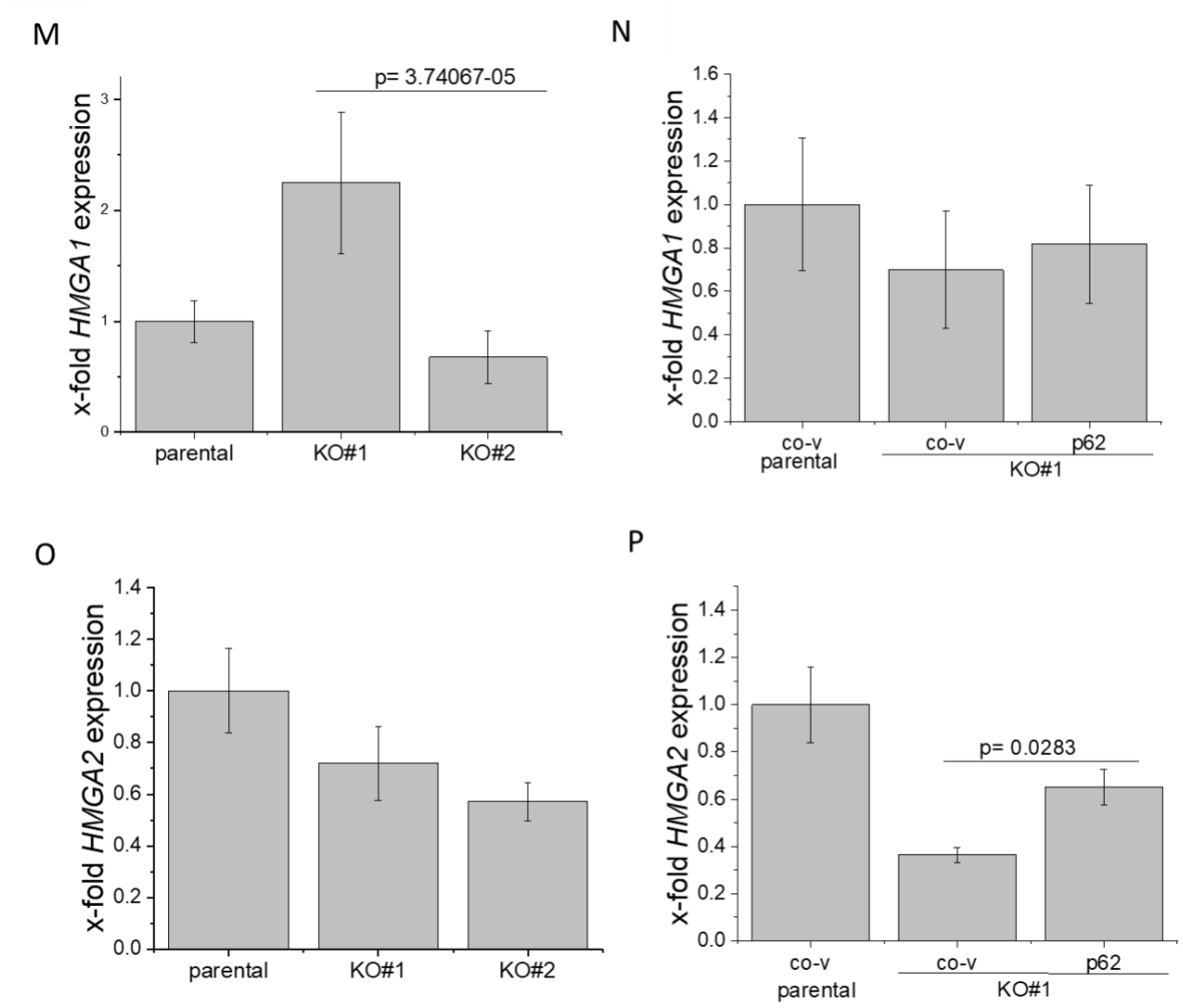

Supplementary Figure 4. (A) *IMP1*, (C) *IMP3*, (E) *TSC1*, (G) *PPAR-γ*, (I) *IGF1R*, (K) *IGF2*, (M) *HMGA1*, and (O) *HMGA2* gene expression were determined in the biallelic IMP2 knockout HCT116 cells and (B, D, F, H, J, L, N, P) *IMP2/p62* overexpressing parental and knockout cells by qPCR. Values were normalized to the housekeeping gene *RNA18SN5*. Data are represented as means ± SEM, n=3 (triplicates).

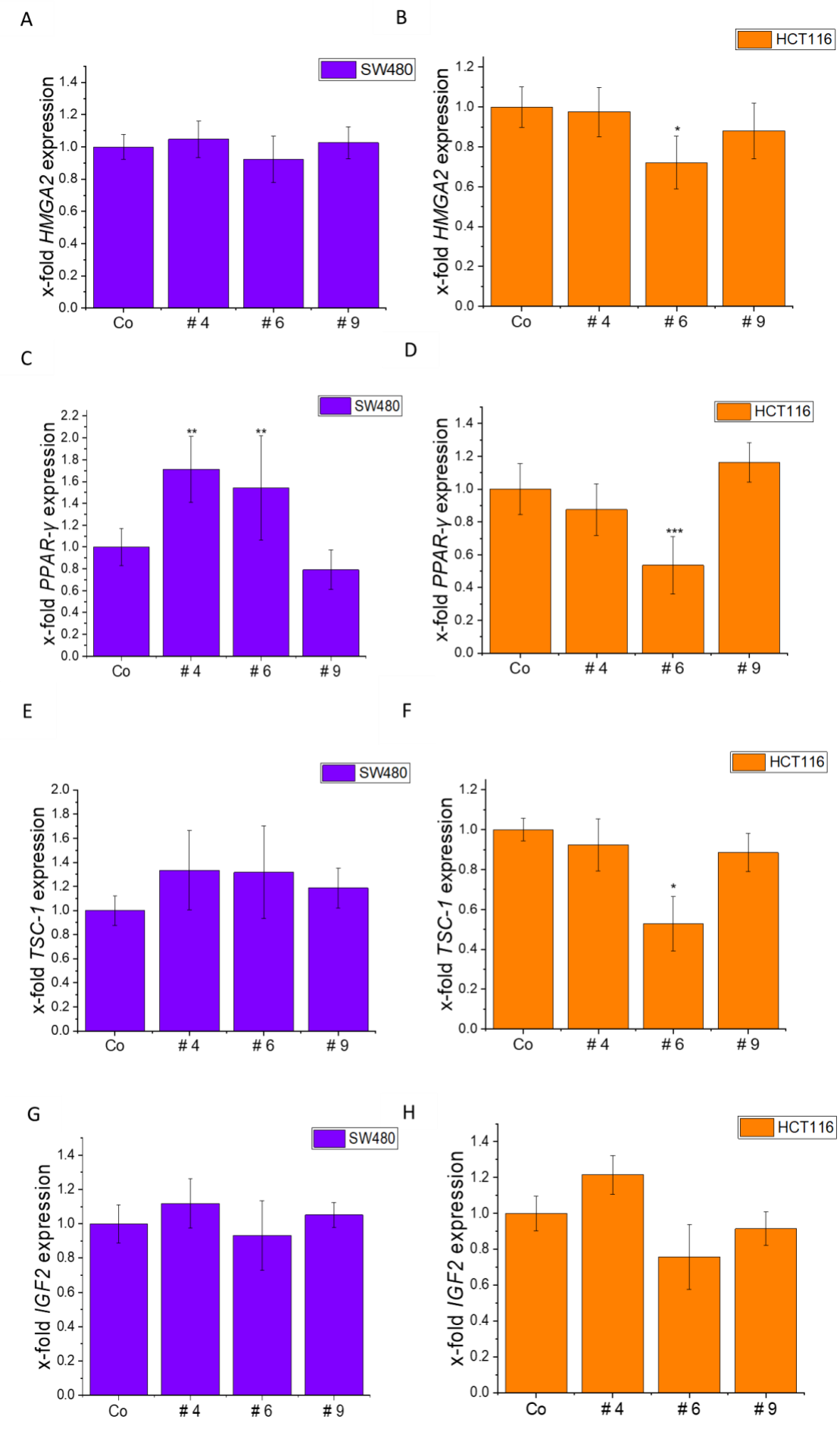
A
SW480
x-fold HMGA2 expression
Co
4
6
9
B
HCT116
x-fold HMGA2 expression
*
C
SW480
x-fold PPAR-γ expression
**
**
D
HCT116
x-fold PPAR-γ expression
***
E
SW480
x-fold TSC-1 expression
F
HCT116
x-fold TSC-1 expression
*
G
SW480
x-fold IGF2 expression
H
HCT116
x-fold IGF2 expression

Supplementary Figure 5. Expression of tumor-promoting *HMGA2*, *PPAR-γ*, *TSC1*, and *IGF2* upon IMP2 inhibitor compound treatment. (A, B) *HMGA2*, (C, D) *PPAR-γ*, (E, F) *TSC1* (G, H) IGF2 gene expression of SW480 (A, C, E, G) and HCT116 (B, D, F, H) cells after treatment with compound 4 (40 µM), 6 (50 µM), or 9 (50 µM) for 24 h, as determined by qPCR. Cells were cultured in 2D. Values were normalized to the housekeeping gene *RNA18SN5*. Data are represented as means ± SEM; n = 3 (triplicates). *p < 0.05, **p < 0.01, and ***p < 0.001 compared to values of respective wild-type (WT)/control (Co) cells.

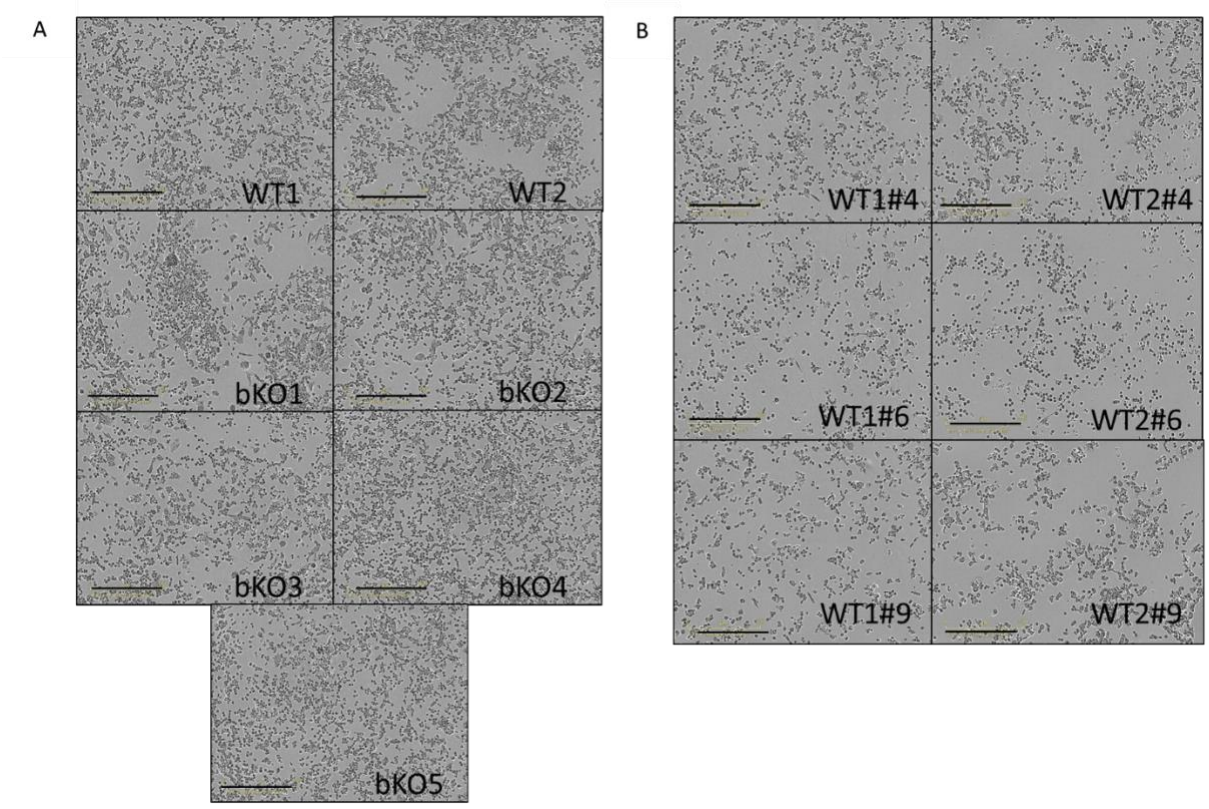

Supplementary Figure 6. Microscopic images of wild-type and biallelic IMP2 knockout and wild-type LLC1 cells upon IMP2 inhibitor treatment. (A) Wild-type and biallelic IMP2 knockout LLC1 cells at 48 h post-seeding. (B) The effects of IMP2 inhibitor compounds # 4, 6, and 9 at 30 µM after 48 h post-treatment. Images were obtained using the IncuCyte® S3 live cell imaging system; scale bar = 500 µm.

8.5 Plasmid maps

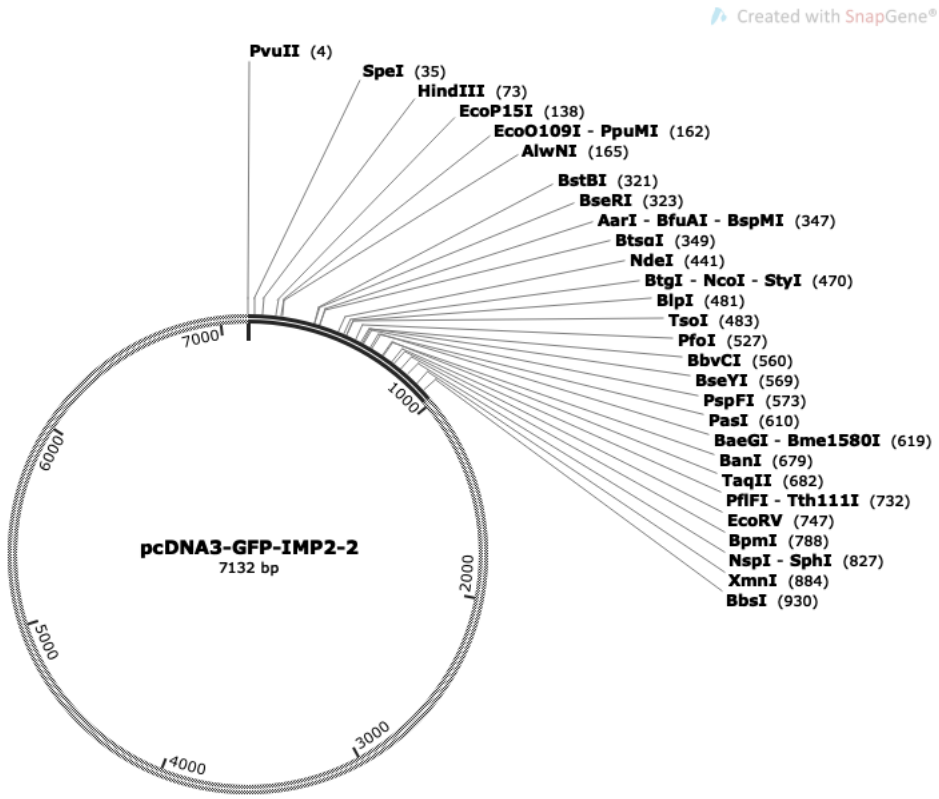

Supplementary Figure 7. pcDNA3-GFP-IMP2-2 (Plasmid #42175, Addgene). *IMP2* overexpression plasmid with GFP as a selection marker. Created with SnapGene®.

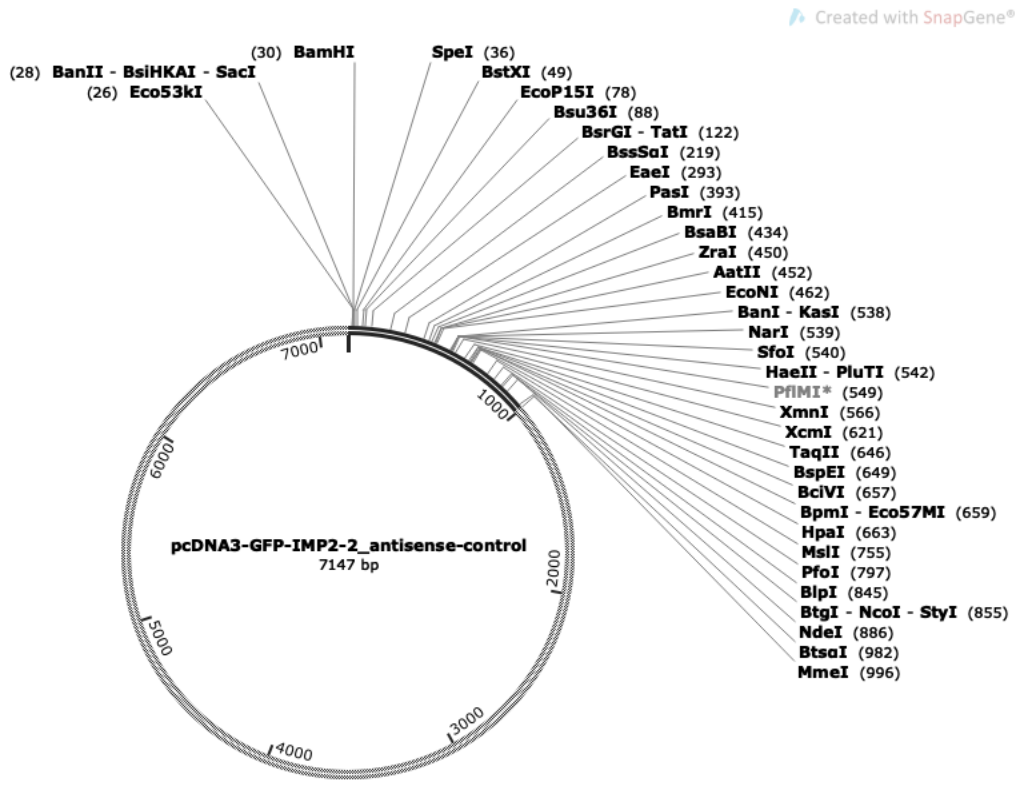

Supplementary Figure 8. pcDNA3-GFP-IMP2-2_antisense-control (Plasmid #42174, Addgene). *IMP2*- control plasmid with GFP as a selection marker. Created with SnapGene®.

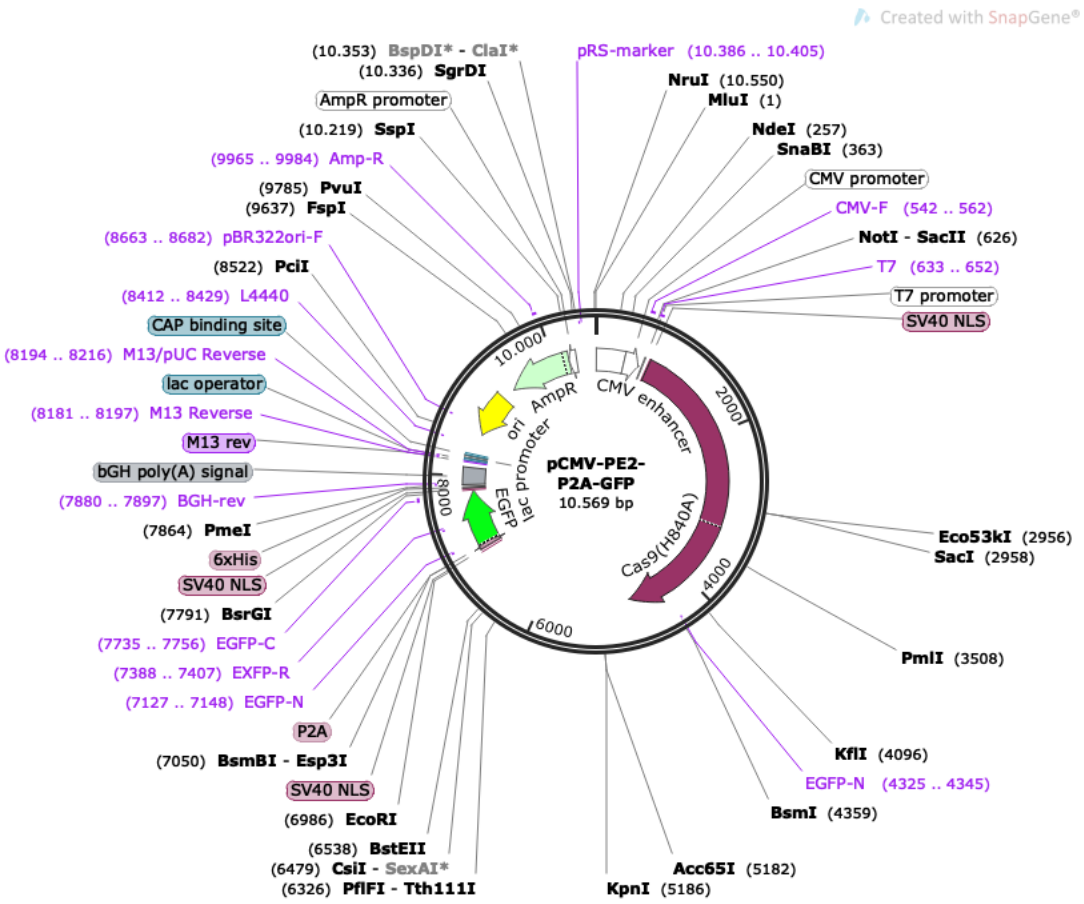

Supplementary Figure 9. pCMV-PE2-PE2A-GFP (Plasmid #132776, Addgene). The prime editor 2 plasmid is composed of the pentamutant Moloney murine leukemia virus reverse transcriptase (M-MLV RT), of Cas9-H840A nickase, and modified GFP (EGFP) as a selection marker. Created with SnapGene®.

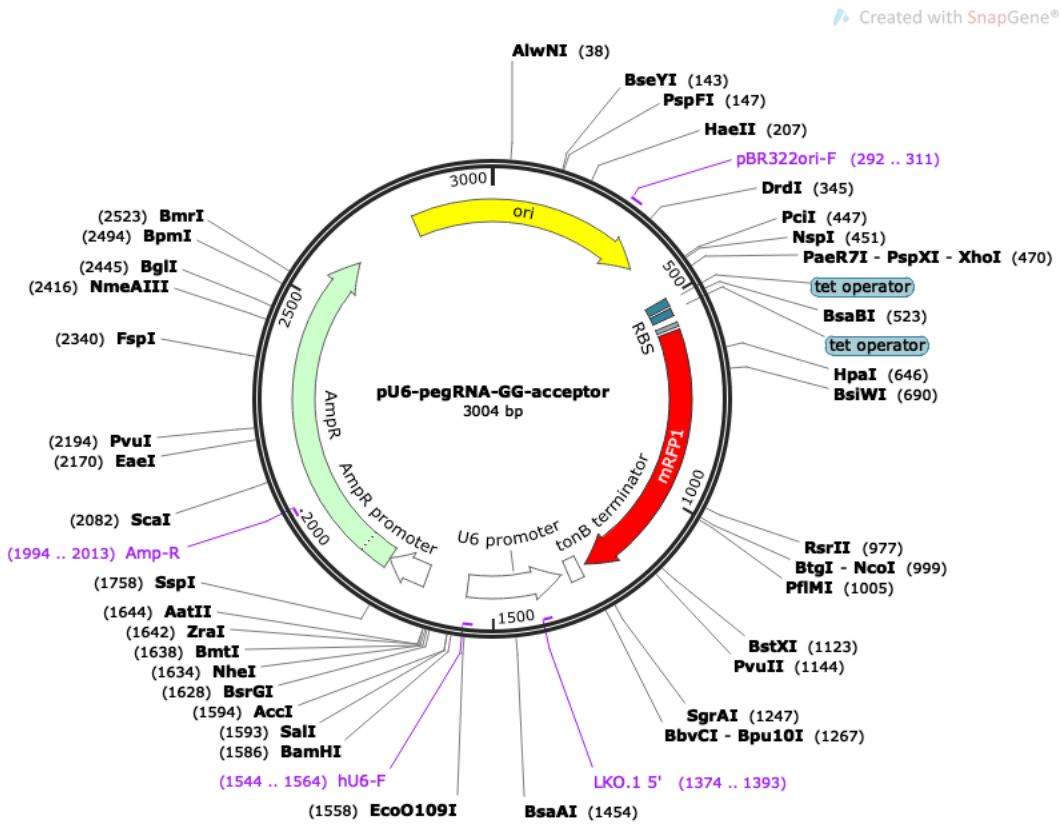

Supplementary Figure 10. pU6-pegRNA-GG-acceptor (plasmid #132777, Addgene). Plasmid containing a red fluorescent protein (mRFP1) dropout cassette as a placeholder for cloning of the pegRNAs in the prime editing approach. Successfully cloned and transformed bacterial colonies lack the red color and appear as white colonies on the agar plate. Created with SnapGene®.

Supplementary Figure 11. pSpCas9(BB)-2A-GFP (PX458) (plasmid #48138, Addgene). Plasmid contains a gRNA scaffold for cloning the desired gRNA construct, a fused Cas9 nickase, and a modified GFP as a selection marker. Created with SnapGene®.

8.6 List of tables and supplementary tables

8.7 List of figures and supplementary figures

8.8 Publications and conferences

Original publications

Shilpee Chanda, Konstantin Lepikhov, Charlotte Dahlem, Hanna S. Schymik, An-Kristin Geber, Konrad Wagner, Martin Empting, Alexandra K Kiemer. Characterization of the RNA binding protein IGF2BP2/IMP2 as an anticancer drug target: gene editing strategies and small molecule inhibitors. Frontiers in Bioscience Landmark. Manuscript in revision. September 2023.

Charlotte Dahlem, **Shilpee Chanda**, Jan Hemmer, Hanna Schymik, Michael Kohlstedt, Christoph Wittmann, Alexandra K. Kiemer. Characterization of Anti-Cancer Activities of Violacein: Actions on Tumor Cells and the Tumor Microenvironment. Frontiers in Oncology, 2022, May 11; 12:872223.

Charlotte Dahlem, Ali Abuhaliema, Sonja M. Kessler, Tarek Kröhler, Ben G. E. Zoller, **Shilpee Chanda**, Yingwen Wu, Simon Both, Fabian Müller, Konstantin Lepikhov, Susanne H. Kirsch, Stephan Laggai, Rolf Müller, Martin Empting, and Alexandra K. Kiemer. First Small-Molecule Inhibitors Targeting the RNA-Binding Protein IGF2BP2/IMP2 for Cancer Therapy, ACS Chemical Biology, 2022, 17 (2), 361-375.

Conference/Poster contributions

Shilpee Chanda, Charlotte Dahlem, Tarek Kroehler, Konstantin Lepikhov, An-Kristin Geber Alexandra K. Kiemer, 'Dependency on IGF2BP2/IMP2 for cancer cell proliferation', Ph.D. Student's Day, Universität des Saarlandes, 2023.

Shilpee Chanda, Charlotte Dahlem, Jan Hemmer, Hanna Schymik, Christoph Wittmann, Alexandra K. Kiemer, 'Anti-cancer action of violacein upon tumor cells and the tumor microenvironment', Tumor Microenvironment Meeting, British Association for Cancer Research, Nottingham, 2022.

8.9 Acknowledgement

I would like to express my heartfelt gratitude and appreciation to Prof. Dr. Alexandra Kiemer for providing me with the opportunity to pursue my Ph.D. under her exceptional supervision and guidance. I am sincerely thankful for her unwavering support throughout my journey, her willingness to invest her time, and her invaluable advice, which have been instrumental in my progress. Even during the most challenging phases of my research, her faith in me has served as a constant motivation.

I extend my deepest thanks to Prof. Dr. Andriy Luzhetskyy for graciously accepting the role of my second examiner and providing me with invaluable feedback on my dissertation during the annual project report presentations.

A special acknowledgment is owed to Dr. Charlotte Dahlem, who has been my Ph.D. supervisor and a constant pillar of support from the early days of my Ph.D. Her exceptional guidance and assistance have played a crucial role in shaping my project and enhancing my understanding of the important aspects of the Ph.D. journey.

I am grateful to Dr. Tarek Kröhler for his comprehensive insights into the CRISPR/Cas9-prime editing methods. Our stimulating discussions and his support during the challenging phases of the project have been truly invaluable.

I would like to extend my heartfelt thanks to Dr. Konstantin Lepikhov from the genetics department of Saarland University for his invaluable support in achieving the knockout cell lines and for his expertise in next-generation sequencing result generation and analysis. I cannot overstate my gratitude for his assistance. Furthermore, I would like to express my appreciation to Ms. An-Kristine Geber from the genetics department for her valuable contribution to processing the next-generation sequencing data.

I would like to thank Dr. Britta Diesel for her support and guidance on the ECIS method and Dr. Jessica Hoppstädter for her advice concerning my project. Special thanks go to Mr. Matti Müller, Ms. Lisa Flöck, Ms. Miriam Bläs, Ms. Euly Helena Oh, Mr. Simon Both, and Mr. Jan Hemmer for their invaluable assistance in the lab, especially during times of ill health. Additionally, I am grateful to Mr. Theo Ransweiler and Mr. Peter Schneider for their technical support. Thanks to Prof. Dr. Joseph Zapp, for his kind gestures and his teaching on chemical safety.

My special acknowledgment goes to Ms. Astrid Decker for her unwavering support in all office-related matters, especially her assistance and guidance in obtaining the GradUds funding.

I wish to express my gratitude to other members of the workgroup, Prof. Dr. Sonja Kessler, Dr. Ali Abuhaelima, Dr. Salma Al-Fityan, Dr. Rebecca Linnenberger, Dr. Vida Mahasheykhi, Ms. Muriel Hans, Ms. Hanna Schymik, Ms. Arefehsadat Kardani Esfahani, Mr. Thierry

Legröux, Ms. Annika Schomisch, Ms. Daria Dorry, Ms. Narges Jafari, Dr. Amanda Alice Wiesenthal, and Ms. Kinza Iqbal, for their friendly and supportive presence throughout my journey. Thanks to Ms. Eva, who made me familiar with the mouse facilities and my duties concerned therein.

I would like to express my appreciation and gratitude to the Deutsche Akademischer Austauschdienst (DAAD) for their generous financial support and all the assistance provided during my stay in Germany for my doctoral work. I would also like to express my gratitude to DAAD-STIBET funding which provided financial support for the first three years of my program. I convey my gratitude to GradUS, for providing me with funds to cover the cost of attending the BACR Conference held at Nottingham, United Kingdom.

I am profoundly thankful to my parents and my husband for their unwavering support throughout this journey. Their consistent encouragement has empowered me to venture beyond my comfort zone and acquire priceless life lessons.